Investigation of Turbulent Spray Flames Using the Conditional Source-term Estimation (CSE) Approach

by

Ahmed Hussien

A thesis
presented to the University of Waterloo
in fulfillment of the
thesis requirement for the degree of
Doctor of Philosophy
in
Mechanical and Mechatronics Engineering

Waterloo, Ontario, Canada, 2022

Examining Committee Membership

The following served on the Examining Committee for this thesis. The decision of the Examining Committee is by majority vote.

External Examiner: Matthew Cleary
                            Associate Professor, School of Aerospace, Mechanical and
                            Mechatronic Engineering,
                            University of Sydney

Supervisor(s):   Cecile Devaud
                            Professor, Dept. of Mechanical and Mechatronics Engineering,
                            University of Waterloo

Internal Member: Fue-Sang Lien
                            Professor, Dept. of Mechanical and Mechatronics Engineering,
                            University of Waterloo

Internal Member: Zhongchao Tan
                            Professor, Dept. of Mechanical and Mechatronics Engineering,
                            University of Waterloo

Internal-External Member: Hans De Sterck
                            Professor, Dept. of Applied Math,
                            University of Waterloo

Author's Declaration

I hereby declare that I am the sole author of this thesis. This is a true copy of the thesis, including any required final revisions, as accepted by my examiners.

I understand that my thesis may be made electronically available to the public.

Abstract

Conditional Source-term Estimation (CSE) is a turbulent combustion model for gaseous combustion. This work aims at extending the CSE formulation to address turbulent spray combustion. The Eulerian-Lagrangian method is implemented where the Eulerian and Lagrangian methods are used to describe the gas and liquid phases, respectively. Two-way coupling is implemented where the mutual effects of the gas and liquid phases are accounted for. Reynolds-Averaged Navier-Stokes (RANS) and Large Eddy Simulation (LES) equations for gas combustion are solved along with the Lagrangian equations to determine the liquid phase source terms. The mass, momentum, enthalpy, and species equations are solved with adequate closures for the unclosed terms. Detailed chemistry mechanisms are included by tabulating the reaction rates and mass fractions prior to the simulations.

To assess the Lagrangian spray model, RANS equations are solved to investigate a turbulent non-reacting acetone spray. The gas velocity and spray statistics show good agreement with the experimental data. In CSE, the mixture fraction is used as a conditioning variable to study non-premixed combustion. CSE is implemented to simulate a series of turbulent non-premixed acetone spray flames. The results reveal generally good agreement for the gas and spray compared to the experiments with noticeable discrepancies at some locations. The sources of discrepancy include inaccurate turbulent mixing field, increased level of premixing for some flames, and the neglect of spray effect in the chemistry tabulation. Doubly CSE (DCSE) is implemented by introducing the progress variable as a second conditioning variable to simulate partially premixed ethanol spray flames. Unlike previous DCSE implementations, a non-normalized progress variable representation is used to eliminate modeling difficulties related to the normalized form. The comparison between CSE and DCSE shows improved DCSE predictions at most locations.

The effects of enthalpy losses due to evaporation and gas radiation are included in the chemistry tabulation by introducing a fourth dimension to the chemistry library. Further, LES is performed to obtain more accurate mixing fields to study turbulent ethanol flames close to the blow-off limit. In general, LES improves the predictions compared to RANS simulation. In addition, adding the enthalpy losses enhances the temperature predictions, particularly for the flames with high jet velocities.

In conclusion, this study proves the capability of CSE/DCSE in accurately predicting the gas and spray statistics. Future work may address more complex fuels, swirl spray, combustion in higher pressures, and more accurate spray models.

Acknowledgements

Dedication

This is dedicated to the one I love; God, my family and my close friends.

Table of Contents

List of Figures

xiv

List of Tables

Nomenclature

δ_{ij} Kronecker delta

$\dot{\omega}_k$ Species chemical reaction rate [kg/(m^{3}s)]

$\dot{\rho}_k$ The spray source terms for specie k due to evaporation

$\dot{\rho}$ The spray source terms for mass transfer due to evaporation

$\dot{F}_j$ The spray source terms for momentum transfer between the gas and liquid phases

$\dot{Q}$ The source term due to enthalpy transfer between the liquid and gas phases

$\dot{q}_{react}$ The enthalpy source term due to chemical reactions

η Mixture fraction sample space

λ Regularization parameter

CMC Conditional Moment Closure

CSE   Conditional Source-term Estimation

DCSE Doubly conditional Source-term Estimation

EBU   EddyBreak Up

EDM   Eddy Dissipation Model

LES   Large Eddy Simulation

MMC Multiple Mapping Conditioning

PDF   Probability Density Function

RANS Reynolds Averaged Navier Stokes

SGS Sub-grid scale

TGLDM Trajectory Generated Low Dimension Manifold

μ Molecular Viscosity [Pa s]

μ_t Turbulent viscosity

ρ Density [kg/m^3]

σ The Stefan-Boltzmann constant

σ_s Mixture fraction variance source term

τ_u Momentum relaxation time

τ_{ij} The viscous stress tensor

ε Turbulent dissipation rate

$\vec{\alpha}$ Solution of the Fredholm integral equation

$\widetilde{P}$ Favre-averaged PDF of mixture fraction

$\widetilde{Q}$ Favre average of the quantity Q

$a_{p,k}$ The Planck absorption coefficient of species k

B_m Spalding Mass number

C Progress variable

C''^2 Progress variable variance

c^* Progress variable sample space

C_μ, C_{ε_1}, C_{ε_2}, σ_k, σ_ε Standard $k - \varepsilon$ model constants

C_D Drag coefficient

C_s Smagorinsky constant

D Droplet diameter, jet inlet diameter

D_k The diffusion coefficient of k

D_t Turbulent diffusion coefficient

h Sensible Enthalpy

J_k The diffusion flux of specie k

K Kinetic Energy

k Turbulent kinetic energy

m_d Droplet mass

Nu Nusselt number

p Pressure

P_k Production term of the turbulent kinetic energy

Pr Prandtl number

q The heat flux

Q'' Fluctuation of the quantity Q

Q_{rad} The radiative heat loss

Re Reynolds number

S_{ij} Strain rate tensor

Sc Schmidt number

Sh Sherwood number

T Temperature [K]

t Time

u_i Velocity in i direction

x_i Spatial coordinate in ith direction

Y_d The mass fraction of droplets with diameter greater than d

Y_k Chemical specie k

Z Mixture fraction

Z''^2 Mixture fraction variance

χ Scalar dissipation rate

Chapter 1

Introduction

1.1 Motivation

Turbulent combustion is found in numerous industrial and daily life applications such as furnaces, automotive engines, and jet engines. Most of these devices use liquid fossil fuels to operate. Liquid fuels such as kerosene and gasoline have been the largest energy resource in the world and expected to further increase in the future [1], as seen in Figure 1.1. However, liquid fossil fuel combustion is responsible for the largest portion of combustion emissions such as carbon dioxide (CO_2) [1]. In addition, they produce large amounts of undesirable gases such as carbon monoxide (CO), nitrogen oxides (NO_x), and sulphur oxides (SO_x) that have to be controlled to meet the local air emission regulations. Since fossil fuels are unsustainable and cause environmental pollution, biofuels may introduce a cleaner alternative. Biofuels are renewable energy sources that can replace fossil fuels since they are environmentally friendly. As seen in Figure 1.1, biofuels commonly exist in solid and liquid phases and constitute a small fraction of the total fuel consumption. Since fossil fuels and biofuels are usually in the liquid form, understanding liquid fuel combustion may assist in decreasing pollution levels and the global greenhouse effect. Thus, it is crucial to have accurate spray combustion modeling to enhance combustion efficiency.

The liquid fuels are commonly introduced into the combustion chamber in the form of spray in order to enhance evaporation and mixing for effective combustion. Thus, the accurate characterization of the entire spray-turbulent combustion process is crucial for the in-depth understanding and prediction of flame stability and emissions. The turbulent spray combustion process is challenging to model because of the coupled phenomena between liquid fuel evaporation, turbulent mixing and chemistry that take place within the

1
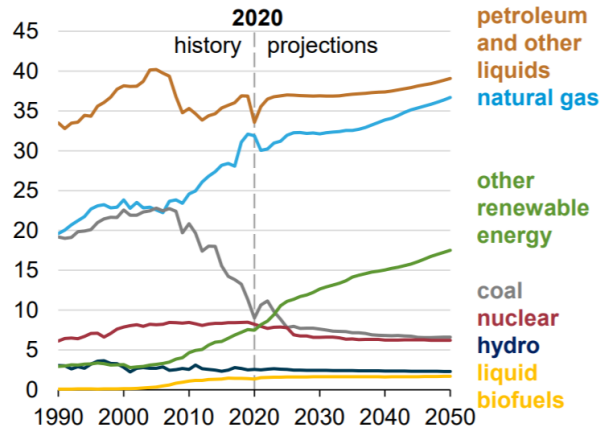
Figure 1.1: U.S. energy consumption by fuel (quadrillion Btu) (Reproduced from [1])

flame resulting in a wide range of length and time scales and multi combustion regimes [8, 9, 10]. Although experimental methods can be used to study turbulent spray flames, they are often costly and time consuming. Therefore, numerical simulations introduce a desirable option where more aspects of the detailed combustion processes can be studied while maintaining a reasonable computational cost. This can be achieved by taking advantage of the recent increase in the computational resources. As a result, the numerical simulations of turbulent combustion have become a valuable tool in designing and optimizing combustion devices. Overall, both experimental and numerical studies are complimentary to better understand turbulent combustion.

1.2 Objectives

The long term objective of the proposed research is to establish a reliable and accurate methodology to simulate turbulent spray flames in conditions similar to those found in real industrial combustion devices such as gas turbine engines. Gas turbines may use several liquid fuels such as gasoline, diesel, and kerosene. In the current study, Conditional Source-term Estimation (CSE) is selected to provide a closure for the mean reaction rate in the turbulent species transport equations. CSE is a well recognized model which has been successfully applied to model different types of flames. However, it has never been extended to simulate multiphase flows or spray flames. Further, the detailed chemistry tables have only been generated for simple hydrocarbon fuels such as methane-air [11] and methanol-air [12] combustion. As a part of this PhD research, new chemistry tables are

created for different fuels such as acetone and ethanol. The experimental set of turbulent spray flames from the University of Sydney performed by Gounder and Masri [7, 13] is used in the current investigation. The experimental set includes turbulent acetone evaporating jets, turbulent acetone spray flames, and turbulent ethanol spray flames. For simplicity and to focus only on the liquid-gas phase interactions, no soot modeling is included in this study. For acetone and ethanol spray flames, all the experimental data are related to liquid fuels producing negligible amount of soot [13]. The predictions of all the quantities such as the gas temperature, mass fractions, velocity, and flame structure are compared with the experimental results and published numerical simulations using different turbulent combustion models. Further, the spray statistics such as droplet velocity, droplet size, and evaporation rate are compared with the experimental data to assess the capability of the spray model in predicting these quantities. The main objectives of this study are summarized as follows:

1. **Coupling of the CSE combustion model with a Lagrangian spray formulation to accurately simulate turbulent spray flames.**

   CSE is extended to simulate turbulent spray flames by coupling the existing CSE formulations with a Lagrangian spray formulations and introducing some terms for spray in the gas equations. To accomplish this objective, the following tasks are undertaken

   - **Performing RANS simulations for turbulent non-reacting acetone spray.**
     It is crucial to ensure that the Lagrangian spray model is capable of accurately predicting the spray characteristics in non-reacting cases. Thus, the uncertainties related to combustion modeling are eliminated and the Lagrangian spray model can be qualitatively assessed.

   - **Generating the chemistry tables for acetone and ethanol combustion.**
     CSE is commonly applied with tabulated chemistry. This work considers acetone and ethanol flames. Thus, adequate tables for adiabatic acetone and ethanol combustion are generated and tested.

   - **Performing RANS simulations for non-premixed spray combustion.**
     RANS numerical simulations using non-premixed CSE are conducted to study a series of mostly non-premixed turbulent acetone spray flames. Turbulent spray flames with diffusion characteristics are selected to investigate the performance of the non-premixed CSE formulation in spray combustion.

2. **Develop a spray combustion formulation capable of predicting turbulent spray flames under multiple conditions.**

   The non-premixed CSE formulation is anticipated to have adequate performance for diffusion flames. However, the performance is expected to degrade when higher levels of premixing are present. In addition, RANS simulations have well-known limitations that affect the accuracy of the predictions. Further, the effects of the enthalpy loss on the conditional averages should be investigated. To address these points, the following steps are considered

   - **Applying doubly CSE (DCSE) to address flames with higher premixing levels in RANS.**
     CSE is extended to DCSE by introducing another conditioning variable. A series of turbulent partially premixed ethanol flames is investigated using RANS computations. A comparison between CSE and DCSE is conducted.

   - **Investigating a series of turbulent ethanol spray flames in LES using adiabatic chemistry tables.**
     CSE is extended for LES implementation by modeling the SGS terms in the governing equations. LES is conducted to study a series of turbulent spray flames using adiabatic chemistry tables. Flames close to the blow-off limit are also investigated. LES is expected to provide more accurate predictions compared to RANS.

   - **Generating non-adiabatic chemistry tables for ethanol combustion.**
     To account for the enthalpy losses due to spray evaporation and gas radiation on the conditional averages, a chemistry library for different enthalpy loss levels is created.

   - **Performing LES using the non-adiabatic chemistry library.**
     LES is performed using the non-adiabatic chemistry tables. A comparison between the adiabatic and non-adiabatic chemistry tables is conducted.

1.3   Thesis overview

Chapter 2 presents the governing equations of gas phase and the closure of different terms. Different techniques to deal with turbulent flows are also discussed. Chapter 3 describes the different approaches to describe the liquid phase. Further information is provided for the Eulerian-Lagrangian approach adopted in the current study. Chapter 4 overviews the

most common turbulent combustion models in the literature. In addition, the formulation of CSE for non-premixed combustion is discussed in detail. The experimental setup used for investigation is also described. Chapter 5 addresses the application of non-premixed CSE in RANS to study a series of mostly non-premixed acetone spray flames. Chapter 6 first provides a detailed description of DCSE formulation and then compares CSE with DCSE in describing partially premixed flames. Chapter 7 first discusses the coupling of CSE with non-adiabatic chemistry tables and then reports an LES study to compare the predictions using adiabatic and non-adiabatic tables. Finally, the conclusions and future work are summarized in Chapter 8

1.4   Author's current contributions

It is acknowledged that parts of the content presented in Chapters 5, 6, and 7 are published or under review in the following articles [14, 15]

1. A. Hussien, C. Devaud, Simulations of turbulent acetone spray flames using the conditional source term estimation (CSE) approach, Combust. Theor. Model. 25 (2020) 1–24.

2. A. Hussien, C. Devaud, Simulations of partially premixed turbulent ethanol spray flames using doubly conditional source term estimation (DCSE), Combust. Flame (2021) 111651.

3. A. Hussien, C. Devaud, LES study of turbulent ethanol spray flames using CSE coupled with non-adiabatic chemistry tables, Proc. Combust. Inst., under review (2022).

Chapter 2

Gas phase formulation

This chapter presents the governing equations and modeling approaches used to describe the gas phase in the current study. The general transport equations and the closure for the different terms are discussed.

2.1 Governing equations

The mass and momentum conservation equations for the gas phase (including the source terms for gas-spray interactions) can be expressed as

$$\frac{\partial \rho}{\partial t} + \frac{\partial}{\partial x_i}(\rho u_i) = \dot{\rho}, \tag{2.1}$$

$$\frac{\partial}{\partial t}(\rho u_j) + \frac{\partial}{\partial x_i}(\rho u_i u_j) = -\frac{\partial p}{\partial x_j} + \frac{\partial \tau_{ij}}{\partial x_i} + \dot{F}_j, \tag{2.2}$$

where ρ is the density, u_i the velocity in the i-direction, p the pressure, and τ_{ij} the viscous stress tensor. $\dot{\rho}$ and $\dot{F}_j$ are the spray source terms for mass and momentum, respectively, due to the interaction between the gas phase and liquid phase. The viscous stress tensor can be expressed as a function of the strain rate tensor S_{ij} as [16]

$$\tau_{ij} = \mu[2S_{ij} - \frac{2}{3}\delta_{ij}\frac{\partial u_k}{\partial x_k}]. \tag{2.3}$$

The species transport equation is

$$\frac{\partial}{\partial t}(\rho Y_k) + \frac{\partial}{\partial x_i}(\rho u_i Y_k) = -\frac{\partial J_{k,i}}{\partial x_i} + \dot{\omega}_k + \dot{\rho}_k, \tag{2.4}$$

where Y_k is the mass fraction of species k, $\dot{\omega}_k$ the reaction rate of species k, J_k the diffusion flux of specie k, and $\dot{\rho}_k$ the source term describing the mass transfer from the liquid phase to the gas phase of the k-th species due to evaporation. The evaporation source term is zero for all the species except for the fuel. The sensible enthalpy equation is expressed as

$$\frac{\partial}{\partial t}(\rho h) + \frac{\partial}{\partial x_i}(\rho u_i h) = -\frac{\partial q_i}{\partial x_i} + \dot{Q} + Q_{rad} + \dot{q}_{react}, \tag{2.5}$$

where h is the sensible enthalpy, q the heat flux, $\dot{Q}$ the source term describing the enthalpy transfer between the liquid and gas phases, Q_{rad} the radiation losses and $\dot{q}_{react}$ the enthalpy source term due to chemical reactions.

2.2 Turbulent flows

Turbulent flows are characterized by a wide range of length and time scales. To resolve all the time and length scales, Direct Numerical Simulation (DNS) must be used. However, it is computationally expensive since the smallest turbulent scales in the simulation are of the order of the Kolmogorov length scale. The number of cells increases with a power of 9/4 with the Reynolds number [16] as discussed in Section 2.5. It is also highly challenging to carry out DNS for high Reynolds numbers with the current computational resources. Therefore, Reynolds-Averaged Navier-Stokes (RANS) equations are introduced to obtain averaged solutions at low computational cost. In RANS, all the fluctuations are modelled and several approaches can be used to model the unclosed terms in the governing equations, as discussed in Section 2.3. Alternatively, Large Eddy Simulation (LES) can be applied to capture the unsteady physics at more affordable computational cost. LES resolves all the large scales down to the grid size which is taken to be the filter width. LES has shown good performance on various types of turbulent flows. LES is briefly introduced in Section 2.4.

2.3 Reynolds Averaged Navier Stokes (RANS)

In RANS, Navier-Stokes equations are averaged to obtain the mean values of all the quantities in turbulent flows. This introduces some additional terms in the equations that require modeling. The eddy viscosity concept is usually applied to close the Reynolds stress term. However, the turbulent viscosity needs to be calculated first. Different turbulence models are available including algebraic models, one equation models, two equation models,

and Reynolds stress model. The most common approaches in RANS are two equation models due to their simplicity and robustness [17]. Two transport equations are commonly solved, one for turbulent kinetic energy and the other for another variable such as turbulent dissipation rate in the k-ε model. Moreover, two equation models have been used in industry for a long time, and they are properly documented [16]. In combustion, the density variations in the computational domain are usually large due to the very high temperature variations encountered in combustion processes. Therefore, it is suitable to use density-weighted averages or Favre averages in turbulent combustion simulations. The Favre-averaging also suppresses the terms containing correlations involving density fluctuations, leading to significant simplifications in the governing equations. Reynolds-averaging results in additional unclosed terms, even in the continuity equation, unlike Favre-averaging. Any Favre-averaged quantity can be expressed as

$$\tilde{\phi} = \frac{\overline{\rho\phi}}{\overline{\rho}}, \tag{2.6}$$

where ϕ represents a flow variable like the velocity and the fluctuations are identified as

$$\phi'' = \phi - \tilde{\phi}. \tag{2.7}$$

The flow governing equations can be derived using Favre-averaging. The continuity equation is expressed as

$$\frac{\partial \overline{\rho}}{\partial t} + \frac{\partial}{\partial x_i}(\overline{\rho}\tilde{u}_i) = \dot{\overline{\rho}}. \tag{2.8}$$

The momentum equation is expressed as

$$\frac{\partial}{\partial t}(\overline{\rho}\tilde{u}_j) + \frac{\partial}{\partial x_i}(\overline{\rho}\tilde{u}_i\tilde{u}_j) = -\frac{\partial \overline{p}}{\partial x_j} + \frac{\partial}{\partial x_i}(\overline{\tau}_{ij} - \overline{\rho\widetilde{u_i''u_j''}}) + \dot{\overline{F}}_j. \tag{2.9}$$

The species equation for a given k species is

$$\frac{\partial}{\partial t}(\overline{\rho}\tilde{Y}_k) + \frac{\partial}{\partial x_i}(\overline{\rho}\tilde{u}_i\tilde{Y}_k) = \dot{\overline{\omega}}_k - \frac{\partial}{\partial x_i}(\overline{\rho\widetilde{u_i''Y_k''}}) + \overline{\frac{\partial}{\partial x_i}\rho D_k \frac{\partial Y_k}{\partial x_i}} + \dot{\overline{\rho}}_k, \tag{2.10}$$

where D_k is the diffusion coefficient of species k. $\dot{\overline{\rho}}_k$ is the fuel evaporation source term. This term only exists for the fuel and is zero for all other species. The sensible enthalpy equation including the source terms due to chemical reaction, evaporation, and radiation is written as

$$\frac{\partial}{\partial t}(\overline{\rho}\tilde{h}) + \frac{\partial}{\partial x_i}(\overline{\rho}\tilde{u}_i\tilde{h}) = -\frac{\partial \overline{q}_i}{\partial x_i} + \overline{\rho\widetilde{u_i''h''}} + \dot{\overline{Q}} + \dot{\overline{q}}_{react} + \overline{Q}_{rad}. \tag{2.11}$$

In the current incompressible flow conditions, the mean pressure is assumed constant and the pressure terms in Equation 2.11 are neglected.

The viscous stress tensor can be expressed as a function of the mean strain rate tensor $\widetilde{S_{ij}}$ as

$$\overline{\tau_{ij}} = \mu[2\widetilde{S_{ij}} - \frac{2}{3}\delta_{ij}\frac{\partial \widetilde{u_k}}{\partial x_k}], \tag{2.12}$$

$$\widetilde{S_{ij}} = \frac{1}{2}(\frac{\partial \widetilde{u_i}}{\partial x_j} + \frac{\partial \widetilde{u_j}}{\partial x_i}), \tag{2.13}$$

where μ is the dynamic viscosity. The Reynolds stress term $\overline{\rho u_i'' u_j''}$ can be expressed as a function of the velocity gradients by utilizing the eddy viscosity concept such that

$$-\widetilde{u_i'' u_j''} = \nu_t \left(\frac{\partial \widetilde{u_i}}{\partial x_j} + \frac{\partial \widetilde{u_j}}{\partial x_i} \right) - \frac{2}{3}k\delta_{ij}, \tag{2.14}$$

where ν_t is the turbulence eddy viscosity, and k the turbulent kinetic energy, which can be expressed as $k = \frac{1}{2}\widetilde{u_i'' u_i''}$. The unclosed terms in the species and energy equations can be modelled using the gradient assumption as

$$\overline{\rho u_i'' Y_k''} = -\frac{\mu_t}{Sc_t}\frac{\partial \widetilde{Y_k}}{\partial x_j}, \tag{2.15}$$

$$\overline{\rho u_i'' h''} = -\frac{\mu_t}{Pr_t}\frac{\partial \widetilde{h}}{\partial x_j}, \tag{2.16}$$

where μ_t is the turbulent viscosity calculated from the turbulence model, Sc_t the turbulent Schmidt number, and Pr_t the turbulent Prandtl number. The turbulent Schmidt number and the turbulent Prandtl number are set to be equal assuming unity Lewis number. Sc_t usually takes a value around 0.7 in combustion problems based on comparison with experiments [18]. In this work, this value is investigated in different implementations.

2.3.1 Standard k-ε model

The k-ε model is one of the most commonly used RANS models. It solves one equation for turbulent kinetic energy k and another equation for the turbulence dissipation rate (ε) [19]. The transport equations of k and ε can be expressed as

$$\overline{\rho}\frac{\partial k}{\partial t} + \overline{\rho}\tilde{u}_i\frac{\partial k}{\partial x_i} = \overline{\rho}P_k - \overline{\rho}\varepsilon + \frac{\partial}{\partial x_i}\left[\left(\mu + \frac{\mu_t}{\sigma_k}\right)\frac{\partial k}{\partial x_i}\right], \tag{2.17}$$

9

$$\bar{\rho}\frac{\partial \varepsilon}{\partial t} + \bar{\rho}\tilde{u}_i\frac{\partial \varepsilon}{\partial x_i} = C_{\varepsilon 1}\frac{\varepsilon}{k}P_k - C_{\varepsilon 2}\bar{\rho}\frac{\varepsilon^2}{k} + \frac{\partial}{\partial x_i}\left[\left(\mu + \frac{\mu_t}{\sigma_\varepsilon}\right)\frac{\partial \varepsilon}{\partial x_i}\right], \qquad (2.18)$$

where the turbulent viscosity can be calculated from

$$\mu_t = \bar{\rho}C_\mu\frac{k^2}{\varepsilon}, \qquad (2.19)$$

and the production term can be calculated as

$$P_k = -\overline{\rho u_i'' u_j''}\frac{\partial \tilde{u}_i}{\partial x_j}. \qquad (2.20)$$

The model coefficients for standard k-ε commonly have the values as followed: $C_\mu = 0.09$, $\sigma_k = 1.00$, $\sigma_\varepsilon = 1.30$, $C_{\varepsilon 1} = 1.44$, and $C_{\varepsilon 2} = 1.92$.

The k-ε model is a robust turbulence model that has been successfully used for different applications. However, it is known to overpredict the spreading rate of axisymmetric jets. Consequently, the constant $C_{\varepsilon 1}$ is commonly varied to obtain the optimum mixing field [20]. Therefore, $C_{\varepsilon 1}$ is investigated in this work for different flames for better agreement with the experimental results.

2.3.2 Mixture fraction

The mixture fraction is a scalar that represents the mixing of the fuel and the oxidizer. It is defined such that it has a value of 1 in pure fuel and a value of 0 in pure oxidizer. The mixture fraction Z is defined by Bilger [21] as

$$Z = \frac{Y_i - Y_{i,O}}{Y_{i,F} - Y_{i,O}}, \qquad (2.21)$$

where Y_i is the mass fraction of element i in the local mixture, $Y_{i,O}$, and $Y_{i,F}$ are the mass fractions of element i in the oxidizer and fuel streams, respectively. In gaseous combustion, the mixture fraction is a conserved scalar where there are no source terms in the mixture fraction transport equation. However, a source term arises in spray combustion due to evaporation. The Favre-averaged equations of mixture fraction mean and variance are given by

$$\frac{\partial}{\partial t}(\bar{\rho}\tilde{Z}) + \frac{\partial}{\partial x_i}(\bar{\rho}\tilde{u}_i\tilde{Z}) = \frac{\partial}{\partial x_i}\left(\overline{\rho D\frac{\partial Z}{\partial x_i}}\right) - \frac{\partial}{\partial x_i}(\overline{\rho u_i'' Z''}) + \bar{\dot{\rho}}, \qquad (2.22)$$

$$\frac{\partial}{\partial t}(\bar{\rho}\widetilde{Z''^2}) + \frac{\partial}{\partial x_i}(\bar{\rho}\tilde{u}_i\widetilde{Z''^2}) = \frac{\partial}{\partial x_i}\left(\overline{\rho D\frac{\partial Z''^2}{\partial x_i}}\right) - \frac{\partial}{\partial x_i}(\overline{\rho u_i'' Z''^2}) - 2\overline{\rho u_i'' Z''} - \bar{\rho}\tilde{\chi} + \overline{\sigma_s}, \quad (2.23)$$

10

where $\bar{\dot{\rho}}$ is the mixture fraction source term due to evaporation, $\widetilde{Z''^2}$ the mixture fraction variance, and $\overline{\sigma_s}$ the mixture fraction variance source term due to evaporation. The turbulent flux can be closed with the gradient assumption as

$$\widetilde{u_i''Z''} = -D_t \frac{\partial \widetilde{Z}}{\partial x_i}. \tag{2.24}$$

The mean scalar dissipation rate is defined as

$$\widetilde{\chi} = 2D\Big(\frac{\partial \widetilde{Z}}{\partial x_i}\frac{\partial \widetilde{Z}}{\partial x_i}\Big). \tag{2.25}$$

The mean scalar dissipation rate is usually modelled as a function of the turbulent kinetic energy and the turbulent dissipation rate as

$$\widetilde{\chi} = c_\chi \frac{\widetilde{\varepsilon}}{\widetilde{k}}\widetilde{Z''^2}, \tag{2.26}$$

where c_χ is a constant and usually taken to be 2 [22]. The source term of the mixture fraction equation $\bar{\dot{\rho}}$ is the same source term of the continuity equation. There are different methods to model the source term of the variance equation $\overline{\sigma_s}$. In RANS computations, the source term is expressed as [23]

$$\overline{\sigma_s} = \bar{\dot{\rho}}\widetilde{Z''^2}(1 - 2\widetilde{Z})/\widetilde{Z}. \tag{2.27}$$

Equation 2.27 is an approximation based on several assumptions, as described in [23]. In the current simulations, $\overline{\sigma_s}$ modeled following Eq. 2.27 is found to be very small, only resulting in $\widetilde{Z''^2}$ changes smaller than 1% for the flames selected in this study.

2.4   Large Eddy Simulation (LES)

In LES, the large scale three-dimensional unsteady turbulent motions are fully resolved, while the small scale motions are modelled. LES is far less computationally expensive when compared to DNS, while providing solutions with acceptable accuracy. Compared to RANS models, LES is more accurate since the large scales are fully resolved. To perform LES calculations, a filtering process should be carried out to decompose the instantaneous velocity into a resolved component which represents the large scale motion and a residual or sub-grid scale (SGS) component that is modelled.

$$U(x,t) = \overline{U}(x,t) + u'(x,t), \tag{2.28}$$

11

where $U(x,t)$ is the instantaneous velocity, $\overline{U}(x,t)$ the resolved component, and $u'(x,t)$ the SGS component. Equation 2.28 is substituted in the governing equations to obtain the filtered equations. However, unclosed SGS terms arise and they need modeling. The eddy viscosity concept is commonly used to close the SGS tensor as

$$\tau_{ij}^{sgs} = -2\mu_t \tilde{S}_{ij}. \tag{2.29}$$

The turbulent viscosity μ_t can be closed by Smagorinsky model [24].

$$\mu_t = \overline{\rho}(C_s \Delta)^2 ||\tilde{S}||, \tag{2.30}$$

where Δ is the filter size, $||\tilde{S}||$ the Frobenius norm of the resolved shear stress tensor $\sqrt{2\tilde{S}_{ij}\tilde{S}_{ij}}$, and C_s is Smagorinsky constant. C_s usually takes values between 0.05 and 0.2 depending on the configuration. The dynamic SGS model [25] can also be used to close the SGS terms. The filtered equations are then solved to obtain the filtered quantities that correspond to the large scale motions. Further discussion of the LES equations are provided in Chapter 7 where the LES investigation is also presented.

2.5 Direct Numerical Simulations (DNS)

DNS resolves all the time and length scales. The smallest scales in the simulation are of the order of the Kolmogorov length scale, η, which is a function of the Reynolds number as [16]

$$\eta \approx Re^{-3/4}l, \tag{2.31}$$

where Re is the turbulence Reynolds number defined as $u'l/\nu$ with u' being the velocity rms, and l the integral length scale which is the size of the large energy containing eddy. The typical grid size of an acceptable DNS simulation must be of the order of the Kolmogorov scale. Therefore, for three-dimensional isotropic turbulence, the number of grid points can be estimated using

$$N_{cell} \approx \left(\frac{L_{box}}{\eta}\right)^3 \approx \left(\frac{L_{box}}{l}\right)^3 Re^{9/4}, \tag{2.32}$$

where N_{cell} the number of numerical cells, and L_{box} the domain length. The number of computational cells increases exponentially with the Reynolds number. Consequently, it is too expensive to perform DNS for large scale devices at high Reynolds numbers.

2.6 Summary

This chapter introduces the governing equations and different models to describe the gas phase. First, the transport equations of mass, momentum, species, and energy are given. Then, turbulent flows are defined and different approaches of turbulent modeling including RANS, LES, and DNS are introduced. The Favre-averaged equations for RANS are discussed with different modeling approaches for the unclosed terms. The k-ε model used in the current study which is known to overpredict the spreading rate of axisymmetric jets, is reviewed. Therefore, some constants are commonly varied to obtain the optimum mixing field. The mixture fraction is then defined which plays an important role in describing non-premixed combustion. In spray combustion, the mixture fraction is not a conserved scalar due to spray evaporation.

Chapter 3

Liquid Phase Formulation

Different approaches are available to model liquid sprays. These approaches vary in accuracy, complexity and computational times. The most common methods of two-phase flow modeling and the adopted approach in the current study are presented in this chapter. Sprays and other dispersed flows may be divided into dilute and dense regimes [10, 26]. Dilute sprays commonly assume spherical droplets with small volume fractions. They are easier to model since droplet collisions are more infrequent. Further, the heat transfer, mass transfer and drag coefficients of individual droplets are not directly influenced by the adjacent droplets. Dense sprays may exist near the exit of an injector where the transition between the liquid jet and the dilute spray occurs. Dense sprays are characterized by large volume fractions and irregularly shaped elements. Modeling dense sprays is much more challenging than dilute sprays due to additional complex phenomena such as the collisions and breakup of liquid elements [26, 27], that need to be considered. In the current study, for simplicity, only dilute sprays are considered with suitable experimental data [7]. Two-way coupling is implemented where the interacting effects of the gas and liquid phases are accounted for [28].

3.1 Fully Resolved Droplet

In this approach, all the physical scales down to the droplet size, boundary layer, and flame thickness are resolved. This approach is the most accurate approach that is usually used to obtain statistics and to validate empirical models. For instance, Wu and Sirignano [29, 30, 31] used fully resolved three-dimensional DNS of droplet arrays burning in stagnant and convective environments. Wang et al. [32, 33] also studied fully resolved DNS of

droplet array combustion in turbulent convective flows, and they modeled the mixing fields in an inter-droplet space. This approach is computationally costly and only feasible for a small number of particles. Thus, this method is currently not applicable to actual spray-combustion processes.

3.2   Eulerian-Eulerian Approach

In this method, the Eulerian description is used to represent the gas phase and it is also used for the liquid phase where the liquid spray is considered a continuum [34]. To use the Eulerian approach, the continuum assumption must be valid [34, 35]. For the assumption to be valid, each computational cell must contain a large number of droplets. Moreover, the droplet size should be smaller than the Kolmogorov microscale, η. In addition, the distances between droplets should be at least an order of magnitude smaller than η [28]. Additional transport equations are solved to describe the spray as a continuous medium. Spray dispersion is accounted for in the governing equations and no separate dispersion model is required like the case in the Lagrangian approach [28]. The Eulerian approach is suitable when the number of droplets is large and the droplets are small. Nevertheless, this approach can be very computationally expensive if particles of various sizes in the dispersed phase of a disperse system (polydispersed system) is considered. In this case, a transport equation for each particle size range is solved [36]. The two-phase flow can be treated as a single phase if the Stokes number (which describes the particle response time) is very small. The Stokes number is defined as the ratio of the characteristic time of a droplet to a characteristic time of the flow. The energy and momentum changes between the two phases are considered source terms in the governing equations.

3.3   Eulerian-Lagrangian Approach

In this approach, the Eulerian method is used to describe the gas phase, while the Lagrangian description is considered to obtain the spray characteristics [37]. This approach is adopted in the current study with two-way coupling. Two-way coupling is achieved such that the mutual effects between the gas phase and liquid phase are considered. In the Lagrangian method, the liquid phase is discretized into computational parcels which are described by Lagrangian coordinates. A parcel is a group of identical droplets with the same properties such as size, mass, velocity, and temperature. This representation allows saving the computational resources for large number of droplets where the resolution of

each droplet is not feasible. The parcels are subjected to several processes such as atomization, break-up, collision, evaporation, heat transfer and turbulence [27]. The source terms due to the gas-spray interaction in the gas phase equations are calculated from the Lagrangian solver. To completely describe the governing equations of spray in Lagrangian framework, several spray sub-models should be introduced. The spray sub-models used in OpenFOAM are discussed in the following subsections.

3.3.1   Model formulation

Spray Motion Equation

The motion of any Lagrangian particle moving in an Eulerian grid is governed by Newton's second law as

$$\sum F_i = m_d \frac{du_{d,i}}{dt}, \tag{3.1}$$

where F_i is the force acting on the droplet in i direction, m_d the droplet mass, and $u_{d,i}$ the droplet velocity in i direction. Forces acting on the droplet include added mass force, pressure gradient, drag force, and gravitational forces [38]. Most of these forces can be neglected due to the high density ratio between the liquid and gas phases [39]. The current study considers the drag forces and the gravitational forces only.

$$\sum F_i = F_D + F_g + F_x, \tag{3.2}$$

where F_D is the drag force and F_g the gravitational force. F_x is the force due to added mass and pressure gradient which is usually neglected in spray flames. F_x and F_D can be expressed as

$$F_x = \frac{m_d \pi D^3 \rho_d}{12} \frac{d(U - u_d)}{dt} + \frac{1}{6}\pi D^3 \nabla p, \tag{3.3}$$

$$F_D = -\rho_g \frac{\pi D^2}{8} C_D (u_d - U)|u_d - U|, \tag{3.4}$$

where ρ_g is the carrier gas density, D the droplet diameter, C_D the drag coefficient, and U the instantaneous gas velocity. The drag coefficient can be calculated using several methods. In the current work, all the droplets are assumed to be spherical and the drag coefficient is obtained from an empirical relation [40] as

$$C_D = \begin{cases} \frac{24}{Re_d}(1 + \frac{Re_d^{\frac{2}{3}}}{6}), & Re_d < 1000, \\ 0.424, & Re_d > 1000, \end{cases} \tag{3.5}$$

where Re_d is the droplet Reynolds number. The gravitational force is calculated as

$$F_g = \rho_d \frac{\pi D^3}{6} g. \tag{3.6}$$

where g is the gravitational acceleration. Combining Equations 3.1, 3.2, 3.4, and 3.6 leads to Equation 3.7

$$\frac{du_{d,i}}{dt} = -\frac{\rho_g}{\rho_d} \frac{1}{D} C_D (u_d - U)|u_d - U| + g, \tag{3.7}$$

To simplify Equation 3.7, a momentum relaxation time is defined as:

$$\tau_u = \frac{8 m_d}{\pi \rho_g C_D D^2 |u_d - U|} = \frac{4}{3} \frac{\rho_d D}{\rho_g C_D |u_d - U|}. \tag{3.8}$$

Finally, Equation 3.7 can be written as:

$$\frac{du_{d,i}}{dt} = -\frac{u_d - U}{\tau_u} + g. \tag{3.9}$$

Evaporation Model

It is essential to accurately predict spray evaporation from a reliable evaporation model since the mass and heat transfer between the gas phase and the liquid phase are calculated directly from the evaporation model. The source terms in the continuity and enthalpy equations are calculated from the mass and heat transfer between the two phases. In spray combustion, liquid droplets are usually surrounded by hot gases. The heat transfers from the hot gases to the droplets resulting in a temperature rise of the droplets. Thus, the droplets begin to evaporate after reaching the boiling point and the vapor diffuses into the surrounding hot gases. Several models for this process can be found in the literature [41, 42]. The Spalding evaporation model [43] is used in the current study. The evaporation model is based on the infinite liquid conductivity model which assumes a uniform droplet temperature in which the temperature of the droplet surface equals the inside temperature of the droplet and changes only with time. The change of droplet mass with respect to time can be expressed as

$$\frac{dm_d}{dt} = \pi D Sh D_{i,m} \rho_\infty ln\left(1 + B_m\right), \tag{3.10}$$

where m_d is the droplet mass, Sh the Sherwood number, ρ_∞ the density of the bulk gas, $D_{i,m}$ the diffusion coefficient of the vapor in the bulk gas, and B_m is the Spalding Mass

number given by

$$B_m = \frac{Y_{v,s} - Y_{v,\infty}}{1 - Y_{v,s}}, \tag{3.11}$$

where $Y_{v,s}$ is the vapor mass fraction at the droplet surface, and $Y_{v,\infty}$ the vapor mass fraction of the bulk gas. The 1/3 rule is used for the temperature and vapor mass fraction to determine the reference point for the averaged properties within the film vapor. The Sherwood number is given by the Ranz-Marshall correlation for mass transfer [44] as follows

$$Sh = 2 + 0.6\sqrt{Re}(Sc)^{\frac{1}{3}}, \tag{3.12}$$

where Sc is the Schmidt number. The heat transfer model is based on the convective heat transfer of a particle with a uniform temperature. The droplet temperature is determined using the heat balance equation. The rate of change of the droplet temperature can be expressed as

$$\frac{dT_d}{dt} = \frac{\pi D k_\infty Nu}{m_d c_{p,v}}(T_\infty - T_d)f_{heat} - \frac{h_{fg}\dot{m}_d}{c_{p,v}m_d}, \tag{3.13}$$

where T_d is the droplet temperature, k_∞ the thermal conductivity of the bulk gas, $c_{p,v}$ the specific heat capacity of the bulk gas, Nu the Nusselt number, f_{heat} the correction factor for the interphase thermal transfer of evaporating droplets, h_{fg} the latent heat of vaporization, and $\dot{m}_d$ the rate of evaporation. The Nusselt number is calculated from the Ranz-Marshall correlation as

$$Nu = (2 + 0.6\sqrt{Re}(Pr)^{1/3}), \tag{3.14}$$

and the correction factor is calculated as

$$f_{heat} = \frac{-\frac{c_{p,v}\dot{m}_d}{\pi D k_\infty Nu}}{e^{-\frac{c_{p,v}\dot{m}_d}{\pi D k_\infty Nu}} - 1}. \tag{3.15}$$

Finally, the source terms added to the governing equations can be summarized as follows

$$\bar{\dot{\rho}} = \frac{1}{V}\sum_{n=1}^{N} n_{d,n}\dot{m}_{d,n}, \tag{3.16}$$

$$\bar{\dot{F}} = \frac{1}{V}\sum_{n=1}^{N} n_{d,n}m_{d,n}\left(-\frac{4}{3}\frac{(u_d - U)|u_d - U|\rho_g C_D}{\rho_d D} + g\right), \tag{3.17}$$

$$\bar{\dot{Q}} = \frac{1}{V}\sum_{n=1}^{N} n_{d,n}m_{d,n}\left(\frac{(T_\infty - T_d)\pi D k_\infty Nu}{m_d c_{p,v}}f_{heat} - \frac{6h_{fg}T_d ShD_{i,m}\rho_\infty ln(1 + B_m)}{c_{p,v}\rho_d D^2}\right), \tag{3.18}$$

18

where N is the number of parcels inside the computational cell, $n_{d,n}$ the number of droplets per parcel, and V the computational cell volume.

3.3.2 Numerical implementation

Parcel Tracking

The liquid particles move in a fixed Eulerian grid. Knowing the position and the velocity of the particle is crucial to accurately predict the source terms in each cell. OpenFOAM uses the Face-To-Face tracking algorithm [45]. Starting with the location and speed of the parcel, the parcel is tracked until it reaches the cell boundary, or for the entire time step if it is still in the same cell. If the parcel changes the cell, the time it takes to leave the first cell is calculated, and the parcel properties are updated. The momentum change is then added to the current cell. Then, the process is started again for the new cell. The Face-To-Face tracking in OpenFOAM includes an additional stability check that begins by tracking the parcel from the centre of the cell it belongs to, rather than from the particle's position. This is done to ensure that particles close to the edge of the cell are properly tracked. This algorithm does not skip cells which improves the predictions of all the source terms that couple the two phases.

Turbulent Dispersion Model

To model the turbulent dispersion of discrete particles, a stochastic dispersion model using discrete random walk method is used [46]. Each particle in the domain is tracked using the tracking model. The droplets disperse by the turbulent flow. The droplets take different paths as a result of the turbulent dispersion. It is very important to accurately predict the trajectories of the droplets because the location of the droplets affects the source terms in the Eulerian gas equations [47]. To solve Equation 3.9 which describes the motion of a particle in a flow field, it is required to calculate the instantaneous gas velocity as

$$U = \tilde{u} + u_i'(t), \tag{3.19}$$

where $\tilde{u}$ is the mean velocity and $u_i'(t)$ the turbulent fluctuation. $u_i'(t)$ can be calculated by means of root mean square (RMS) of the velocity fluctuation, a Gaussian probability distribution and assumption of isotropic turbulence in the three directions. OpenFOAM uses discrete random walk model to simulate the interaction of the droplets with the

turbulent eddies of the gas phase following Dukowicz [48]. The velocity is perturbed in random direction, with a Gaussian random number distribution with zero mean and the variance is the local RMS value of the velocity fluctuations $\sqrt{\overline{u'^2}}$.

$$u' = \zeta \sqrt{\overline{u'^2}}, \tag{3.20}$$

where ζ is a random number with normal distribution. The RMS velocity fluctuations are calculated from the turbulent kinetic energy assuming isotropic turbulence as

$$\sqrt{\overline{u'^2}} = \sqrt{\frac{2}{3}k}, \tag{3.21}$$

Injection Model

The injection model introduces the spray droplets to the computational domain. A PDF of the droplet diameters has to be defined at the injection location. The injection model also determines the number of droplets, the injection velocity and injection angle of each parcel. The direction angle of each droplet is calculated by multiplying the maximum injection angle defined by the user and a random number between 0 and 1 [39]. The injection velocity can be defined directly or calculated from the injection pressure difference as

$$u_d = C_d \sqrt{\frac{2\Delta p}{\rho_i}}, \tag{3.22}$$

where ρ_i is the density of the parcel, C_d the discharge coefficient and Δp the pressure difference. The number of droplets is determined by the supplied PDF for droplet diameters, droplets initial velocity, and the mass flow rate of the injected spray. OpenFOAM introduces several probability distributions to describe the droplet diameters distribution such as: uniform distribution, normal distribution, exponential distribution, multi-normal distribution, and Rosin-Rammler distribution. The Rosin-Rammler distribution [49] is widely used to describe the size distribution of sprays. The droplet size distributions are determined based on the minimum and maximum diameter of the droplets and are divided into several discrete intervals with each interval specified by a mean diameter. This can be used to calculate the mass fraction of the droplets with diameters greater than the mean diameter in a particular size interval as

$$Y_d = exp^{-(d/\bar{d})^n}, \tag{3.23}$$

where n is the spread parameter of the droplets, Y_d the mass fraction of droplets with diameter greater than d in a particular size interval, d the droplet diameter, and $\bar{d}$ the

mean diameter. This model requires the droplet minimum, maximum and mean diameters as well as the spread parameter. Any size distribution can be obtained using the Rosin-Rammler exponential equation by adjusting the values of the mean diameter and the spread parameter. To determine these parameters, the particle size data should fit the Rosin-Rammler exponential equation.

3.4 Summary

This chapter reviews the different methods of describing the liquid phase. It starts with the fully resolved droplets in which all the scales are resolved. This approach is very accurate, but it is computationally expensive for practical applications. In the Eulerian-Eulerian approach, the gas and liquid phases are treated as continuum and represented by Eulerian equations. The Eulerian approach is suitable when large numbers of small droplets are included. However, this approach can be very computationally expensive if a polydispersed system is considered. In the current study, the Eulerian-Lagrangian approach is adopted in which the Lagrangian approach is used to obtain the spray characteristics. The formulation of the Lagrangian model and the different submodels are discussed such as the droplet motion equations, parcel tracking, and injection model. In the current study, a stochastic dispersion model is considered to account for turbulent dispersion. The evaporation model and the underlying assumptions are also stated.

Chapter 4

Turbulent Combustion modeling

4.1 Turbulent combustion models

The governing equations of turbulent flows are presented in Section 2.3. There are different unclosed terms in the governing equations due to averaging in RANS or filtering in LES. Turbulent combustion models are developed to close the mean or filtered chemical source term $\bar{\dot{\omega}}_k$ in the species equation (See Equation 2.10). Several models have been developed such as Eddy Break Up (EBU) model [22], and Eddy Dissipation Model (EDM) [18], flamelet model [50], Conditional Moment Closure (CMC) [51], Conditional Source-term Estimation (CSE) [52], PDF methods [18], and Multiple Mapping Conditioning (MMC) [53]. A summary of these models is presented in this chapter.

4.1.1 Eddy Break Up model

The Eddy Break Up (EBU) model is one of the first attempts to close the mean chemical reaction rates. EBU is based upon the infinitely fast chemistry assumption which assumes that the reaction occurs much faster than the rate of mixing of reacting species. This assumption is found to be reasonable to study the global properties in turbulent combustion. The mean reaction rate is a function of the rate of mixing between the reactants and hot products which is carried out by turbulence effect. Thus, the mean/filtered reaction rates can be expressed as [18]

$$\widetilde{\dot{\omega}}_P = C_{EBU} \frac{\varepsilon}{k} \sqrt{\widetilde{Y_p''^2}}, \tag{4.1}$$

where P denotes a product species, C_{EBU} is a model constant, and $\widetilde{Y_p''^2}$ the variance of the product mass fraction. This approach is considered the fastest approach due to its high simplicity. However, it commonly produces higher reactive scalars. In addition, detailed chemistry cannot be incorporated in the EBU model.

4.1.2 Eddy Dissipation Model (EDM)

The Eddy Dissipation Model (EDM) is based on the EBU concept by considering the fuel, oxidizer, and products [54]. The closure of the mean reaction rate is given by [18]

$$\widetilde{\dot{\omega}}_F = A\frac{\varepsilon}{k}min\Big(\widetilde{Y}_F, \frac{\widetilde{Y}_{Ox}}{S}, B\frac{\widetilde{Y}_P}{1+S}\Big),$$ (4.2)

where Ox indicates oxidizer, F stands for fuel, S is the oxygen-fuel stoichiometric mass ratio, and A and B are model parameters. Although EDC provides a low computational cost, it has strong limitations. The parameters A and B are flame specific and require adjustments for each flame [18]. Thus, the model requires validation for each flow. Further, the model presents a less accurate description of turbulent temperature fluctuation [55].

4.1.3 Laminar Flamelet model

The Laminar Flamelet model assumes that turbulent diffusion flames consist of an ensemble of stretched laminar flamelets. The flame properties can be characterized within the reaction zone using different parameters. Diffusion flames are controlled by the degree of mixing of the fuel and the oxidizer where the mixture fraction can be used to describe non-premixed combustion. Therefore, the spatial coordinate perpendicular to the flame surface can be transformed to the mixture fraction space. In this context, the Favre-averaged mass fraction of species k can be written as

$$\widetilde{Y}_k(x,t) = \int_0^1 \int_0^\infty Y_k(Z, \chi_{st}, x, t)\widetilde{P}(Z, \chi_{st}, x, t)d\chi_{st}dZ,$$ (4.3)

where χ_{st} is the scalar dissipation at the flame surface, $\widetilde{P}$ a presumed PDF, and $Y_k(Z, \chi_{st}, x, t)$ an ensemble of laminar flamelets at different strain rates and is tabulated prior to the CFD calculations. The steady or unsteady flamelet equations are commonly solved to construct the chemistry library. It is worth noting that the Laminar Flamelet model is limited to the flamelet regime where the flame structure is not strongly distorted.

4.1.4 Conditional Moment Closure

Conditional Moment Closure (CMC) was first proposed by Bilger [56] and Klimenko [57], independently. The model uses the conditional averages to retrieve the unconditional averages since the fluctuations about the conditional mean are much smaller compared to the unconditioned means. The mixture fraction is commonly used as a conditioning variable in non-premixed combustion. Thus, any mean scalar can be obtained from its conditional mean as follows

$$\widetilde{Q} = \int_0^1 \langle Q|\eta\rangle \widetilde{P}(\eta)d\eta \tag{4.4}$$

where $\langle Q|\eta\rangle$ is the conditional average of $\widetilde{Q}$ conditioned on the sample space of the mixture fraction η and $\widetilde{P}$ a presumed PDF. In CMC, the conditional averages are determined by solving their transport equations in mixture fraction space. For high Reynolds number and unity Lewis number, the conditionally filtered equations for species k can be expressed as

$$\frac{\partial Y_k}{\partial t} + \widetilde{u_i|\eta}\frac{\partial Y_k}{\partial x_i} + e_f = \widetilde{N|\eta}\frac{\partial^2 Y_k}{\partial \eta^2} + \widetilde{\dot{\omega}_k|\eta}, \tag{4.5}$$

where $\widetilde{u_i|\eta}$ is the conditional velocity, $\widetilde{N|\eta}$ the conditional scalar dissipation rate, e_f the conditional turbulent flux, and $\widetilde{\dot{\omega}_k|\eta}$ the conditional reaction rate. Thus, it can be seen that many unclosed terms arise in the CMC equations and further modeling is required. First order closure for the conditional chemical source term can be achieved by neglecting the fluctuations about the conditional mean. Hence, the conditional reaction rates can be written as

$$\langle \dot{\omega}_k|\eta\rangle \simeq \dot{\omega}(\langle Y_k|\eta\rangle, \langle T|\eta\rangle, \langle \rho|\eta\rangle). \tag{4.6}$$

Additional models to close the conditional velocity, the conditional scalar dissipation rate and the conditional turbulent flux are required. Unlike the laminar flamelet model, CMC is not limited to the flamelet regime. Nevertheless, the computational cost of CMC is expected to be higher.

4.1.5 PDF methods

The method of solving a modelled PDF equation started in 1969 when Lundgren derived, modelled, and solved a transport equation for the joint PDF of velocity [58]. Later, Pope derived, modelled, and solved a transport equation for the composition joint PDF including a set of scalars [59]. In the PDF method, the joint PDF is not presumed and a transport

equation of the joint PDF of velocity, viscous dissipation and reaction scalars is solved. This method can be applied to any combustion regime. In addition, the chemical source term appears in a closed form and no modeling is required. Therefore, it is considered one of the most complete descriptions of turbulent reacting flows [18]. The joint PDF transport equation does not contain any information of the mixing time and a closure of this mixing term is required. Providing closure for this term results in higher computational cost. However, the Monte-Carlo simulation technique using Lagrangian methods can be used to reduce the computational cost [60]. The PDF methods are mathematically complex and computationally expensive. Further, providing closure for the mixing term is not simple and the predictions quality relies on this closure. Further information about the PDF method can be found in [61].

4.1.6 Multiple Mapping Conditioning

Multiple Mapping Conditioning (MMC) was first developed by Klimenko and Pope [53]. The MMC model is built upon both CMC and the PDF method and combines their advantages. MMC model can reduce the computational requirements by conditioning the mixing of the stochastic particles on a reference field that ensures localness of particle mixing in composition space. This allows for a significant reduction in stochastic particle numbers and a substantial increase in computational efficiency [62]. Although this model is computationally less expensive compared to the PDF methods, further reduction in the computational cost is still required for complex geometries.

4.2 Conditional Source-term Estimation (CSE)

Conditional Source-term Estimation (CSE) was first developed to close the chemical source-term in averaged transport equations for non-premixed turbulent combustion. CSE takes advantage of the same closure approximation as in CMC, but does not solve any additional transport equations. Instead, an integral inversion is performed, as discussed in Section 4.2.2. Therefore, no additional models are required for the unclosed conditional terms in Equation 4.5, as emphasized in Section 4.1.4.

CSE has some interesting features [63]; it can be applied to any turbulent flame regime in any configuration. In addition, no additional transport equations or closures are introduced to calculate the mean reaction rates. Further, detailed chemistry mechanisms can be included by using chemistry reduction methods where the reaction rates are calculated and

tabulated prior to the simulation. CSE has been successfully applied to model turbulent combustion in non-premixed cases for methane and methanol [11, 12, 64, 65, 66, 67, 68]. It has been also used for premixed flames in RANS and LES [69, 70, 71, 72], and multi-stream configurations [73, 74]. Doubly Conditional Source-term Estimation (DCSE) has been developed to simulate partially premixed flames [75, 76, 77]. Therefore, the current study aims at extending CSE for gas combustion to simulate turbulent spray flames. The current section describes the CSE formulation of spray combustion.

4.2.1 Concept

CSE uses the concept of conditional averages to determine the unconditional Favre-averaged quantities in a turbulent reacting flow. In non-premixed flames, the conditioning variable is taken to be the mixture fraction. Thus, the conditional average of any scalar is calculated at a specific mixture fraction value η in mixture fraction space. First order closure for the conditional chemical production rate is applied which assumes that the fluctuations about the conditional average are negligible. This assumption has been shown to be reasonable for attached jet flames far from extinction and without ignition [51] and was successfully applied to previous CSE studies of attached non-premixed turbulent flames [12, 68]. In CSE, the conditional chemical source term $\langle \dot{\omega}_k | \eta \rangle$ can be calculated as a function of a selected number of species

$$\langle \dot{\omega}_k | \eta \rangle \simeq \dot{\omega}(\langle Y_k | \eta \rangle), \tag{4.7}$$

where $\langle Y_k | \eta \rangle$ is the conditional average of species k. In general, any species could be selected to obtain the conditional chemical reaction rate $\langle \dot{\omega}_k | \eta \rangle$ from Equation 4.7. However, the selection is determined based on the fuel used and its corresponding chemical mechanism. The conditional mass fractions of carbon dioxide (CO_2) and water (H_2O) have been commonly used along with CSE for methane and methanol combustion under multiple conditions and proved to provide good predictions [11, 12, 64, 65, 66, 67, 68]. They are commonly selected due to their long formation times [66] leading to accurate representation of the thermo-chemical state. Therefore, the conditional mass fractions of CO_2 and H_2O are used in the current study and the conditional reaction rates can be expressed as

$$\langle \dot{\omega}_k | \eta \rangle \simeq \dot{\omega}(\langle Y_{CO_2} | \eta \rangle, \langle Y_{H_2O} | \eta \rangle), \tag{4.8}$$

where $\langle Y_{CO_2} | \eta \rangle$ and $\langle Y_{H_2O} | \eta \rangle$ are the conditional mass fractions of CO_2 and H_2O, respectively. The unconditional Favre-averaged equations are solved and the conditional averages can be obtained by inverting the following integral

$$\widetilde{Y}_k(x_j, t) = \int_0^1 \langle Y_k | \eta \rangle (\eta, x_j, t) \widetilde{P}(\eta, x_j, t) d\eta, \tag{4.9}$$

26

where (x_j) is the spatial coordinate, t the simulation time, $\widetilde{Y}_k(x_j, t))$ is the Favre-averaged mass fractions obtained by solving Equation 2.10 and $\widetilde{P}(\eta, x_j, t)$ is the Favre-averaged pdf of mixture fraction. A presumed β distribution is selected to model $\widetilde{P}$ [78]. The β-PDF is calculated as follows

$$\beta_{pdf}(x, a, b) = \frac{1}{B(a, b)} x^{a-1}(1 - x)^{b-1}, \tag{4.10}$$

$$B(a, b) = \frac{\Gamma(a)\Gamma(b)}{\Gamma(a+b)}, \tag{4.11}$$

where $\Gamma(x)$ is the Gamma function, a and b can be calculated as

$$a = \overline{x}\Big(\frac{\overline{x}(1 - \overline{x})}{\sigma^2} - 1\Big), \tag{4.12}$$

$$b = (1 - \overline{x})\Big(\frac{\overline{x}(1 - \overline{x})}{\sigma^2} - 1\Big), \tag{4.13}$$

where $\overline{x}$ is the mean value of the mixture fraction and σ^2 is the variance.

The mean unconditional reaction rates can then be calculated from the conditional means using

$$\overline{\dot{\omega}_k}(x_j, t) = \overline{\rho} \int_0^1 \frac{\langle \dot{\omega}_k | \eta \rangle}{\langle \rho | \eta \rangle} \widetilde{P}(\eta, x_j, t) d\eta. \tag{4.14}$$

The unconditional mass fractions are determined using Equation 4.9, where in the current implementation, the terms $\langle \dot{\omega}_k | \eta \rangle$ and $\langle Y_k | \eta \rangle$ are obtained from the chemistry tables as a function of the two conditional species mass fractions $\langle Y_{H_2O} | \eta \rangle$ and $\langle Y_{CO_2} | \eta \rangle$.

In principle, CSE does not require any chemistry tabulation and all conditional species mass fractions can be obtained by integral inversion. However, the use of tabulated chemistry significantly reduces the computational cost by lowering the number of required inversions. Further, common techniques like zeroth order Tikonov method [79], selected in the present study, do not enforce conservation of mass in the inversion process. Therefore, a large number of inversions to obtain a large number of conditional species mass fractions would result in increased inaccuracies for mass conservation in the mixture fraction space. Other inversion techniques may be derived to add specific constraints like the conservation of mass [80], but these are not straightforward to implement and are beyond the scope of the current work.

As for the choice of the tabulated chemistry, CSE is not linked to any particular chemistry tabulation technique and different methods could have been considered [81]. In the present study, the Trajectory Generated Low Dimension Manifold (TGLDM) approach [66, 82] is selected due to previous successful implementations [11, 12, 65, 66, 67, 68]. Further detail

on TGLDM is given in Section 4.3. The current implementation of TGLDM requires the input of the conditional mass fractions of CO_2 and H_2O. Therefore, an inversion process is required to obtain these species conditional mass fractions from the Favre-averaged mass fractions.

4.2.2 Integral Inversion

The conditional averages are found to vary much less in space than unconditional averages [51]. Consequently, the conditional averages are assumed homogeneous within a known ensemble of points. The computational domain is divided into several ensembles with all the computational cells on each ensemble having the same conditional averages while each computational cell has its own pdf based on the mixture fraction mean and mixture fraction variance. Thus, for a given ensemble, the Favre-averaged mass fraction can be written as

$$\widetilde{Y}_k(x_j, t) = \int_0^1 \langle Y_k|\eta\rangle(\eta, t)\widetilde{P}(\eta, x_j, t)d\eta. \tag{4.15}$$

Equation 4.15 is written for one given ensemble, whereas Equation 4.9 is shown for any point in space without making any assumption on the conditional averages. In Equation 4.15, the conditional averages do not vary with x_j within a given ensemble.

The ensemble distribution depends on the flame being studied and a sensitivity analysis on the number of ensembles should be carried out to ensure that the solution does not depend on the number of ensembles. For axisymmetric jet flames, the computational domain is usually divided by a set of planes in the axial direction to take advantage of the weak radial dependence of the conditional averages. Equation 4.15 is a Fredholm integral of the first kind. Using a numerical quadrature for the left-hand side, Equation 4.15 can be expressed in general form as

$$A \cdot \vec{\alpha} = \vec{b}, \tag{4.16}$$

where $\vec{\alpha}$ is the vector including $\langle Y_k|\eta\rangle$ at each η_m, m is the mixture fraction bin index, $\vec{b}$ is the vector containing $\widetilde{Y}_k$ at each spatial position x_j, and A is the matrix of integrated pdf over a mixture fraction interval. The matrix A is of size $N \times M$, where N is the number of grid nodes in a given ensemble, and M is the number of bins in mixture fraction space. The matrix A can be calculated as

$$A_{jm} = \int_{\eta_1}^{\eta_2} \widetilde{P}(\eta_m, x_j, t)d\eta, \tag{4.17}$$

where j is the spatial coordinate index, η_1, and η_2 are the lower and upper bounds of the mixture fraction bin. The solution of Equation 4.16 is ill-posed which means it is sensitive

to any small perturbation in the system [83]. Consequently, a regularization method is required to obtain a smooth, stable, and unique solution. Tikhonov regularization [79] is selected in the present study and it can be implemented based on the least-square technique as

$$\vec{\alpha} = arg\ min\left\{\left|\left|\ A\vec{\alpha} - \vec{b}\ \right|\right|_2^2 + \lambda^2\left|\left|\ I(\vec{\alpha} - \vec{\alpha}_0)\ \right|\right|_2^2\right\}, \tag{4.18}$$

where $||.||_2$ is the L2-norm of a vector, I is the identity matrix, $\vec{\alpha}_0$ is the solution from the previous time step, and λ is the regularization parameter. The regularization parameter λ is defined as

$$\lambda^2 = \frac{Tr(A^TA)}{Tr(I)}, \tag{4.19}$$

where Tr is the trace of the matrix. In Chapter 5, LU decomposition is used to solve Equation 4.16. However, the Least-Squares QR-factorization (LSQR) algorithm is implemented in Chapter 6 and Chapter 7 since it provides much faster execution times which is crucial for DCSE and LES implementaions.

4.3   Chemistry Tabulation

The chemical reaction rates for the different species are tabulated prior to the simulation using the TGLDM approach [66, 82]. The detailed chemistry mechanism is reduced to low-dimensional manifolds in composition space. A TGLDM manifold for each mixture fraction is generated and stored in tables using the mass fraction of CO_2 and H_2O due to their long formation times [66]. Reaction trajectories in the manifold are constructed by integrating the following system of equations

$$\rho\frac{\partial Y_k}{\partial t} = \dot{\omega}_k, \tag{4.20}$$

where $\dot{\omega}_k$ is the reaction rate vector given by the detailed chemistry mechanism. A stiff Ordinary Differential Equation (ODE) system solver is used to solve Equation 4.20 starting at each boundary point. The calculations stop when chemical equilibrium is reached.

In the present TGLDM method, there is no strain rate term in the laminar flame equations solved, as shown in Equation 4.20. However, many trajectories are included for a given mixture fraction value covering the reacting states between the pure mixing to fully-burnt (chemical equilibrium) limits. For illustration, Figure 4.1 shows the 54 trajectories generated for acetone combustion at the stoichiometric mixture fraction. This
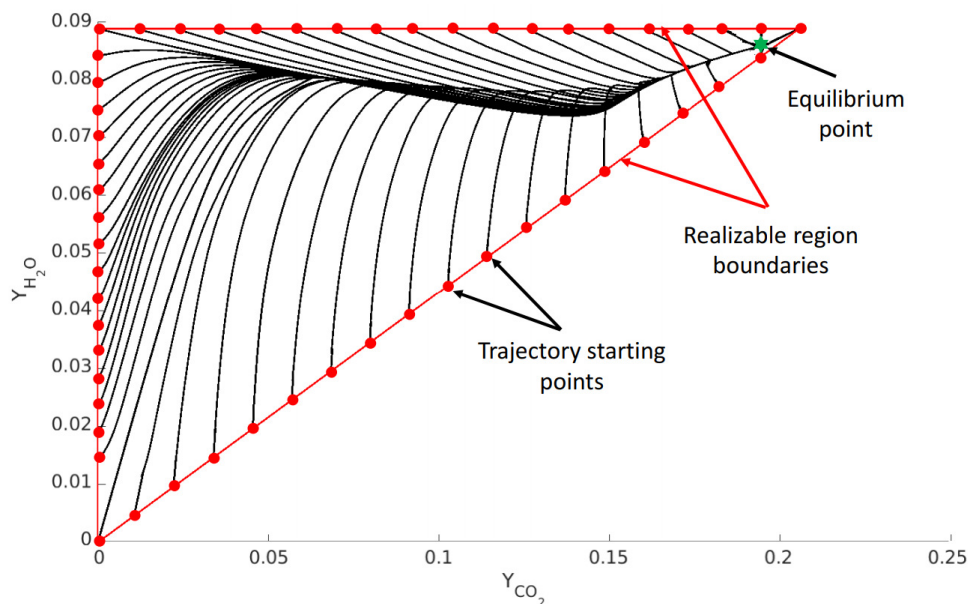
Figure 4.1: Trajectories generated by solving Equation 4.20 showing the initial points, pure mixing limit and equilibrium point for the stoichiometric mixture fraction for acetone combustion

set of trajectories with associated species mass fractions and reaction rates corresponds to one manifold. As shown in Figure 4.1, the trajectories start from different initial points and the time evolution of each trajectory is kept towards the equilibrium point. The longest trajectory consists of 955 points and the shortes has 11 points. The redundant points are then removed to reduce the table size. Delaunay triangulation is applied to facilitate locating the points in the manifold [84].

For flames with significant levels of extinction and reignition, CSE needs to be extended to DCSE and the chemistry tables would have one additional dimension due to the addition of a progress variable [77]. The resulting tables are three dimensional including η, Y_{CO_2} and Y_{H_2O} subspaces.

The present chemistry tables are initially adiabatic. Radiation is included in Equation 2.11 for the Favre averaged enthalpy, but its direct effect is neglected on the conditional chemical source terms and species mass fractions in the chemistry tables. This approximation has been used in previous CSE studies with good predictions, but is expected to fail when a large amount of radiation is present [68]. Likewise, as a first step, the effects of spray are not included in the current chemistry tabulation. This assumption is also applied to the previously published numerical studies including tabulated chemistry that are used

herein for comparison [4, 85, 86, 87, 88]. In order to include evaporation effects in the tabulated chemistry, one additional dimension would need to be added like an enthalpy deficit [89, 90]. The impact of this assumption is further investigated in Chapter 7.
Several detailed chemistry mechanisms are available for acetone combustion. Chong and Hochgreb [91] have extended GRI-MECH 3.0 by an additional acetone sub-mechanism of 7 reactions. The full acetone mechanism consists of 56 species and 332 reactions. Fifty TGLDM manifolds are tabulated for 50 different values of η ranging from 0.001 to 0.99, with a finer resolution around the stoichiometric mixture fraction ($\eta_{st} = 0.095$). The number of bins was doubled from 50 to 100 to make sure that the solution is independent of the number of bins. No significant change could be detected in the results. Therefore, 50 bins are deemed sufficient for the present conditions and used in all simulations presented in current work. For ethanol combustion, Marinov detailed chemistry mechanism for ethanol [5] is implemented including 56 species and 383 reactions.

The conditional chemical source terms are determined from the chemistry tables based on $\langle Y_{CO_2}|\eta \rangle$ and $\langle Y_{H_2O}|\eta \rangle$ that were previously calculated from the inversion process. The conditional reaction rates and the conditional mass fractions are stored in TGLDM tables.

In addition to the conditional reaction rates and the conditional species mass fractions, the conditional chemical source term of the sensible enthalpy equation (Equation 2.11) is also tabulated. It is calculated based on the conditional reaction rates and the enthalpy of formation as

$$\langle \dot{q}_{react}|\eta \rangle = \sum_1^k \langle \dot{\omega}_k|\eta \rangle \ \Delta h_{f,k}^0, \tag{4.21}$$

where $\Delta h_{f,k}^0$ is the enthalpy of formation of species k at 298 K. Then, the mean chemical source term of the sensible enthalpy equation (Equation 2.11) can be calculated as

$$\bar{\dot{q}}_{react} = \bar{\rho} \ \int_0^1 \frac{\langle \dot{q}_{react}|\eta \rangle}{\langle \rho|\eta \rangle} \widetilde{P}(\eta, x_j, t) d\eta. \tag{4.22}$$

Figure 4.2 shows a summary of the coupling between the CFD module, CSE code and the Lagrangian spray routine in the current implementation. First, the gas phase transport equations are solved to obtain the Favre-averaged quantities. The gas properties are used through the inner loop in the Lagrangian spray module to calculate the spray source terms. The two-way coupling is evident in the mutual effects of the gas and liquid phases. In the outer loop, the mixture fraction mean and variance are used to calculate the PDF based on a presumed beta distribution. The Favre-averaged mass fraction of CO_2 and H_2O are inverted to obtain their conditional values. These values are used to locate the conditional

31

reaction rates and mass fractions from the TGLDM tables. The conditional quantities are then averaged with the PDF to obtain the unconditional quantities.
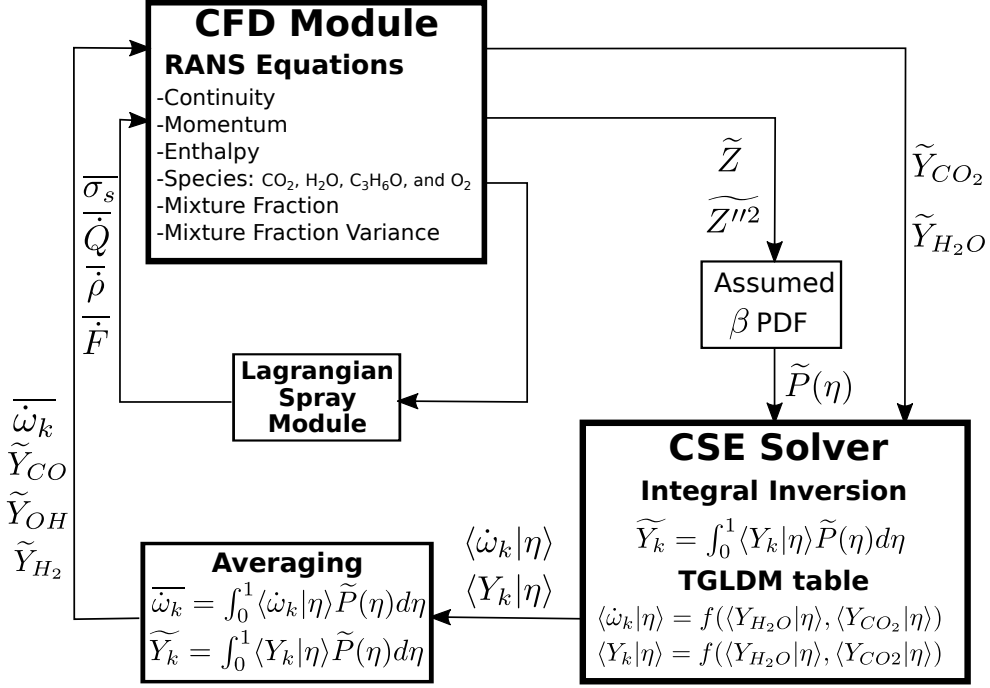
Figure 4.2: Flowchart of the coupled CSE-spray approach in two-phase flows

4.4 Radiation model

In the current study, radiation heat loss due to the main combustion product species (H_2O, CO_2, CO) is included using an optically thin radiation model. The radiative heat loss $\overline{Q}_{rad}$ is calculated as:

$$\overline{Q}_{rad} = 4\sigma(\sum_1^n p_k \ a_{p,k})(\widetilde{T}^4 - T_\infty^4), \tag{4.23}$$

where σ is the Stefan-Boltzmann constant, p_k the partial pressure of species k in atmospheres, $a_{p,k}$ the Planck absorption coefficient of species k, T the local flame temperature in K and T_∞ the background temperature [92]. Since soot concentrations are negligible in selected flames, no soot model is included and radiation due to soot is neglected. Curve

fitting is used to determine the Planck absorption coefficients as a functions of the mass fractions of H_2O, CO_2 and CO. The parameters for the curve fitting may be found in [93].

4.5 Burner Configuration

The series of piloted turbulent spray flames, experimentally studied at the University of Sydney [7, 13] is selected for investigation. The burner consists of a central jet with a diameter of 10.5 mm which issues fuel spray and a mixture of air and prevaporized fuel. The spray is generated 215 mm upstream of the jet exit by an ultrasonic nebulizer. Some of the spray evaporates before reaching the jet exit resulting in air fuel mixture at the exit section. The jet is surrounded by a pilot with an outer diameter of 25 mm to stabilize the flame . The pilot flow consists of a stoichiometric mixture of acetylene, hydrogen and air. The bulk velocity of the pilot is 4.5 m/s for non-reacting cases while it is 11.9 m/s for reacting acetone and 11.6 m/s for reacting ethanol. The pilot is surrounded by an air co-flow with a diameter of 104 mm and unburnt velocity of 4.5 m/s. Mean temperature profiles were measured by an R-Type thermocouple. The spray velocities were obtained by phase-Doppler anemometry (PDA) at different cross sections. Also, laser induced fluorescence (LIF) was used to take images of acetone and OH. Typical measurement uncertainties associated with these techniques are of the order of 10% for the temperature measurements, 6% and 15% for the velocity measurements of mean and rms, respectively [7].
In the experiments, two different parameters are varied to investigate the stability limits of the spray flames as blow-off is approached. The first parameter is the carrier mass flow rate which can be controlled by the jet bulk velocity. The other variable is fuel loading. Four carrier velocities of 24, 36, 48, and 60 m/s are set and three different mass flow rates of 23.4, 45, and 75 g/min are selected for fuel loading resulting in eight different flames for each fuel. The experimental results show that for fixed carrier velocity, the flame structures change from diffusion flame to a premixed flame structure as the droplet fuel loading is reduced and the flame approaches the global blow-off limit. In contrast, flames with fixed fuel loading show diffusion flame structure at low carrier velocities and premixed flame structures as the carrier velocity increases and the flame approaches the global blow-off. The premixed flame structures are characterized by higher centreline temperatures when compared to non-premixed flames. The current study includes one non-reacting acetone spray and several reacting acetone and ethanol flames selected such that they cover non-premixed and premixed combustion conditions.

4.6 Summary

This chapter introduces the concept of turbulent combustion modeling. Different turbulent combustion modelling strategies are discussed including the infinitely fast chemistry models such as EBU and EDM which have the advantage of low computational cost, but the model constants require adjustment for each individual case. The Laminar flamelet model has been commonly applied to many combustion problems, however, it is limited to the flamelet regime. CMC, transport PDF equation and MMC are not restricted to any combustion regime assuming appropriate closures are found for the additional terms produced for each method. However, the computational cost of CMC is higher compared to the flamlet model. The PDF methods are mathematically complex and computationally expensive. Further, the mixing term closure is not simple and the predictions quality relies on this closure. Although MMC is computationally less expensive compared to the PDF methods, further reduction in the computational cost is still required for complex geometries. CSE model for non-premixed combustion is then discussed in detail. CSE relies on the conditional averages similar to CMC, but an integral inversion is performed instead of solving CMC equations. TGLDM is used to generate the chemistry tables for acetone and ethanol combustion. The optically thin radiation model is considered to account for gaseous radiation. Finally, the experimental flame configuration is presented with different boundary conditions for every flame.

Chapter 5

Non-premixed CSE for turbulent diffusion acetone flames

The objective of the present chapter is to assess the performance of the coupled spray-combustion module using CSE. In particular, the combination of non-premixed CSE with a Lagrangian spray module is investigated. To initially examine the Lagrangian spray model, a non reacting case of evaporating acetone (Sp4) is selected. The non-reacting case consists of evaporating acetone spray issued into cold air surrounded by cold pilot and coflow. Therefore, all the factors related to chemical reaction and temperature rise are excluded. Afterwards, a non-premixed CSE version in RANS is implemented to simulate four reacting acetone flames AcF1, AcF2, AcF3, and AcF5 [2]. The CSE implementation in this chapter shares some similarities with the work of Fang et al. [94]: a non-premixed CSE formulation is implemented with a β probability density function (pdf) for the mixture fraction statistics in RANS with a similar objective of testing CSE further with more complex fuels (n-dodecane for [94] and acetone in the current study). However, a simplified CSE implementation is considered in the work of Fang et al. [94]. For the chemistry tabulation, two dimensional Flamelet Generated Manifold (FGM) is included in mixture fraction and progress variable spaces in the work of Fang et al. [94]. In contrast, three dimensional chemistry tables are created using the TGLDM approach [66, 82]. Further, the species transport equations considered are different: Fang et al. [94] solve for one progress variable only (no other species). Instead, in the present work, seven species transport equations are solved in the CFD domain. An additional source term due to spray is also included in the mean mixture fraction variance equation in the present work, whereas it is neglected by Fang et al. [94].

Flames AcF1, 2 ,3 and 5 are selected due to their diffusion flame like structure [2]. However,

the experimental data set also includes turbulent flames with more premixing that will be useful for future model developments. Further, these flames are well documented and have been simulated with different numerical approaches, this is valuable for validation. Another characteristic for flames AcF1, 2 ,3 and 5 is that they are shown to be well below the blowoff limit [2]. Thus, the proposed CSE formulation including one conditioning variable is suitable to the present conditions. The mean temperature and mixture fraction distribution for the gas phase as well as the spray velocities are compared with available experimental data [7, 13] and previous published simulation results [3, 4, 85, 86, 87, 95, 88, 96].

5.1   Computational details

Equations 2.8-2.11 and 2.22-2.23 are solved using finite volume pressure-based approach in OpenFOAM-7. At the CFD solver level, outside the chemistry tables, seven reactive species are defined, acetone (C_3H_6O), CO_2, H_2O, carbon monoxide (CO), hydroxide (OH), hydrogen (H_2), oxygen (O_2) and two inert species, nitrogen (N_2) and argon (Ar). The governing equations of C_3H_6O, O_2, CO_2 and H_2O are solved and their chemical source terms are obtained using the conditional reactions from the chemistry tables and Equation 4.14. In contrast, the mass fractions of CO, OH and H_2 are determined by retrieving their conditional mass fractions and averaging with the pdf using Equation 4.15. Time derivatives are discretized using an implicit second order backward scheme. A Gauss linear scheme is used for gradients and Gauss limited linear (bounded) for the divergence scheme. The diffusion term is approximated by the Gauss Linear limited scheme which is second order accurate in space.

The computational domain consists of a cylindrical domain with a diameter of 140 mm and a height of 420 mm. There are 45 cells in the radial direction, 48 cells in the circumferential direction, and 280 cells in the axial direction resulting in a grid with total number of cells of 604800. The mesh is clustered near the jet in the axial and radial directions to account for the sharp gradients in these regions as shown in Figure 5.1. The mesh has been refined several times and the present results are found to be grid independent. Three different mesh sizes of approximately 301,000, 604,800, and 901,000, were used in this study and no significant change in the mean temperature was detected after 604,800.

Zero-gradient boundary conditions are applied at the outlet and the side of the cylinder. The pressure defined at the outlet is 1 bar. The velocity, temperature, and species mass fractions are defined at the jet, pilot, and co-flow to match the experiments. The turbulent velocity profile at the jet inlet is obtained from the experiment. The turbulent kinetic
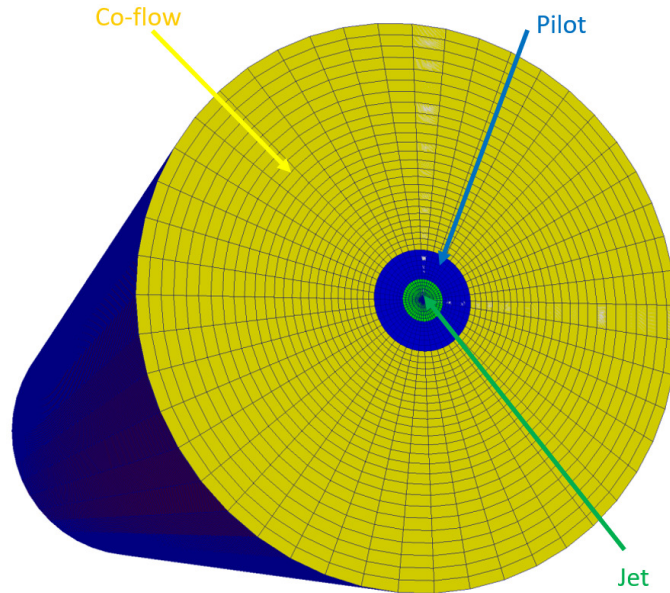
Figure 5.1: The computational domain generated for RANS computations showing different inlet surfaces.

energy at the inlet is calculated based on the turbulence intensity using the fluctuations obtained from fully developed jet profiles. The turbulence intensity is set using the reported experimental data. The boundary conditions are summarized in Table 5.1.

Table 5.1: Acetone spray parameters and boundary conditions [7]

	Sp4	AcF1	AcF2	AcF3	AcF5
Bulk velocity (m/s)	24	24	36	24	48
Carrier	Air	Air	Air	Air	Air
Carrier mass flow rate (g/min)	150	150	225	150	301
Liquid fuel injection rate (g/min)	23.4	75	75	45	75
Measured liquid fuel rate at inlet (g/min)	10.6	18	23.9	15.9	27.8
Vapour fuel rate at inlet (g/min)	12.8	57	51.2	29.1	47.2
Overall equivalence ratio	$-$	4.7	3.2	2.9	2.4
Z_{jet}	0.08	0.275	0.1898	0.1625	0.1355
Z_{Pilot}	$-$	0.0858	0.0858	0.0858	0.0858
Jet Reynolds number	18000	24400	32131	20700	39600

The parcels are inserted into the domain at z/D = 0.3 where the particle statistics are measured. In the simulations, the parcels are inserted with a constant velocity for all sizes that matches the inlet jet velocity for each flame. The Rosin-Rammler size distribution is used to define the size distribution at the jet exit. The parameters of the Rosin-Rammler distribution are fit to match the lognormal size distribution reported from the experiment [88]. The mean diameter is taken to be $26.5\mu m$ and the spread diameter n is taken to be 2.15. The maximum and minimum drop diameters are $1\mu m$ and $100\mu m$, respectively.

The standard $k - \varepsilon$ model which is known to overpredict the spreading rate in axisymmetric jets, has been modified. Different values for $C_{\varepsilon 1}$ were tested and a value of 1.55 for the non-reacting case and 1.75 for the reacting cases were found to provide best agreement with the experiment. The turbulent Schmidt number Sc_t usually takes a value around 0.7 in combustion problems based on comparison with the experiments [18]. However, two different values of 0.7, and 0.9 were tested and the value of 0.9 was found to give the best mixing field agreement when compared to the experimental results. Thus, the value of 0.9 is selected for the present flames.

When running on one core (Intel@ core i7-8700 CPU @ 3.20 GHz), the current CSE-spray simulations including 30 ensembles require approximately 21 hours for converged solutions. The CSE routine takes approximately two thirds of the total CPU time.

5.2   Non-reacting evaporating acetone Sp4

For the non reacting case, a sensitivity analysis on $C_{\varepsilon 1}$ is carried out. The sensitivity analysis consists of four simulations with $C_{\varepsilon 1}$ values of 1.44, 1.5, 1.55 and 1.6. The gas velocity profiles are not reported in the experiment [7]. Therefore, the gas velocity is compared to that of the smallest droplets group ($0 < d_p < 10\mu m$) since the Stokes number is very small and the slip velocity between the gas and the droplets is negligible [7]. Figure 5.2 shows the axial velocity at the centreline for different $C_{\varepsilon 1}$ values. It can be seen that $C_{\varepsilon 1}$=1.55 yields the best results compared to the experimental results and the axial velocity is well captured near the centreline. Figure 5.3 shows the radial profiles of the axial velocity at z/D=10, z/D=20, and z/D=30, respectively. The predicted axial velocity using $C_{\varepsilon 1} = 1.55$ is in good agreement with the experiment near the centreline, within 5% of the experimental data. However, the velocity is underpredicted away from the centreline reaching the largest discrepancy of 20% at z/D=30. These discrepancies with experimental data are attributed to the limitations of eddy viscosity turbulence model to fully capture turbulent shear layers.
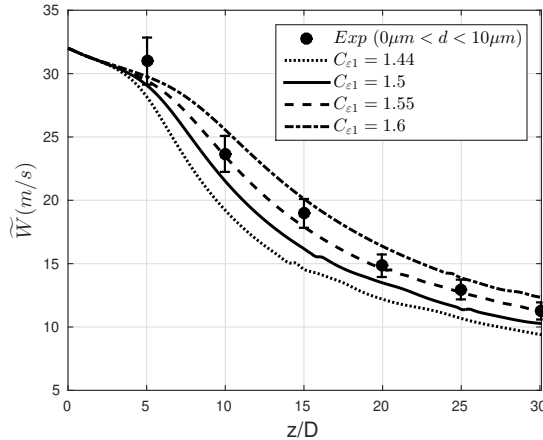
Figure 5.2: Centreline profile of mean axial velocity component for different $C_{\varepsilon 1}$ values compared with the experimental droplet velocity for $(0 < d < 10)$ [2].No experimental value is available for the gas phase, instead the smallest droplet velocity is used for comparison.

The radial profiles for the axial droplet velocities for $C_{\varepsilon 1} = 1.55$ are shown in Figure 5.4. It can be seen that the mean droplet velocity is in good agreement with the experimental data at all locations. However, the velocity is slightly underpredicted far from the centreline at all locations and overpredicted near the centreline at z/D=10. This can be explained by the fact that the droplets follow the gas velocity which shows the same trend, as can be noted from Figure 5.3. Overall, the non-reacting case shows good agreement with the experimental values.

5.3 Reacting acetone spray

5.3.1 Ensemble sensitivity analysis

As described in Section 4.2.2, the computational domain is divided into several ensembles and the inversion process is carried out for each ensemble. To make sure that the solution is independent of the number of ensembles, a sensitivity analysis on the number of ensembles is undertaken. The sensitivity study is performed on flame AcF1 and the results are applied to the other flames. The ensembles are uniformly distributed in the axial direction. The number of ensembles varies from 1 to 45 ensembles. The radial profiles of the mean temperature for different numbers of ensembles at three axial locations are shown in Figure
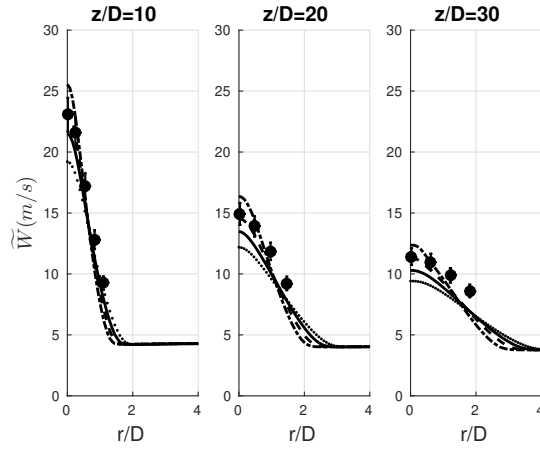
Figure 5.3: Radial profiles of mean axial velocity component at three different axial positions for different $C_{\varepsilon 1}$ values compared with the experimental droplet velocity for $(0 < d < 10)$ [2]. Same legend as in Figure 5.2.
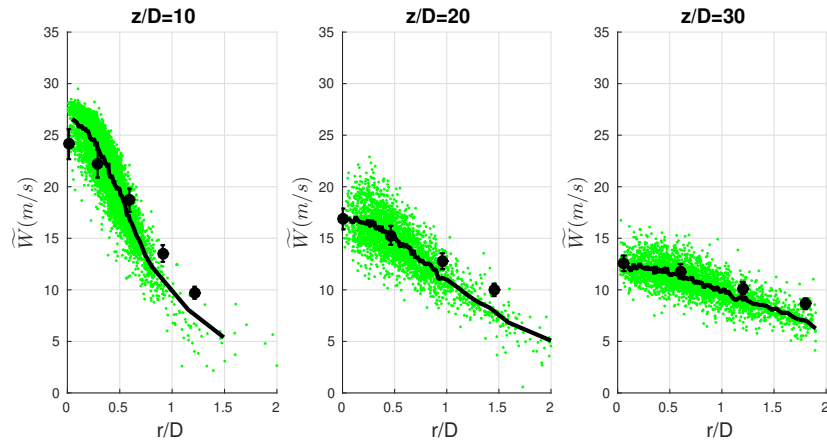
Figure 5.4: Radial mean droplet velocities for all sizes for non-reacting acetone spray Sp4 at three axial locations. The black dots represent the experimental measurements, the bars represent the uncertainty in the experiment, the green dots represent individual droplet velocity, and the black lines represent the droplets' average velocity [2]

5.5. There are clear differences in the mean temperature profiles when one ensemble is selected compared to the results with more ensembles. However, it can also be seen that even 4 ensembles yield temperatures values very close to those for a larger number of

40

ensembles. The temperature differences are negligible when 15, 30 or 45 ensembles are incorporated. This confirms the weak spatial dependence of the conditional averages. Eventually, if the number of ensembles keeps increasing, the solution would deteriorate again due to insufficient number of points in each ensemble needed for good statistical description and the inversion process imposes a requirement for the minimum number of points in each ensemble, equal to 51 (number of mixture fraction bins +1) in the current study. Detailed explanations on this aspect of getting the right balance between the number of points in each ensemble, the total number of ensembles and the connection with parallel processing are given in [77] and [97], in particular, crucial in LES.

In the remainder of the chapter, the predictions are shown for 30 ensembles, selected due to small computational run overhead. Each ensemble includes approximately 10000 CFD reacting cells, which is well above the minimum value of 51.
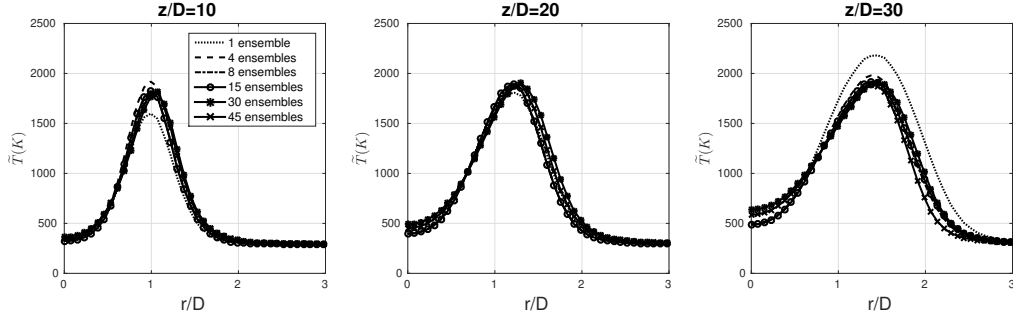
Figure 5.5: Radial profiles of mean temperature for different numbers of ensemble at three axial locations

5.3.2 Turbulent mixing field

In fully gaseous jets, the mixture fraction values decrease with increasing downstream distances due to turbulent mixing with the surrounding air. However, this is not necessarily true in spray jets as a result of evaporation. Thus, at one point downstream, the mixture fraction can exceed the jet value. The predicted radial profiles of mean mixture fraction at three axial locations for flames AcF1, AcF2, AcF3 and AcF5 are presented in Figure 5.6. For flame AcF1, the centreline value is equal to 0.3 at z/D=10 and has increased from the value of 0.275 set at the jet exit. The centreline $\tilde{Z}$ reaches a peak of 0.325 at z/D=20. This results from the high evaporation rate near the jet exit. Farther downstream, $\tilde{Z}$ decreases along the centreline due to the dominant effect of turbulent mixing over reduced evaporation of the remaining fuel droplets. At z/D=10, the peak $\tilde{Z}$ is located off the

centreline at $r/D \simeq 0.5$. This can be explained by the presence of the hot pilot next to the cold fuel inlet which increases the evaporation rate at this location. However, this is not observed farther downstream as the jet core temperature is higher and the evaporation rate becomes more even. Further, the jet width increases radially at $z/d = 20$ and 30 because of turbulent mixing. Similar trends can be observed for flames AcF2, AcF3 and AcF5. The centreline mean mixture fraction values are different due to different inlet boundary conditions and spray mass flow rates. No experimental data are provided for the turbulent mixing field, and therefore, no further comparison can be made.
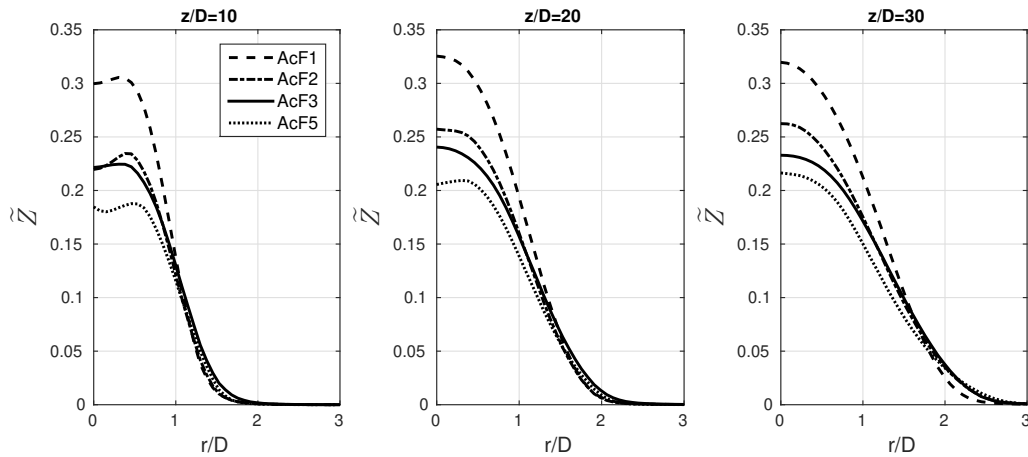
Figure 5.6: Predicted radial profiles of mean mixture fraction for the four flames, AcF1, AcF2, AcF3 and AcF5.

5.3.3   Conditional species mass fractions

The conditional mass fractions of CO_2 and H_2O at three axial locations are shown in Figure 5.7. For brevity, only the profiles for flame AcF5 are included, but similar profiles and conclusions are obtained for flames AcF1, AcF2 and AcF3. The conditional mass fractions of CO_2 and H_2O are selected as they are directly obtained by the integral inversion (Equation 4.15) and control other species reaction rates or mass fractions through the chemistry tables. Negligible changes are observed on the lean side until the stoichiometric point. However, on the rich side of stoichiometry, the conditional profiles do not decrease as steeply with increasing axial distances and reaches zero at larger values of η. This is due to a large amount of fuel being present due to evaporation in the turbulent mixing field which

has an impact on the width of the conditional profiles in η space. No experimental data are available, but some comparisons may be made with previously published simulation results. The current conditional profiles are consistent with those shown in LES-CMC [95] for flame AcF3 and LES-MMC [88] for flame AcF1. Some differences between the present profiles and those from [95, 88] are seen on the rich side of stoichoimetry, in particular in the maximum η value (η_{max}) at which the conditional mass fractions drop to zero. For example, for flame AcF1, in [88], η_{max} is approximately equal to 0.28 at z/D=30 compared to 0.32 in the current results, as shown in Figure 5.8. This difference can be explained by the lower mean centreline mixture fraction values predicted by LES-MMC. The current conditional mass fractions show good agreement with LES-MMC for $\eta < 0.22$. This further confirms the accuracy of the inversion process to obtain the conditional mass fractions. The deviation between RANS-CSE and LES-MMC for rich mixture fractions can be explained by the lower mean centreline mixture fraction values predicted by LES-MMC and the lower number of cells containing mixture fractions higher than 0.25. This results in reduced statistical information at these mixture fractions where the integral inversion shows lower accuracy. It is worth mentioning that these deviations are at mixture fractions higher than the upper flamibility limit of acetone ($z_{ufl} \approx 0.25$) and its effect is negligible on the predictions. In the work of Ukai et al. [95], the sample space is clipped to the inlet jet mean mixture fraction value.
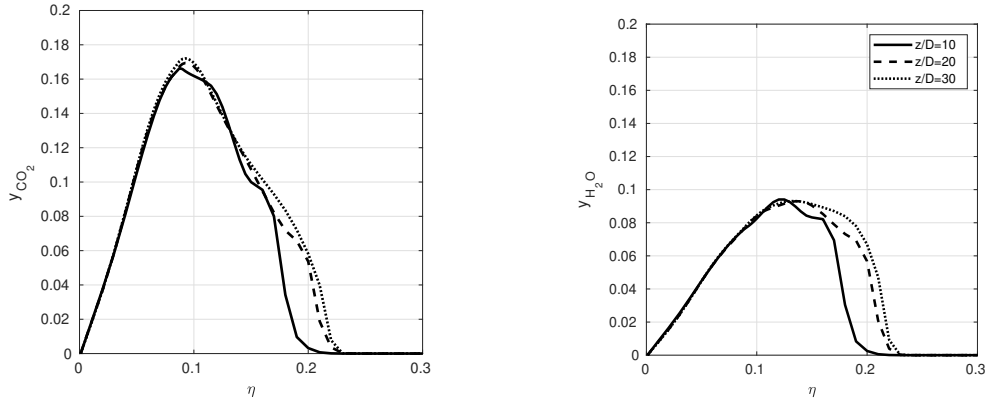
Figure 5.7: Conditional mass fraction of CO_2 and H_2O at three axial locations for flame AcF5

43
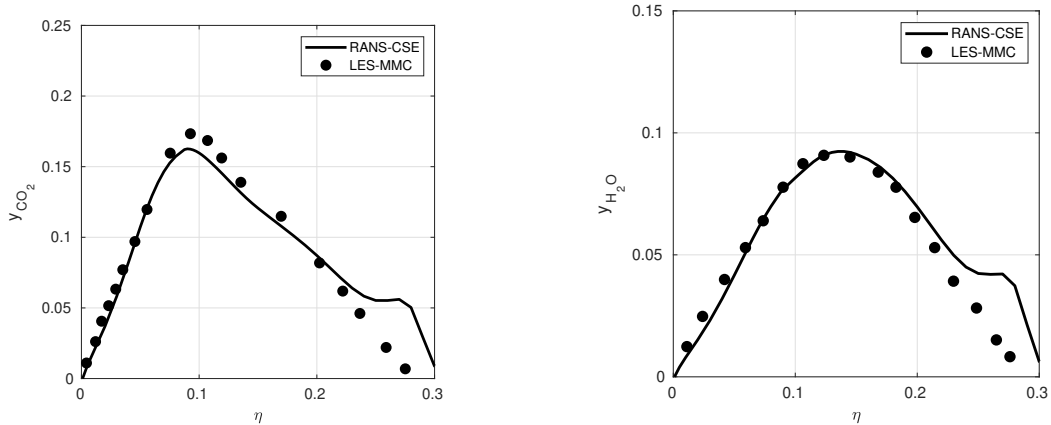
Figure 5.8: Conditional mass fractions of CO_2 and H_2O at z/D=10 for flame AcF1 compared with the LES-MMC results.

5.3.4 Favre averaged gas temperature

In this section, the radial profiles of mean temperature for the four selected flames are compared with experimental data and previously published simulation results. The radial temperature profiles of AcF1 at different axial locations are presented in Figure 5.9(a) and they show good agreement at z/D=10 and z/D=20 regarding the peak temperature. However, at z/D=10 the maximum predicted temperature is slightly shifted radially outwards compared to the experimental profile, likely due to some inaccuracies in the predicted jet spreading rate using the current RANS-k-ε formulation. This temperature peak shifting is also observed at z/D=30 and the maximum temperature discrepancy is 8%. In addition, the temperature is underpredicted near the centreline, in particular at z/D=30. Similar qualitative observations are also noted in most recent LES of flame AcF1 using a non-premixed combustion formulation [95, 3, 88, 96], in particular the larger discrepancies observed at z/D=30 as shown in Figure 5.9(a). Nevertheless, the peak location and peak temperature are more accurately predicted in LES-MMC [88] and LES-CMC [3], which is expected due better turbulent shear layer and mixing description.

Figure 5.9(b) shows the mean temperature profiles of flame AcF2. Similar conclusions are reached for flame AcF2. However, a better agreement of the centreline mean temperature and peak location with experiments is observed at z/D=30. For flame AcF1, a closer agreement with experimental data is found with previous LES-CMC [3].

The radial temperature profiles for flame AcF3 are shown in Figure 5.9(c). A better agreement between the predicted and measured values is noted near the centreline. The mean
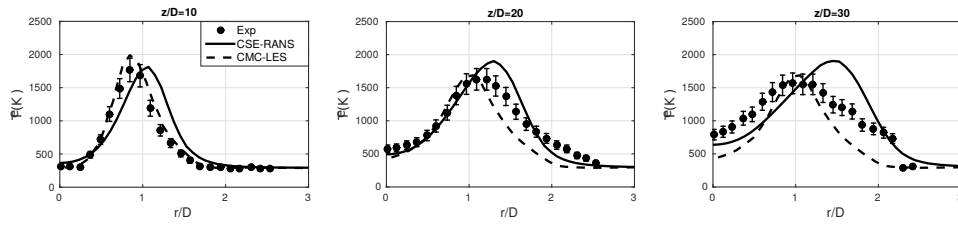
(a) AcF1
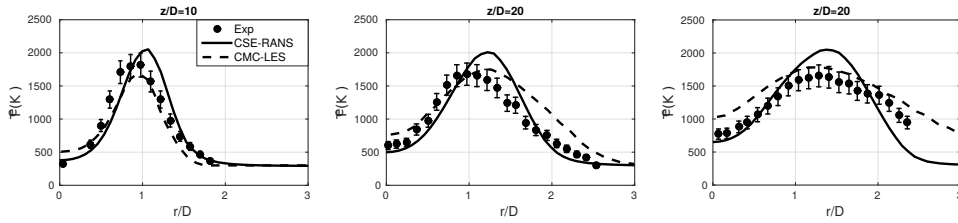
(b) AcF2
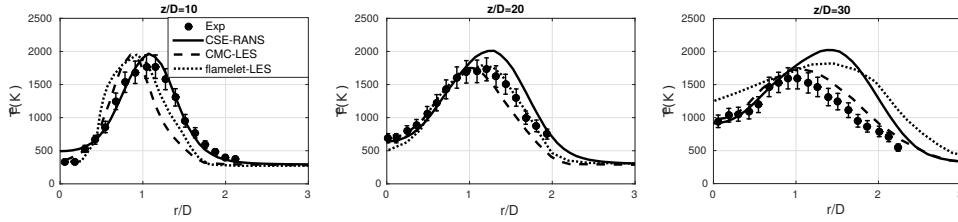
(c) AcF3
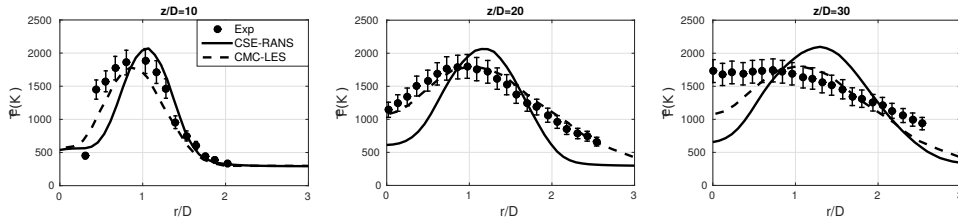
(d) AcF5

Figure 5.9: Radial mean temperature profiles for flames AcF1, AcF2, AcF3, and AcF5 at different axial locations compared with the experimental data [2]. Solid lines represent the current CSE-RANS predictions, dashed lines CMC-LES data [3] and dotted lines non-premixed flamelet-LES values [4], whenever available.

45

temperature profiles match closely the experimental profile at the first two axial locations. At z/D=30, the predicted temperature peak is located at a larger radial distance in comparison with the experimental value with a maximum temperature discrepancy of 23%. The present results are comparable with previous LES-CMC [3, 96] in terms of accuracy: in the current RANS-CSE, the centreline values are closer to the experimental data and the peak location is better predicted at z/D=10, however the predicted peak is shifted farther out radially at z/D=30. Further, the present predictions may also be compared with previous LES of the same flame using a flamelet model for turbulent combustion. Previously published LES results for flame AcF3 are available with three different flamelet model formulations, non-premixed, premixed, and partially premixed flamelet-based tabulated chemistry [4, 85]. In the non-premixed flamelet LES, the centreline mean temperature appears to be overpredicted at z/D=30 as shown in Figure 5.9(c), while in the premixed flamelet LES, they are shown to be significantly underpredicted at z/20 and z/D=30. The partially premixed flamelet LES reveals slightly better predictions when compared to the premixed flamelet. The current temperature predictions are very close to those shown by the LES with non-premixed flamelets at all locations. Similar temperature magnitudes are obtained at z/D=10 and z/D=20. However, in CSE, the centreline temperature predictions are much closer to the experiment at z/D=30. Further, the peak location shift is also visible in the LES non-premixed flamelet as in the present results. The overprediction of the peak temperature is greater in RANS-CSE than that of LES-non-premixed flamelet. Figure 5.9(d) presents the temperature profiles of flame AcF5. They show similar trends to what is observed in flame AcF1 with respect to the underpredicted temperature near the centreline and the peak shift. In LES-CMC, the centreline temperature is also underpredicted, in particular at z/D=30. However, the peak temperature is closer to the experimental results. It can be observed that the prediction accuracy deteriorates for flame AcF5 compared to flames AcF1, AcF2 and AcF3. This is believed to be due to the increased levels of premixing in flame AcF5. The overall equivalence ratio can be used to combine the fuel and carrier mass flow rates. It is calculated using the mass flow rate of carrier air and the overall liquid fuel mass flow rate assuming all the liquid fuel is in the vapor form. The overall equivalence ratio of the four flames AcF1, AcF2, AcF3, and AcF5 are 4.7, 3.2, 2.9, and 2.4, respectively. Flames with higher overall equivalence ratio are mostly non-premixed as the high fuel to carrier mass flow rate increases the number of unevaporated droplets that start to evaporate and mix farther downstream. Flames AcF1 and AcF2 show predominantly diffusion flame like structure, while flame AcF5 starts to move to a premixed nature. This can be seen in the significantly high centreline temperature of flame AcF5 when compared to flames AcF1, AcF2 and AcF3. The current CSE implementation is based only on fully non-premixed combustion and an additional conditioning variable needs to be introduced to reproduce the partially premixed flame propagation and

46

capture flame lift-off accurately [77]. This explains why the previously published RANS predictions developed for partially premixed combustion show more accurate predictions for flame AcF5 [86]. Previously published simulations of these flames also mention larger experimental temperature uncertainty due to the thermocouples which may lead to some noticeable errors in high temperature regions of two-phase flows [86, 87, 4].

In the current investigation, the evaporation effect is not included in the chemistry tabulation and therefore, the conditional chemical reaction rates are assumed to be unaffected by evaporation. The inclusion of evaporation effect on the conditional averages would tend to decrease the predicted Favre averaged temperature in the region of high evaporation rates. In the selected flames, evaporation rates are the largest close to the centreline in fuel rich regions. In comparison to the experimental data, no significant temperature overprediction is noticed except for flame AcF3 where a more visible overprediction is indicated, as can be seen in Figure 5.9. In the past LES-CMC [95], an evaporation source term is included in the CMC transport equations and temperature predictions for flame AcF1 are shown with and without the CMC spray source term. Negligible changes in the Favre averaged temperature profiles are found for the first two axial locations, $z/d = 10$ and 20. Farther downstream, at $z/d = 30$, the main evaporation effect is shown to shift the peak temperature slightly inwards towards the centreline. However, the magnitude of predicted temperature with/without CMC spray source term remains at the same level when the temperature shift is considered for the without CMC spray source term profile. These past results would indicate that the current temperature predictions could be improved, in particular at $x/d = 30$ with the inclusion of spray effect in the TGLDM tables that may correct the temperature peak locations in the selected flames. In the future, a combination of better turbulent flow/mixing field prediction through LES and the inclusion of spray effect in the chemistry tabulation is expected to have the largest impact on the Favre averaged temperature predictions.

5.3.5 Spray statistics

The mean droplet velocities compared with the experimental data are shown in Figure 5.10. The predicted droplet velocities are in good agreement with the experiment, in particular at $z/D=10$. However, the predicted droplets velocities are underpredicted at $z/D=30$ for AcF1 and AcF2 flames. The noticeable velocity underprediction in flames AcF1 and AcF2 is related to the low jet-core temperature, as shown in Figures 5.10(a) and 5.10(b), which reduces the thermal expansion near the centerline. This problem does not appear in flames AcF3 and AcF5 since they have relatively higher temperatures near the core. In addition, the number of droplets for AcF3 and AcF5 at $z/D=30$ is much smaller compared to those

of AcF1 and AcF2 as the higher temperatures at the jet centreline significantly increases the evaporation rates. Overall, the Lagrangian spray model seems to accurately capture spray statistics and the gas-liquid interactions are reasonably reproduced for the present flames.

5.4   Summary

RANS equations are solved coupled with CSE model for non-premixed flames to simulate four acetone flames with diffusion characteristics. A modified k-ε turbulence model is used to correct the overpredicted jet spreading of axisymmetric jets. The Eulerian-Lagrangian method is applied where the Lagrangian approach is employed to determine the dispersed phase characteristics. The coupling between the two phases is achieved by introducing source terms to the governing equations to account for mass, momentum, and heat transfer. The selected flames include dilute sprays only. Detailed chemistry effects are included by generating the TGLDM tables prior to the simulations. The mean temperature and droplet velocities are compared with the experimental results for reacting acetone spray flames.

The mean gas temperature profiles are well captured. However, overprediction near the peak is observed for all flames, in particular at farther downstream locations. Further, the peak temperature is also shifted radially outwards at downstream locations. The temperature is slightly underpredicted for flames AcF1 and AcF2 and significantly underpredicted for flame AcF5 near the jet-core. Previously published numerical studies [86, 87, 95, 3, 96, 4, 85, 88] also noted larger discrepancies at the third axial location. Possible sources of discrepancy are inaccurate turbulent mixing field due to RANS limitations, increased levels of premixing that cannot be captured in the present non-premixed CSE version, the neglect of spray effect on the conditional averages in the chemistry tabulation and a larger experimental uncertainty in the temperature measurements in high temperature regions. The mean droplets velocity profiles show good agreement with the experiments for the four flames. However, the velocity is underpredicted, especially near the centerline, for flames AcF1 and AcF2. This can be justified by the lower centerline temperature which causes lower thermal expansion. The velocity profiles of flames AcF3 and AcF5 are in good agreement with the experimental results since the temperature is higher at the centerline. The number of droplets in flames AcF3 and AcF5 is small at z/D=30 since the higher temperature at the centerline enhances the evaporation rates and most of the droplets evaporate before reaching this location. The present results may be improved by performing LES for better description of the turbulence and mixing fields, and including the evaporation effects in the chemistry tabulation.
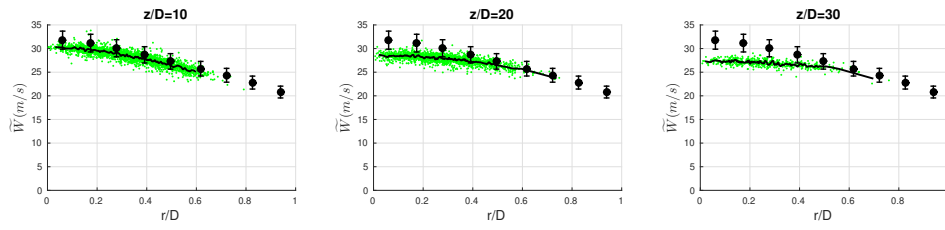
(a) AcF1
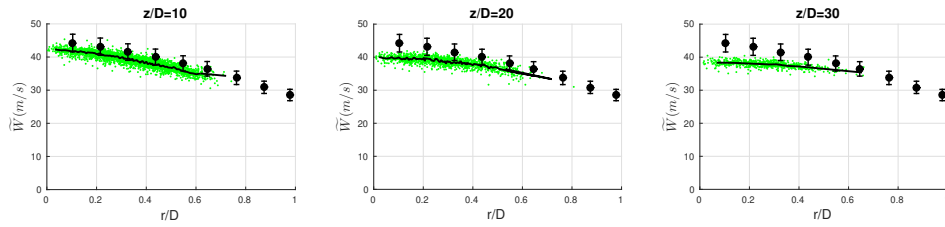
(b) AcF2
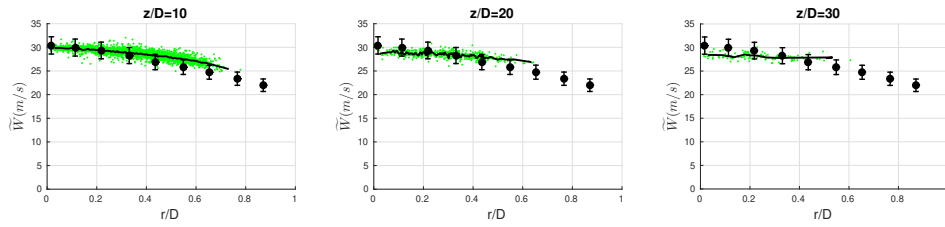
(c) AcF3
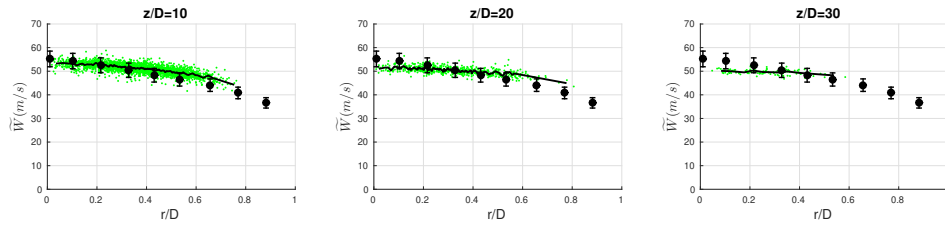
(d) AcF5

Figure 5.10: Radial mean droplet velocities for all sizes for flames AcF1, AcF2, AcF3, and AcF5 at different axial locations. The black dots represent the experimental measurements, the bars indicate the uncertainty in the experiment, green dots are for individual droplet velocity, and black lines represent the droplets average velocity [2]

49

Chapter 6

DCSE for turbulent partially premixed ethanol flames

The capability of incorporating multi mode combustion regimes with a partially-premixed combustion formulation, for example, is crucial for turbulent spray flame modeling. The aspect of turbulent partially-premixed combustion is further explored in the present study using a formulation based on CSE [63]. Doubly conditioned CSE (DCSE) has been developed by adding another conditioning variable to simulate partially premixed and lifted flames [75, 76, 77]. Recently, the CSE concept and DCSE have also been examined in an a-priori Direct Numerical Simulation (DNS) analysis for high pressure conditions [98, 97]. These past studies have shown that DCSE and double conditioning are likely to be needed for cases closer to real practical combustion applications. Doubly conditioning approaches also result in additional modeling and numerical complexities. Much more research is still required to elucidate these aspects.

In Chapter 5 , four turbulent spray acetone flames from the Sydney experimental series of spray flames [7] were investigated using singly-conditioned CSE. These four selected flames are characterized mostly by diffusion flames with different levels of premixing. Overall, the predictions of mean temperature and droplet velocity show good agreement with the experimental data. However, several discrepancies in the mean temperature profiles are observed. The radial temperature profiles were often underpredicted near the centreline and overpredicted near the flame peak temperature. Further, the peak temperature locations were overpredicted and shifted radially outward. The accuracy of temperature prediction was shown to degrade with increased levels of premixing. Three possible explanations have been proposed. First, RANS calculations imply well-known limitations in the predictions of turbulent flow and mixing fields. The logical remedy would be to switch to Large Eddy

Simulation (LES). Second, the use of one conditioning variable (mixture fraction) is insufficient to accurately predict the complex flame structure, particularly, for flames with more premixing. Third, the spray evaporation effects need to be included in the tabulated chemistry and therefore, directly in the conditional averages. As a step wise approach, it is decided to move to DCSE first to implement a partially-premixed formulation that can handle multi combustion modes before moving to LES and developing non-adiabatic chemistry tables. The objective of this chapter is to assess the capabilities of DCSE to accurately reproduce different combustion regimes from non-premixed to premixed flames for the selected turbulent ethanol spray flames. CSE calculations are performed and serve as a comparison baseline for DCSE in addition to available experimental measurements. Further, the DCSE implementation has been improved compared to previous DCSE studies [75, 76, 77]: transport equations of a non-normalized progress variable and its variance are solved and therefore, removing uncertainties in the modeling of additional unclosed terms previously found [77] and the parallel processing has also been improved for faster run times.

Flames EtF1, EtF3, and EtF4 are considered in the current study with flame EtF1 being predominantly non-premixed and flames EtF3 and EtF4 including increasing levels of premixing [7, 2]. Further information related to the flame selection is presented in Section 6.2. Previously published numerical studies are also available for some of the selected flames using different implementations of flamelet model [99, 100, 101, 102, 103], Multiple Mapping Conditioning (MMC) [62] and DNS [104]. The experimental data and previous modeling results serve as a foundation for comparison with the present CSE/DCSE results.

6.1 DCSE formulation

The methodology is described in the context of DCSE. Similar to CMC, CSE and DCSE use the conditional averages to obtain the unconditional Favre-averaged quantities in turbulent reacting flows. First order closure for the conditional chemical production rate is commonly applied resulting in fluctuations about the conditional averages being neglected. This assumption is proven to be reasonable for attached jet flames far from extinction and without ignition [51] and was successfully applied to previous CSE studies of attached non-premixed turbulent flames [12, 68]. Conditional fluctuations are even smaller when doubly instead of singly conditioning is applied. Thus, first order closure is expected to be reasonable in DCSE for a wide range of conditions, as shown in previous studies [105, 106]. In doubly conditioning approaches, two conditioning quantities are introduced: the mixture

fraction which describes the degree of mixing and the progress variable which represents the degree of reaction. The normalized progress variable is defined as $c = Y_c/Y_{c,\,eq}(Z)$, where Y_c is the progress variable and $Y_{c,\,eq}(Z)$ is the equilibrium value at a specific mixture fraction Z. The idea of DCSE is to obtain the unconditional Favre-averaged scalars by integrating the conditional averages with a joint PDF that represents the statistical distribution of the mixture fraction and the progress variable. Therefore, the mean chemical reaction rate is calculated from the following integral

$$\overline{\dot{\omega}_k}(x_j, t) = \int \int \frac{\langle \dot{\omega}_k | \eta, c^* \rangle}{\langle \rho | \eta, c^* \rangle} \widetilde{P}(\eta, c^*; x_j, t) d\eta dc^*, \tag{6.1}$$

where $\overline{\dot{\omega}_k}$ is the mean chemical source term of species k, x_j the spatial coordinate, t the simulation time, η mixture fraction sample space, c^* the normalized progress variable sample space and P the joint PDF. The terms $\langle \dot{\omega}_k | \eta, c^* \rangle$ and $\langle \rho | \eta, c^* \rangle$ represents the conditional chemical reaction rate and conditional density, respectively.

As discussed in Chapter 4, the conditional chemical reaction rates could be calculated from any selected species based on the selected fuel and chemical mechanism. In the current investigation, the conditional chemical source term $\langle \dot{\omega}_k | \eta, c^* \rangle$ is obtained from the chemistry tables knowing the conditional mass fractions of CO_2 and water H_2O

$$\langle \dot{\omega}_k | \eta, c^* \rangle \simeq \dot{\omega}(\langle Y_{CO_2} | \eta, c^* \rangle, \langle Y_{H_2O} | \eta, c^* \rangle), \tag{6.2}$$

where $\langle Y_{CO_2} | \eta, c^* \rangle$ and $\langle Y_{H_2O} | \eta.c^* \rangle$ are the conditional mass fractions of CO_2 and H_2O, respectively. In DCSE, $\langle Y_{H_2O} | \eta, c^* \rangle$ is calculated from the Favre-averaged mass fraction of H_2O by inverting the following integral

$$\widetilde{Y}_{H_2O}(x_j, t) = \int_0^1 \langle Y_{H_2O} | \eta, c^* \rangle (\eta, c^*; x_j, t) \widetilde{P}(\eta, c^*; x_j, t) d\eta dc^*, \tag{6.3}$$

where $\widetilde{Y}_{H_2O}(x_j, t)$ is the Favre-averaged mass fraction of water obtained by solving the transport equations. In contrast to CSE, DCSE requires only one inversion process for H_2O as the conditional mass fraction of CO_2 is also the progress variable sample space, taking advantage of having only one species in the progress variable representation. To calculate the joint PDF, the mean mixture fraction with its variance and the mean progress variable with its variance must be determined. For this, $\tilde{Z}$ and $\widetilde{Z''^2}$ are found by solving Equations 2.22 and 2.23. However, the transport equations for the mean normalized progress variable and variance are not solved directly due to complex and unclosed additional terms: three unclosed additional terms due to progress variable dissipation rate,

mixture fraction dissipation rate and cross-dissipation arise. These three terms are not straightforward to model and increase the modeling uncertainty [77]. Alternatively, the mean non-normalized progress variable $\widetilde{Y}_c$ and its variance $\widetilde{Y_c''^2}$ transport equations are solved [107, 108, 109] and the normalization step is carried out later before calculating the joint PDF. The normalized Favre-averaged progress variable mean and variance are calculated following [109] as

$$\widetilde{c} = \frac{\widetilde{Y}_c}{\widetilde{Y_{c,\,eq}}}, \tag{6.4}$$

$$\widetilde{c''^2} = \frac{\widetilde{Y_c''^2}}{\widetilde{Y_{c,\,eq}^2}} + \widetilde{Y}_c^2 \left(\frac{1}{\widetilde{Y_{c,\,eq}^2}} - \frac{1}{\widetilde{Y_{c,\,eq}}^2} \right), \tag{6.5}$$

where $\widetilde{Y_{c,\,eq}}$ and $\widetilde{Y_{c,\,eq}^2}$ are calculated using the mixture fraction PDF as

$$\widetilde{Y_{c,\,eq}} = \int Y_{c,\,eq}(\eta)\widetilde{P}(\eta)d\eta \tag{6.6}$$

$$\widetilde{Y_{c,\,eq}^2} = \int Y_{c,\,eq}^2(\eta)\widetilde{P}(\eta)d\eta \tag{6.7}$$

In the current study, the progress variable is taken to be the mass fraction of CO_2 such that $Y_c = Y_{CO_2}$. This definition has been used previously for methane combustion and yielded good results in RANS and LES [75, 77]. The same definition was also used in DCMC to simulate turbulent spray flames of ethanol [110] and heptane [111]. In the current solver, a transport equation is solved to obtain the Favre-averaged mass fraction $\widetilde{Y}_c = \widetilde{Y}_{CO_2}$. An additional transport equation of the progress variable variance is required, as presented in Section 6.1.2. In the current study, the c^* distribution is uniform with 20 points and shown to be sufficient. The number of c^* bins was increased to 40 and no significant changes could be seen in the predictions.

6.1.1 Presumed joint PDF

The presumed joint PDF can be written, assuming statistical independence between the mixture fraction and progress variable, as

$$P(\eta, c^*) = P(\eta)P(c^*), \tag{6.8}$$

where $P(\eta)$ and $P(c^*)$ are approximated by a β-PDF. However, the assumptions of statistical independence and presumed β PDF may not be accurate and may introduce additional numerical errors to the predictions. In the present work, without detailed experimental or DNS data, it is not possible to have a direct estimation of the impact of the assumptions on the predictions. Nevertheless, further insight on this issue may be gained from turbulent spray flames studies, which have shown that the use of β PDF is a good approximation for the mixture fraction PDF [112, 113]. More debate exists for the use of the β PDF for the progress variable, but a recent DNS investigation applied to one of the selected turbulent ethanol flames, EtF3, reports the β PDF to be a reasonable approximation for the PDF of the progress variable [114]. Several other LES studies for the Sydney ethanol turbulent flames include a comparison between predictions obtained from different presumed PDF shapes, in particular with β and top hat functions and observe negligible effect of the selected PDF shapes on the final predictions [101]. Beyond the use of presumed PDF shapes, the assumption of statistical independence between mixture fraction and progress variable is more questionable [97]. This assumption could be relaxed if a joint PDF transport equation is solved [115]. This is beyond the scope of the present study. As in all other earlier studies on the same selected flames [99, 100, 101, 102, 103], these assumptions are made for simplicity in the context of presumed PDF.

6.1.2 Progress variable

The transport equation of the progress variable $Y_c = Y_{CO_2}$ is already included in the species transport Equation 2.10. Moreover, an additional transport equation of the progress variable variance $Y_c''^2$ is required to calculate the presumed progress variable PDF $P(c^*)$. The progress variable transport equation is written as

$$\frac{\partial}{\partial t}(\bar{\rho}\widetilde{Y_c''^2}) + \frac{\partial}{\partial x_i}(\bar{\rho}\widetilde{u_i}\widetilde{Y_c''^2}) = \frac{\partial}{\partial x_i}\left(\frac{\mu_t}{Sc_t}\frac{\partial \widetilde{Y_c''^2}}{\partial x_i}\right) + 2\frac{\mu_t}{Sc_t}\frac{\partial \widetilde{Y_c}}{\partial x_i}\frac{\partial \widetilde{Y_c}}{\partial x_i} - \bar{\rho}\widetilde{\chi_c} + 2\bar{\rho}(\widetilde{Y_c\dot{\omega}_{Y_c}} - \widetilde{Y_c}\widetilde{\dot{\omega}_{Y_c}}), \quad (6.9)$$

where the last term on the RHS represents the correlation between the fluctuations of the conditioning variable and the reaction rate. It can be modelled as

$$\widetilde{Y_c\dot{\omega}_{Y_c}} = \int_0^1 \int_0^1 \langle Y_c | \eta, c^* \rangle \langle \dot{\omega}_{Y_c} | \eta, c^* \rangle \widetilde{P}(\eta, c^*) d\eta dc^*, \quad (6.10)$$

$$\widetilde{\dot{\omega}_{Y_c}} = \int_0^1 \int_0^1 \langle \dot{\omega}_{Y_c} | \eta, c^* \rangle \widetilde{P}(\eta, c^*) d\eta dc^*, \quad (6.11)$$

where $\langle Y_c|\eta, c^*\rangle$ is the conditional mass fraction of the progress variable (the sample space of CO_2)) and $\langle \dot{\omega}_{Y_c}|\eta, c^*\rangle$ the conditional reaction rates of the progress variable obtained from the chemistry library. Equation 6.9 does not include a source term due to spray evaporation because the transport equation of $\tilde{Y}_{CO_2}$ does not include a mass evaporation source term. In the current study, a non-normalized progress variable is solved for. If, instead, the transport equation of the normalized progress variable form had been considered, an additional term for spray evaporation would arise due to the inclusion of the equilibrium value that depends on mixture fraction, as given by Equation 6.4. The full derivation of this term can be found in the appendix of Reference [4].

6.1.3 Scalar dissipation rate closure

The mixture fraction mean scalar dissipation rate term is modelled using a linear relaxation model [22] as

$$\widetilde{\chi}_z = 2\frac{\varepsilon}{k}\widetilde{Z''^2}, \tag{6.12}$$

where k is the turbulent kinetic energy and ε the dissipation rate of k. However, this model is well-known to be inaccurate for the progress variable variance transport equation (Equation 6.9). Therefore, the model proposed by Kolla et al. [116] is adopted in the current study. It has shown better mean progress variable distribution compared to the linear relaxation model [72]. The mean progress variable scalar dissipation rate is given by

$$\widetilde{\chi}_c(Z) = 2\frac{1}{\beta'}\Big([2K_c^*(Z) - \tau(Z)C_4(Z)]\frac{S_L(Z)}{\delta_L(Z)} + C_3(Z)\frac{\varepsilon}{k}\Big)\widetilde{Y_c''^2}, \tag{6.13}$$

where S_L is the unstrained laminar flame speed, and δ_L the unstrained laminar flame thickness. The other parameters in Equation 6.13 are related to the nature of reactive scalar mixing. β' is a model constant taken to be 6.7, $K_c^*(Z) = 0.85\tau(Z)$ for hydrocarbon-air mixtures, and $\tau(Z) = \frac{T_b(Z)-T_u}{T_u}$ where T_b and T_u represent the burnt and unburnt gas temperature, respectively. C_3 and C_4 are functions of the Karlovitz number and can be calculated as $C_3(Z) = 1.5/(1+Ka(Z)^{-0.5})$ and $C_4(Z) = 1.1/(1+Ka(Z))^{0.4}$. The Karlovitz number is defined as $Ka(Z) = \Big((2(1+\tau(Z))^{0.7})^{-1}(u'/S_L(Z))^3(\delta_L(Z)/\Lambda)\Big)^{0.5}$ where the rms velocity fluctuation is calculated assuming isotropic turbulence as $u' = \sqrt{2k/\varepsilon}$ and the integral length scales is $\Lambda = u'^3/\varepsilon$. Equation 6.13, shows that all the model parameters are a function of the mixture fraction Z. Therefore, the laminar flame speed, laminar flame thickness, and the burnt temperature are calculated for different mixture fraction values within the flammability limits using Cantera. After obtaining these values, a polynomial

interpolation is obtained. These polynomials are then used in the CFD solver to obtain δ_L, S_L, and T_b using $\tilde{Z}$. To examine the solution obtained from Cantera [117], the laminar flame speed is compared with the experimental work of Dirrenberger et al. [6]. Figure 6.1 shows the laminar flame speed obtained from Cantera compared with the values in [6]. The obtained solution is in good agreement with the experiment. The selected polynomial, also plotted on the same graph, is well aligned with the points from Cantera. The laminar flame thickness and the burnt temperature are shown in Figure 6.2 and Figure 6.3, respectively.
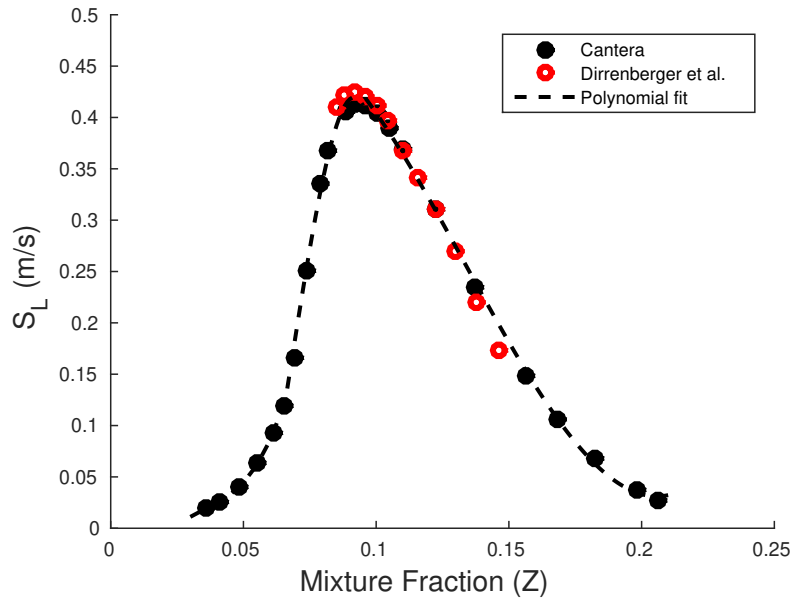
Figure 6.1: Laminar flame speed of ethanol. The solid black circles represent solution obtained from Cantera using Marinov's mechanism [5], the red circles represent the experimental data of Dirrenberger et al. [6]. The dashed line represents the interpolated polynomial

6.1.4 Summary of DCSE implementation

Figure 6.4 shows a flowchart of the implementation of DCSE. Compared to CSE, an additional transport equation of the mean progress variable variance is solved in DCSE. The mean progress variable and its variance are then normalized according to Equation 6.4 and Equation 6.5. The PDF of the normalized progress variable is calculated assuming a β
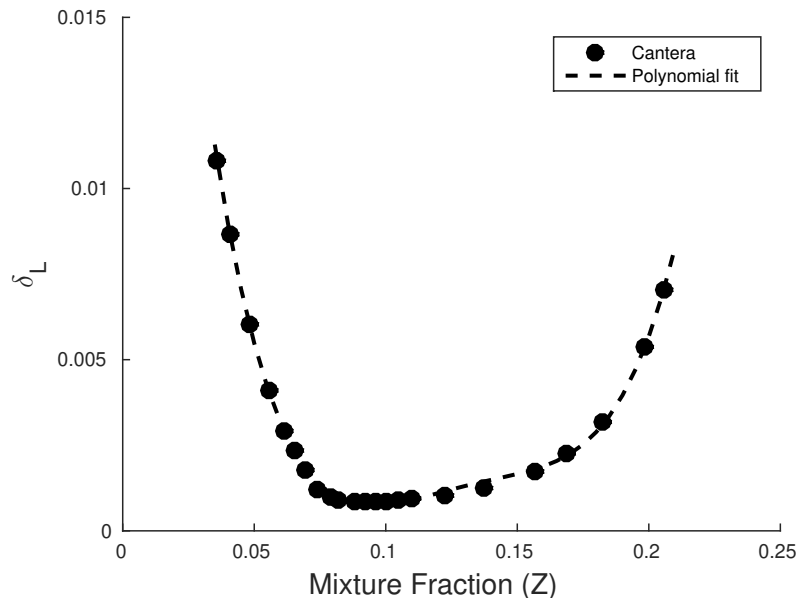
Figure 6.2: Laminar flame thickmness of ethanol.

distribution. Then, the joint PDF is calculated. In CSE, two inversion processes are performed for the Favre-averaged mass fractions of CO_2 and H_2O. In contrast, DCSE includes the inversion for the Favre-averaged mass fractions of H_2O only since the conditional mass fraction of CO_2 is the sample space.

6.2 Experimental conditions and flame selection

The burner used to study the ethanol flames is similar to that used in acetone flames as discussed in Chapter 5. The central jet has a diameter of 10.5 mm which issues droplets of fuel and a mixture of air and prevaporized fuel. The spray is generated 215 mm upstream of the jet exit by an ultrasonic nebulizer. Some of the spray evaporates before reaching the jet exit resulting in air fuel mixture with different equivalence ratios at the exit section. The degree of evaporation depends on the jet velocity and mass flow rate of the spray. The jet is surrounded by a pilot with an outer diameter of 25 mm in order to stabilize the flame. The pilot flow consists of a stoichiometric mixture of acetylene, hydrogen and air showing the same C/H ratio as in ethanol. The equivalent ethanol mixture fraction at the pilot is 0.1. The bulk velocity of the burnt pilot stream is 11.6 m/s. The pilot is
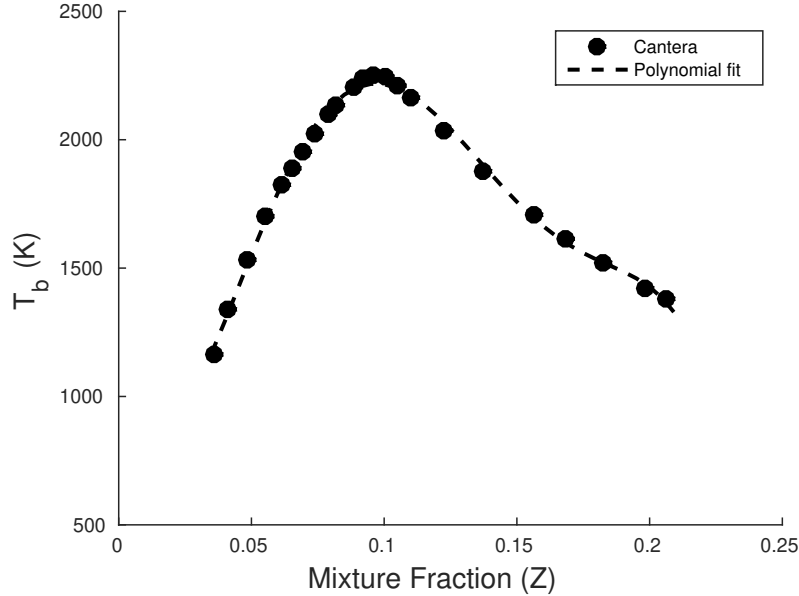
Figure 6.3: The adiabatic flame temperature of ethanol.

surrounded by an air co-flow with a diameter of 104 mm and unburnt velocity of 4.5 m/s. The experimental data set includes values for eight ethanol flames. The carrier mass flow rate and the spray mass flow rate are varied resulting in different jet conditions starting from fuel rich to fuel lean. The experimental results show that for fixed carrier velocity, the flame structure change from a diffusion flame structure to a premixed flame structure as the droplet fuel loading is reduced and the flame approaches the global blow off limit. To compare the single conditioning approach using CSE and the double conditioning approach using DCSE, three ethanol flames are selected in the current study. EtF1, EtF3, and EtF4 are selected as they have the same air mass flow rate of 150 g/min with a decreasing spray mass flow rate of 75 g/min, 45 g/min, and 23.4 g/min, respectively. The corresponding jet mixture fraction at jet exit is 0.163, 0.087, and 0.056, respectively. Flame EtF1 with a high fuel loading shows predominantly diffusion flame structures, while flame EtF3 is a transitionary flame showing characteristics similar to diffusion and premixed flames and flame EtF4 with the lowest fuel loading exhibits a premixed flame structure, also closer to the blow-off limit [7]. Therefore, the selection of these three flames gives a representative range of combustion modes from predominantly non-premixed moving towards premixed combustion regimes. The boundary conditions of the three flames are summarized in Table 6.1

CFD Module

RANS Equations
-Continuity
-Momentum
-Enthalpy
-Species: CO_2, H_2O, C_2H_5OH, O_2
-Mixture Fraction
-Mixture Fraction Variance
-Progress Variable Variance

Normalizing

$\widetilde{Y_c}, \widetilde{Y_c''^2}$

$\widetilde{Z}, \widetilde{Z''^2}$ $\widetilde{c}, \widetilde{c''^2}$

Assumed β PDF   Assumed β PDF $\widetilde{Y}_{H_2O}$

$\widetilde{P}(\eta)$ $\widetilde{P}(c^*)$

$\widetilde{P}(\eta, c^*) = \widetilde{P}(\eta)\widetilde{P}(c^*)$

$\overline{\sigma}_s$
$\dot{\overline{Q}}$
$\dot{\overline{\rho}}$
$\dot{\overline{F}}$

$\overline{\dot{\omega}_k}$
$\widetilde{Y}_{CO}$
$\widetilde{Y}_{OH}$
$\widetilde{Y}_{H_2}$

Lagrangian Spray Module

CSE Solver

Integral Inversion
$$\widetilde{Y_k} = \int\int \langle Y_k|\eta, c^*\rangle \widetilde{P}(\eta, c^*) d\eta dc^*$$

TGLDM table
$$\langle \dot{\omega}_k|\eta, c^*\rangle = f(\langle Y_{H_2O}|\eta, c^*\rangle, \langle Y_{CO_2}|\eta, c^*\rangle)$$
$$\langle Y_k|\eta, c^*\rangle = f(\langle Y_{H_2O}|\eta, c^*\rangle, \langle Y_{CO_2}|\eta, c^*\rangle)$$

Averaging
$$\overline{\dot{\omega}_k} = \int_0^1\int_0^1 \langle \dot{\omega}_k|\eta, c^*\rangle \widetilde{P}(\eta, c^*) d\eta dc^*$$
$$\widetilde{Y}_k = \int_0^1\int_0^1 \langle Y_k|\eta, c^*\rangle \widetilde{P}(\eta, c^*) d\eta dc^*$$

Figure 6.4: Flowchart of the coupled DCSE/Spray approach in two-phase flows

Table 6.1: Spray parameters and boundary conditions [7]

	EtF1	EtF3	EtF4
Bulk velocity (m/s)	24	24	24
Carrier	Air	Air	Air
Carrier mass flow rate (g/min)	150	150	150
Liquid fuel injection rate (g/min)	75	45	23.4
Measured liquid fuel rate at inlet (g/min)	45.7	30.7	14.5
Vapour fuel rate at inlet (g/min)	29.3	14.3	8.9
Overall equivalence ratio	4.7	2.9	1.5
Z_{jet}	0.163	0.087	0.056
Z_{Pilot}	0.1	0.1	0.1
Jet Reynolds number	22525	19678	17506

6.3 Computational details

The RANS CFD simulations are performed in OpenFOAM-7 using finite volume pressure-based approach. Equations 2.8-2.11, 2.22, 2.23, and 6.9 are solved. Seven reactive species are defined in the CFD simulation, ethanol (C_2H_5OH), CO_2, H_2O, carbon monoxide (CO), hydroxide (OH), hydrogen (H_2), oxygen (O_2) and two inert species, nitrogen (N_2) and argon (Ar). These selected species are the main contributors of enthalpy/temperature changes. The Favre-averaged transport equations of C_2H_5OH, O_2, CO_2 and H_2O are solved and their chemical source terms are obtained using the conditional reactions from the chemistry tables and Equation 2.10. The Favre-averaged mass fractions of CO, OH and H_2 are determined by retrieving their conditional mass fractions and averaging with the joint PDF. All selected species could be obtained by solving a transport equation. To save computational time, only the transport equations of the species needed for the inversion and TGLDM (H_2O and CO_2) and two additional species (C_2H_5OH and O_2) for accurate boundary conditions using available experimental data are included. Previous calculations showed no impact on the predictions when a reduced number of species transport equation was used.

Time derivatives are discretised using an implicit second-order backward scheme. A Gauss linear scheme is used for gradients and Gauss limited linear (bounded) scheme for the divergence scheme. The diffusion term is approximated by the Gauss Linear limited scheme, which is second-order accurate in space.

The same computational domain used in Chapter 5 is also used in the current investigation since it is the same burner configuration with the same bulk jet velocity. The computational domain consists of a cylindrical domain with a diameter of 140 mm and a height of 420 mm with 45 cells in the radial direction, 48 cells in the circumferential direction, and 280 cells in the axial direction. The total number of cells is 604800 which is sufficient to obtain a grid independent solution. The mesh is refined near the jet exit in the axial and radial directions to account for the sharp gradients in the shear layer. Zero-gradient boundary conditions are applied at the outlet and the side of the cylinder. The pressure at the outlet section is set to 1 bar. The velocity, temperature, and species mass fractions are defined at the jet, pilot, and co-flow according to the experimental values. The turbulent velocity profile at the jet inlet is obtained from the experiment. The turbulent kinetic energy at the inlet is calculated from the turbulence intensity using the fluctuations obtained from fully developed jet profiles where the turbulence intensity is determined from the experiments.

The liquid spray parcels are injected into the domain at $z/D = 0.3$ where the particle statistics are measured. The Rosin-Rammler size distribution is used to define the size

distribution of the droplets at the jet exit. The parameters of the Rosin-Rammler distribution are fit to match the lognormal size distribution reported in the experiment following [88]. All the parcels introduced into the computational domain initially have the same total volume in which the number of the droplets in each parcel depends on the droplet size. Parcels of small droplet sizes have more droplets to ensure similar volumes for all parcels. The parcel size is calculated from the imposed size distribution at the injection location. For example, we may find 1 droplet per parcel for parcels of size of 45 μm and 90 droplets per parcel for parcels of size of 10 μm. The standard $k - \varepsilon$ model with standard coefficients is used in the current study.

Forty ensembles are used in the current simulations for CSE and DCSE. Each ensemble is assigned to a separate processor resulting in parallel processing using 40 processors (Intel Skylake 2.4 GHz). When using 20 c^* bins, DCSE requires approximately 18 CPU hours to obtain converged solutions. In comparison, CSE requires only 1.5 CPU hours. Thus, CSE is almost twelve times faster than DCSE using the same computational domain and number of ensembles. This can be mostly explained by the size of the matrix that needs to be inverted. In DCSE, with 20 c^* bins, this produces an inversion matrix 20 times larger than that of CSE and retrieves 20 times more points from the chemistry tables.

6.4   DCSE ensemble selection

In CSE and DCSE, the computational domain is divided into several ensembles and the inversion process is performed for each ensemble. To ensure a reliable solution, the predictions should be independent on the selected number of ensembles. In the previous CSE study for turbulent acetone flames reported in Chapter 5, 30 ensembles are sufficient to provide ensemble independent solution. The same applies for the current ethanol flames. However, the use of more ensembles can be computationally more efficient in parallel processing. Each ensemble can be assigned to a separate processor to save more time. This is particularly crucial in DCSE as the inversion process is carried out for M points where (M = Number of η bins × Number of c^* bins) instead of only (M = Number of η bins) in CSE. Therefore, 40 equally spaced ensembles distributed in the axial direction are selected in the current study for CSE and DCSE simulations. It is worth mentioning that the number of reacting cells in each ensemble should be greater than M. In the current study, 50 bins are used for the mixture fraction and 20 bins for the progress variable. The minimum number of reacting cells is around 7000 which is far greater than (M = 1000) in the case of DCSE.

6.5 Results

### 6.5.1 Favre-averaged gas phase temperature

The radial profiles of the gas phase temperature are shown in Figure 6.5 at three axial locations for the different flames.

For flame EtF1, the CSE temperatures are in a reasonable agreement with the experimental data. In comparison with the experimental values, CSE underpredicts the temperatures near the centreline, in particular at z/D=10 and 20, with improvements at z/D = 30. It can also be seen that CSE tends to overpredict the peak temperature at all locations, by 18% at z/D=10 and 15% at z/D=20, with a maximum discrepancy of 25% at z/D=30. Further, the peak location is shifted radially outwards similar to what is observed in the previous CSE calculations of turbulent spray acetone flames conducted in Chapter 5. Near the centreline, the DCSE predicted temperatures are close to the CSE results and also share the same underprediction. The same behaviour has been noticed in CSE-RANS for acetone flames which was attributed to the lack of the RANS capability of accurately analyzing the mixing region. This temperature underprediction near the centreline is also noted in the MMC-LES for the same flame [62]. A different trend is seen in the flamelet LES work of De and Kim [100]. Their results show a significant temperature overprediction at z/D=10 and slight overprediction at z/D=20 and z/D=30, irrespective of the constant value used for the linear relaxation model of the subgrid scale (sgs) scalar dissipation rate in the sgs mixture fraction variance transport equation. De and Kim [100] explained that it is "partly attributed to the three stream nature of the current spray flame configuration". The sgs fluctuations and terms are calculated differently in the two LES studies [100] and [62] and this is probably the source of the differences seen for this flame. In contrast to CSE, DCSE shows better predictions regarding the peak temperature value at all locations in comparison with the experimental values. DCSE slightly underpredicts the peak temperatures by 7% and 9% for z/D=10 and z/D=20, respectively. At z/D=30, the DCSE profile closely follow the experimental values within the experimental uncertainty. For this flame, the accuracy of CSE and DCSE predictions may be at the same level of those for the first two axial locations. However, there is a visible improvement in the temperature profiles from DCSE at z/D = 30.

The radial temperature profiles of flame EtF3 are shown in Figure 6.5(b). As seen in flame EtF1, CSE and DCSE produce temperatures that are also underpredicted near the centreline at z/D=10 and z/D=20 with larger discrepancies at z/D=10. At this first axial location, CSE captures the peak temperature well, while DCSE reveals a slight underprediction by 13%. Similar temperature underpredictions are also noticed for the same
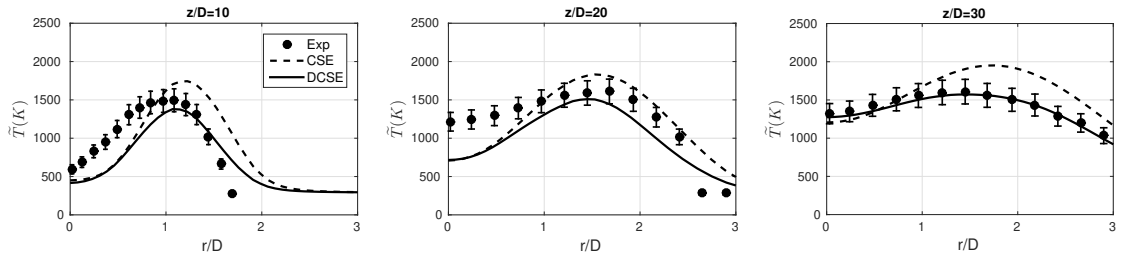
(a) EtF1
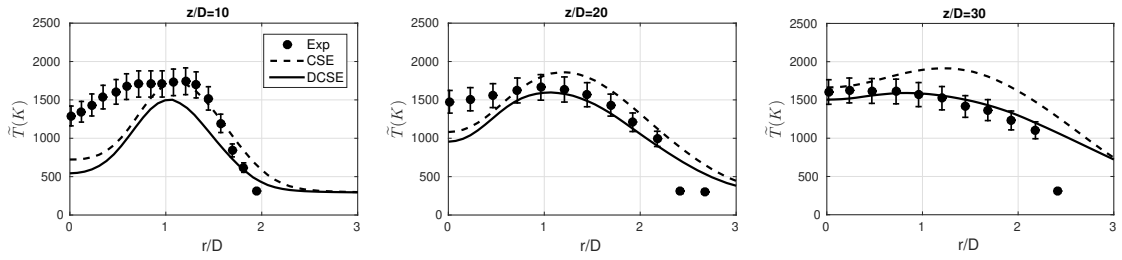
(b) EtF3
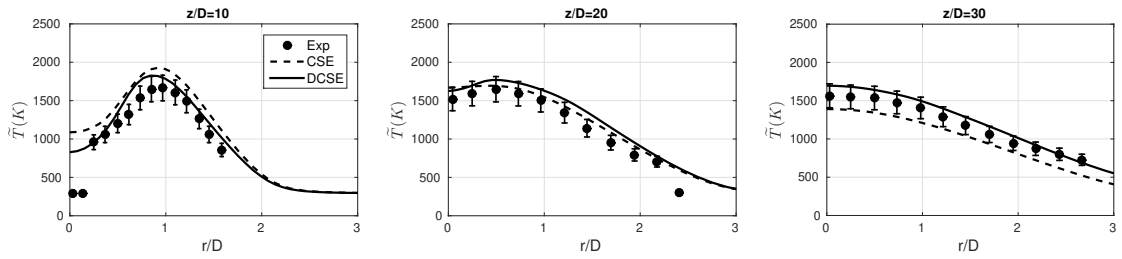
(c) EtF4

Figure 6.5: Radial mean temperature profiles of flames EtF1, EtF3, and EtF4 at different axial locations compared with the experimental data with the vertical bar at each experimental point indicating the experimental uncertainty [2] . Dashed lines represent current CSE-RANS implementation and solid lines current DCSE-RANS.

flame in DNS [104] (at z/D = 10 only) and FGM-LES [99] (at z/D=10 and 20). However, the temperature is consistently overpredicted in the LES results of premixed FGM [101]. These two LES studies include two different sgs models, a dynamic Smagorinsky model [99] and sigma model [101]. Thus, this seems to indicate the significance of modeling the sgs contribution accurately. Farther downstream, at z/D=20, and z/D=30, the DCSE temperature predictions significantly improve and display a closer agreement with the experimental profiles, compared to CSE, in particular at z/D=30. For comparison, the maximum discrepancy associated with CSE at z/D=30 is approximately 25%, while the DCSE predicted temperatures are within 7% of the experimental data. Further, at z/D=30, the peak location is overpredicted by CSE, whereas it is much better reproduced in DCSE.

Figure 6.5(c) shows the results for flame EtF4. Both CSE and DCSE predictions are in good agreement with the experimental values. Again, CSE tends to slightly overpredict the temperature at z/D=10 with a maximum discrepancy of 16%. DCSE reveals slight improvements at z/D=10 with a discrepancy in the order of 10%. It is also noticed that DCSE better predicts the centreline temperature at this location. At z/D=20, both CSE and DCSE display very good agreement with the experiment, and the peak magnitude and locations are well captured. At z/D=30, CSE underpredicts the temperature by 11%, while DCSE slightly overpredicts the temperature with a maximum discrepancy of 8%. Thus, at the measurements locations, CSE and DCSE produce similar temperature profiles at most locations. Further discussion on the CSE/DCSE similarities and differences is presented in Section 6.5.2. The present DCSE results compare favourably with those obtained in LES-FGM [100] and MMC-LES [62] for the same flame. The results in LES-FGM [100] reveal a good agreement with the experimental data at z/D=10, while the temperatures are overpredicted at z/D=20 and z/D=30. In MMC-LES [62], temperature overpredictions are observed at all locations, consistent with the current CSE results when a non-premixed formulation is applied only.

From the current results, this region of low temperature predictions may be due to inaccuracies in the turbulent velocity and mixing fields, as a result of the RANS k-ε model, which is well-known to overpredict the spreading rate in turbulent jets. However, the fact that similar observations are noted in previously published studies using LES [62, 99, 101] and DNS [104], may also point towards a different explanation. Chrigui et al. [99] and Pillai and Kurose [104] mention that this could be due to larger experimental errors near the centreline due to cooling effects arising from droplet collisions with the thermocouples, more likely to occur close to nozzle with larger amounts of droplets. In addition, the LES studies of [100] and [101] do not show any temperature underprediction close to nozzle in the core jet region in which different sgs models are used. It may be concluded that there may be several combined sources of errors, some from the experiments and others from the

modeling too due to different turbulence modeling approaches, in addition to the coupled effect of the assumption of statistical independence used in the joint PDF and neglect of evaporation effect on the conditional averages.
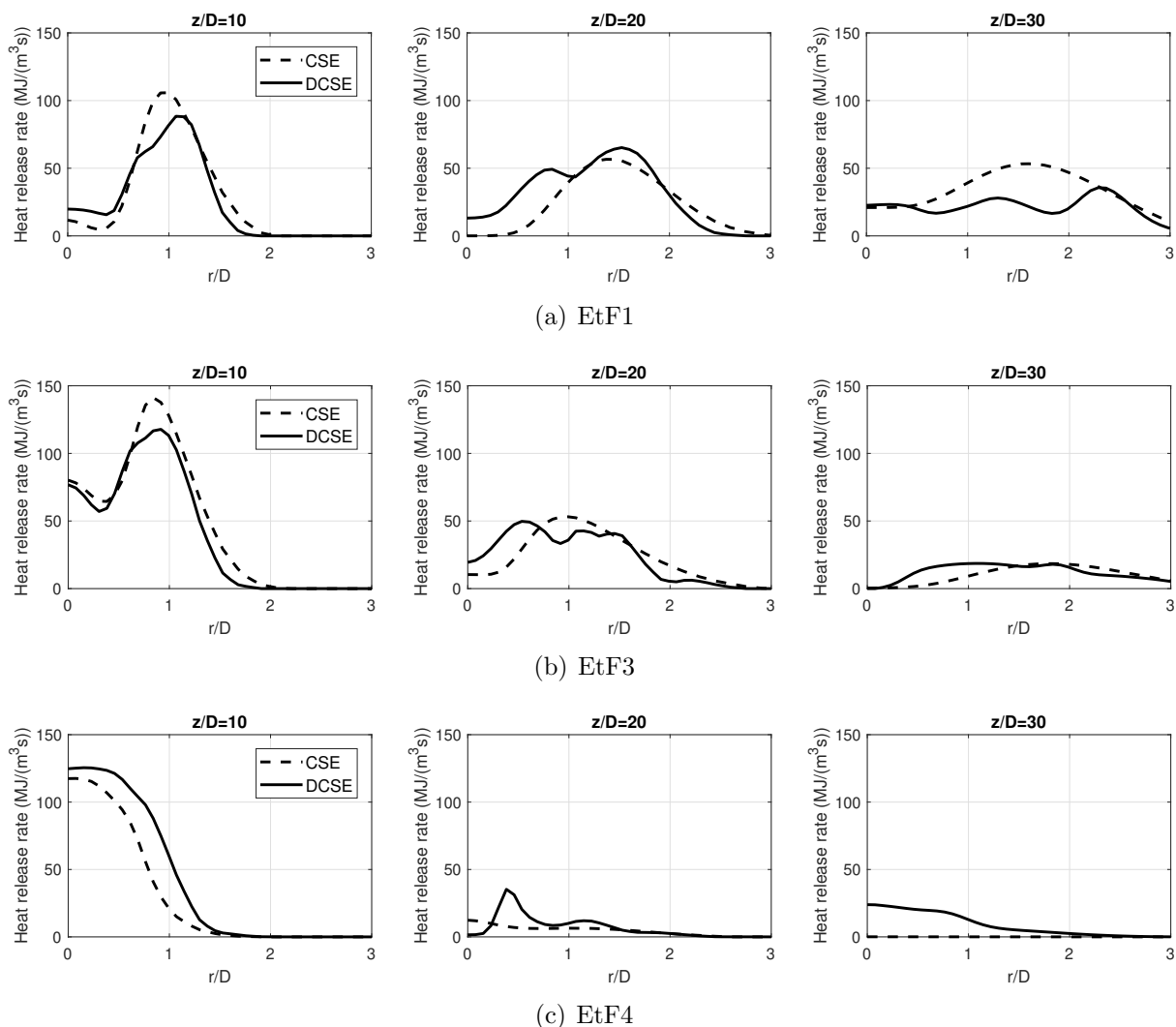

(a) EtF1

(b) EtF3

(c) EtF4

Figure 6.6: Radial profiles of mean heat release rate in MJ/(m^{3}s) for flames EtF1, EtF3, and EtF4 at different axial locations. Dashed lines represent current CSE-RANS and solid lines current DCSE-RANS.

6.5.2 Mean heat release rate

In Section 6.5.1, DCSE is shown to bring some improvements to the mean temperature predictions over CSE, but these remain smaller than initially expected. Further, the DCSE benefits seem to be most visible for flames EtF1 and EtF3 that tend to behave more like non-premixed flames, while EtF4 is supposed to be close to a partially premixed turbulent flame. These observations deserve further investigation.

In this section, the mean heat release rate (HRR) is examined for further information on the flame structure that is captured by CSE and DCSE. The mean HRR is selected for qualitative comparisons with the experimental observations and previously published numerical results. The source term of the sensible enthalpy equation represents the HRR which is the source of temperature change due to chemical reactions. This term is calculated using Equation 4.22 by averaging the conditional enthalpy source term with the joint PDF. In the current implementation, the conditional enthalpy source term is calculated based on the reaction rates of all the species in the detailed chemistry mechanism following Equation 4.21, and then tabulated in the chemistry tables. The radial profiles of the mean HRR are shown in Figure 6.6. HRR profiles show higher magnitudes at upstream locations near z/D=10 and decrease farther downstream in all flames. For flame EtF1, the CSE mean HRR profile displays a single peak at a location where $\widetilde{Z}$ is equal to 0.16, 0.15 and 0.14 for z/D = 10, 20, and 30, respectively. Thus, the highest HRR is on the fuel rich side of the stoichiometric mixture fraction. In contrast, the mean HRR in DCSE exhibits a double peak profile at some locations, in particular at z/D = 20. The double peak feature implies that EtF1 is not a traditional gaseous turbulent non-premixed flame where a single peak around the mean stoichiometric mixture fraction would be expected. At z/D = 20, the first peak is on the fuel rich side and the second peak, larger in magnitude, is on the fuel rich side, much closer to stoichiometry. Although the temperature predictions are relatively close for both models, CSE and DCSE do not reveal the same flame and the double conditioning process plays an important role. In the experiments [2], only instantaneous measurements of HRR are available at several axial positions up to z/D=25. However, these instantaneous contours may provide some qualitative information. At z/D=25, the instantaneous heat release drops sharply compared to those at the upstream locations. This observation corroborates the DCSE mean HRR profiles that have dropped significantly at z/D = 30 in comparison to the DCSE mean HRR at z/D = 20. Further information may be gained with the recent MMC-LES work [62]. EtF1 also shows a more complex flame structure than a pure gaseous turbulent non-premixed flame. Regions of non-premixed, premixed, and mixing of pre-evaporated fuels are shown to coexist in the three flames that they selected, EtF1, EtF4 and EtF7 [62]. In particular, high conditional temperature fluctuations in the fuel rich regions are evidenced in their

numerical results. This is in line with what is seen in DCSE: the formation of double peak in the HRR representing different reaction zones due to partial premixing at z/D = 20 and 30 and lower HRR values at z/D= 10 due to higher conditional fluctuations that may be captured by the double conditioning method.

Flame EtF3 shows a similar HRR distribution to EtF1 where the double peak is also observed at z/D= 10 and 20. For both CSE and DCSE, EtF3 shows higher HRR values at z/D=10 and slightly lower values at z/D = 20 and 30 in comparison to what is noticed in EtF1. This agrees with the experimental observations showing lower instantaneous HRR at z/D = 20 in comparison to the intensity in EtF1. This is also consistent with the reported flame lengths in the experiments [7, 2] where the lengths are around 66D, 50D, and 48D for EtF1, EtF3, and EtF4, respectively. Flame EtF1 is longer since it has a richer composition and the reactions persist for farther downstream distances.

Flame EtF4, which lies mainly close to the stoichiometric regime, is the shortest among the studied flames. It can be seen that the HRR drastically drops in locations after z/D=10 in CSE where most of the burning occurs before z/D=10 and no significant reactions occur downstream. This is reflected in the CSE predicted temperatures being larger than the experimental values at z/D=10 and then, the continuous temperature drop until the CSE temperatures become lower than the experimental data at z/D=30. In contrast, DCSE shows fair amounts of HRR at z/D=20 and z/D=30 where the experimental images display some heat release up to z/D=25. Furthermore, the results of MMC-LES [62] report that flame EtF4 experiences lower conditional fluctuations at z/D=20 and z/D=30 when compared to EtF1 which explains the good performance of CSE at these locations. Although the temperature profiles predicted by CSE and DCSE are close at the measurement axial locations, the HRR profiles are clearly different. In addition, the HRR is higher at upstream locations, z/D<10, and the mean HRR differences between the two models are the largest at axial locations upstream of z/D=10 where no experimental data are available for comparison. Also, CSE systematically predicts higher reaction rates at upstream locations compared to DCSE where the fuel is consumed much faster in CSE. This can explain the faster temperature decay shown in CSE. For example, the predicted peak temperature at z/D=5 is approximately 1800K and 1600K for CSE and DCSE, respectively, with 12.5% difference. However, at z/D=10, the difference has dropped to 5.5% which shows that the differences in temperatures predicted by CSE and DCSE decrease farther downstream, as shown in Figure 6.5. This further supports that the effect of double conditioning is mostly visible at axial locations upstream of z/D=10 where CSE systematically tends to predict higher reaction rates in comparison to DCSE.

6.5.3 Mean evaporation rate

The mean evaporation rate profiles are also examined. The purpose of this section is to identify the regions of high evaporation rate in both CSE and DCSE calculations and give a more detailed picture of the physical processes captured in the current simulations. For brevity, only the axial profiles of the mean evaporation rate for the three flames are shown in Figure 6.7.

(a) EtF1	(b) EtF3	(c) EtF4
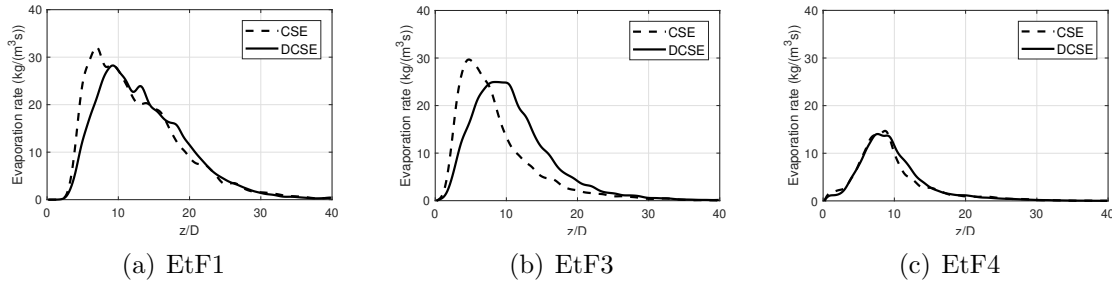
Figure 6.7: Mean profiles of evaporation source term at the centreline for flames EtF1, EtF3, and EtF4. Dashed lines represent current CSE-RANS implementation and solid lines current DCSE-RANS.

Flame EtF1 displays the highest evaporation amongst the three flames of interest since it has the highest spray mass flow rate at the nozzle exit, as shown in Table 6.1. The presented profiles are consistent with what is shown for EtF1 and EtF4 in Reference [62]. In CSE, higher evaporation rates are displayed close to the jet exit for flames EtF1 and EtF3, in agreement with the larger temperatures obtained by CSE in comparison to the DCSE results, as shown in Figure 6.5(a). For EtF3, larger differences in the centreline mean evaporation rates between CSE and DCSE are seen corresponding to larger temperature differences as well for this flame, as noted from Figure 6.5(b). The CSE results show higher evaporation magnitudes up to $z/D=8$ and then the CSE mean evaporation rates drop. This is explained by the volumes of the spray that have evaporated early upstream and the evaporation rates from the remaining droplets significantly reduced. For EtF4, the centreline values of mean evaporation rate are much smaller than those observed in EtF1 and EtF3 due to lower spray mass flow rate. Both CSE and DCSE profiles are similar, which is consistent with similar temperature profiles in Figure 6.5. From the radial profiles (not shown here for brevity), in flames EtF1 and EtF3, the peak evaporation rates are shifted from the centreline at $z/D=10$. This can be explained by the hot pilot gases that exist near these locations which enhance the evaporation process. Farther downstream, the peak is located at the centreline where the jet core starts to gain higher temperature and

the evaporation is not concentrated in the pilot passage. For EtF4, the peak is located at the centreline at z/D=10 since more evaporation occurs upstream of z/D=10 where high centreline temperatures exist.

In the light of the mean temperature predictions, as presented in Section 6.5.1 and the mean evaporation rates, as shown in Figure 6.7, the negligence of evaporation effect on the conditional averages through the TGLDM table and its possible impact on the predictions are further discussed. The spray effect is expected to be visible in high evaporation regions, like for the first 20 diameters for flames EtF1 and EtF3 and 10 diameters for flame EtF4, and close to the centreline. At these locations, there is no clear indication of significant temperature overprediction due to the neglect of spray effect on the conditional averages in the mean temperature profiles (Figure 6.5) in the regions of highest evaporation rate (Figure 6.7). Currently, no direct comparison can be made between the results obtained from adiabatic chemistry tables and those from non-adiabatic tabulated chemistry. The inclusion of the spray effect requires an additional dimension, for example the enthalpy deficit, in the TGLDM tables [89]. In a previously published CMC study [118], a comparison is performed between temperature predictions obtained with and without spray source term in the CMC transport equation for the conditional averages for the turbulent acetone spray flame AcF3. Compared to EtF3, AcF3 experiences higher evaporation rate with the liquid spray mass flow rate at the inlet section being equal to 15.9 and 30.7 g/min for AcF3 and EtF3, respectively. It is interesting to see only a small evaporation effect on the mean temperatures, negligible at z/D = 10 and 20 and only visible at z/d = 30 with a shift in the temperature peak. No additional published data could be found for this set of experimental data and caution needs to be taken with any extrapolation of results for different turbulent combustion models and different flames with different evaporation rates. This aspect needs to be examined in detail in the future.

6.5.4   Mean mixture fraction and progress variable distribution

No experimental data are available for $\widetilde{Z}$ or mean species concentrations. However, a qualitative analysis may be undertaken. The radial profiles of the $\widetilde{Z}$ and mean progress variable are shown in Figure 6.8. Flame EtF1 features the highest $\widetilde{Z}$ values among the three flames and reaches a peak of around 0.3 at z/D=20. Thus, the jet centreline lies in the fuel rich zone. The same behaviour is observed for flame EtF3 with a maximum mean mixture fraction of 0.24 at z/D=20 located on the centreline. The similarities in the $\widetilde{Z}$ profiles for flames EtF1 and EtF3 are also consistent with the simlarities seen in the mean HRR profiles and flame structure, as presented in Section 6.5.2. For flame EtF4, the jet inlet mixture fraction is on the fuel lean side with a mean mixture fraction of 0.056. The
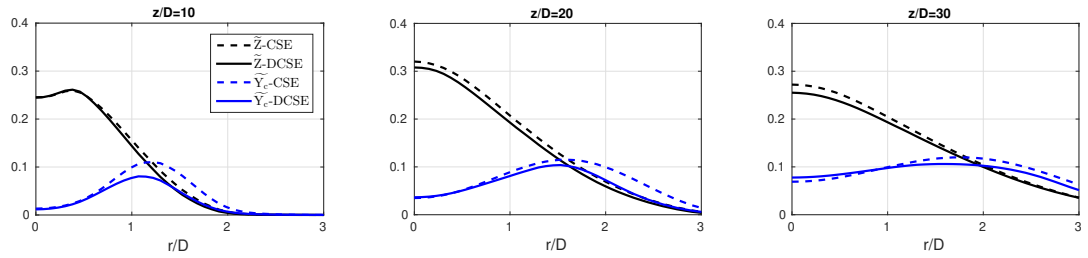
(a) EtF1
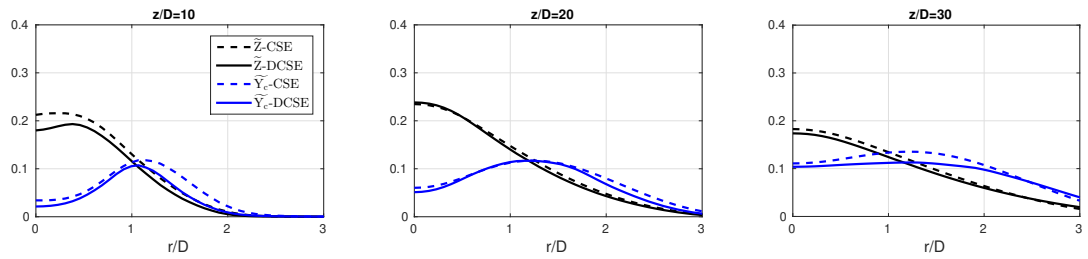
(b) EtF3
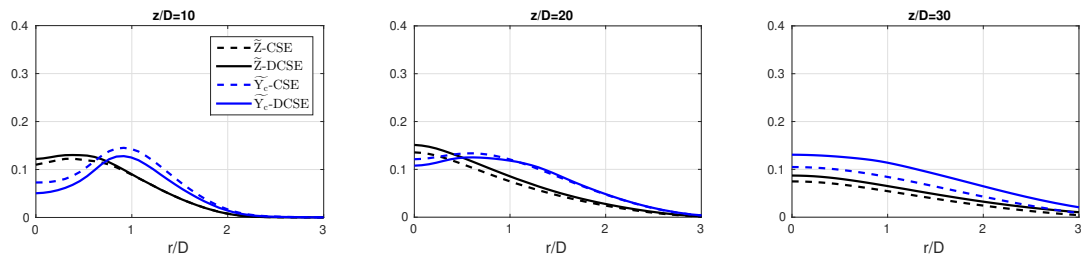
(c) EtF4

Figure 6.8: Radial profiles of mean mixture fraction and progress variable for flames EtF1, EtF3, and EtF4 at different axial locations. Dashed lines represent current CSE-RANS implementation and solid lines current DCSE-RANS. Black represents mean mixture fraction $\widetilde{Z}$. Blue represents mean progress variable $\widetilde{Y_c}$.

mean mixture fraction increases along the centreline and reaches a maximum value of 0.15 at z/D=20. Unlike flame EtF1 and EtF3, flame EtF4 primarily lies in the stoichiometric region with $\widetilde{Z}$ values around 0.1. Regarding the comparison between CSE and DCSE, the results show that CSE mostly tends to yield higher $\widetilde{Z}$ values due to the higher evaporation rates, as discussed in Section 6.5.3. It is also noted that the mean mixture fraction peak is slightly shifted from the centreline at z/D=10 for the three flames. This can be explained as the spray evaporation is maximized at these locations as a result of the existence of the hot pilot. As for the mean progress variable profiles, CSE usually predicts higher values at the different locations. This is consistent with the overpredicted temperatures resulting from the CSE simulations, as displayed in Figure 6.5. This observation is also aligned with the conclusion of previously published work that singly conditioning tends to overpredict the magnitude of product reaction rates outside the non-premixed flame regime [105].

6.5.5 Spray statistics

Spray mean velocity

The experimental data [7, 2] contains measurements of the mean droplet velocity conditioned on droplet size and unconditioned corresponding to the mean of all sizes. Five droplet size bins of $(0\mu m < d < 10\mu m)$, $(10\mu m < d < 20\mu m)$, $(20\mu m < d < 30\mu m)$, $(30\mu m < d < 40\mu m)$, and $(40\mu m < d < 50\mu m)$ are available. In the current study, the unconditioned droplet velocity is compared first. For brevity, the bin sizes of $(0\mu m < d < 10\mu m)$, $(20\mu m < d < 30\mu m)$, and $(40\mu m < d < 50\mu m)$ are selected for comparison to represent the small, medium, and large droplets, respectively. Figure 6.9 presents the mean droplet velocities for all sizes of the three flames at different axial locations. Figure 6.9(a) shows the mean droplet velocity of flame EtF1. It can be seen that the profiles are accurately captured by both CSE and DCSE. CSE shows slightly higher velocity compared to DCSE at z/D=20 and z/D=30, which corresponds to the overpredicted mean temperature at the same locations as seen in Figure 6.5(a). Both CSE and DCSE underpredict the mean velocity at the third location. This may be explained by the higher spreading rate associated with the k-ε model for round jets.

For flame EtF3, the same conclusion can be obtained at all locations with the mean velocity profiles slightly underpredicted at farther radial locations. Similar observations are reported by Chrigui et al. [99] with similar magnitude of discrepancies. The mean droplet velocity profiles of flame EtF4 are shown in Figure 6.9(c). The profiles show good agreement at z/D=10. Large discrepancies appear at z/D = 20 and 30. Similar levels of discrepancy are noted in the recent MMC-LES study for flames EtF1 and EtF4 [62], instead of under-
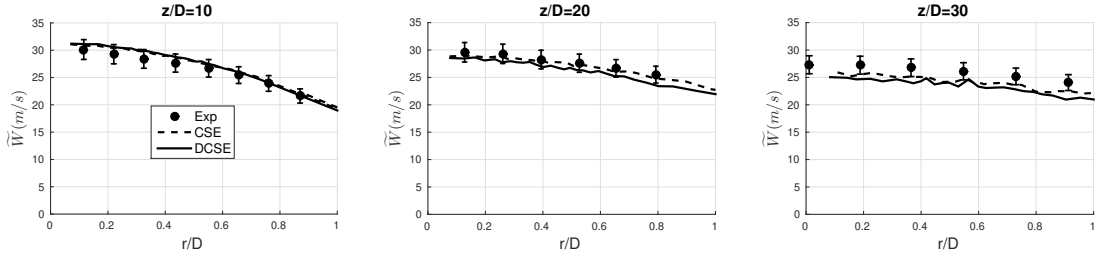
(a) EtF1
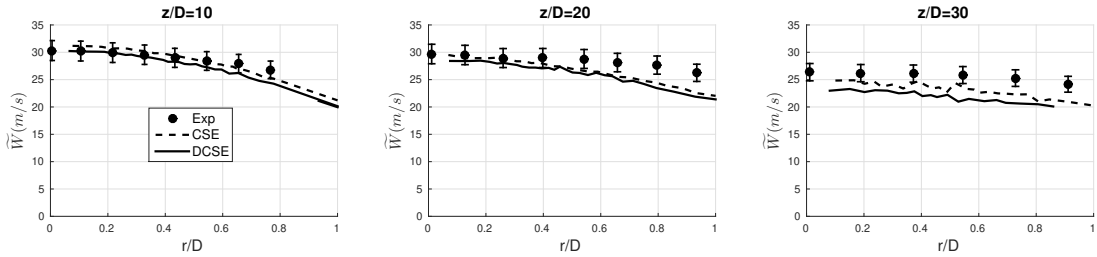
(b) EtF3
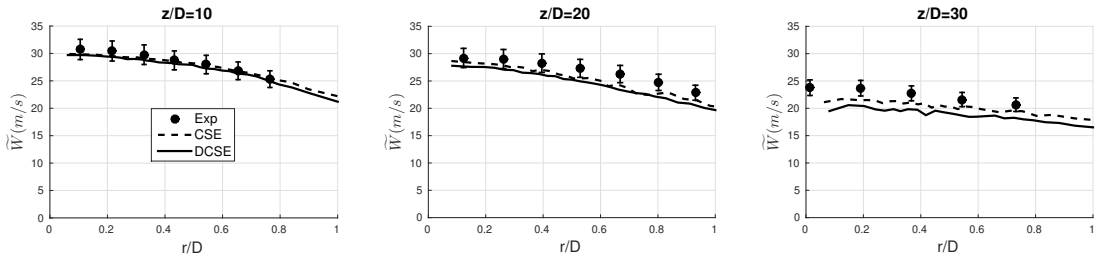
(c) EtF4

Figure 6.9: Radial mean droplet velocity profiles for all sizes of flames EtF1, EtF3, and EtF4 at different axial locations compared with the experimental data with the vertical bar at each experimental point indicating the experimental uncertainty [2]. Dashed lines represent current CSE-RANS implementation and solid lines current DCSE-RANS.

72
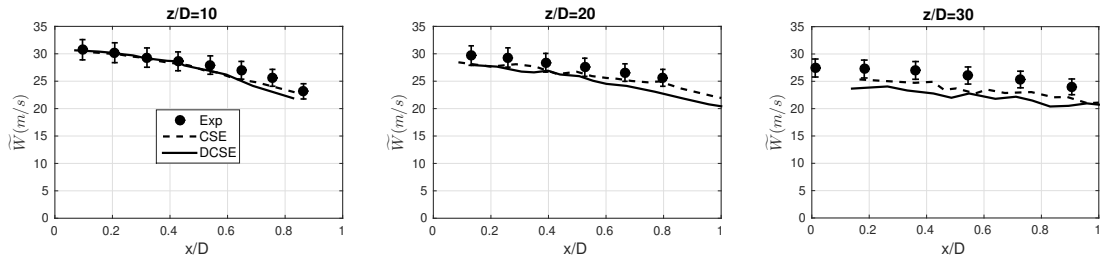
(a) EtF1
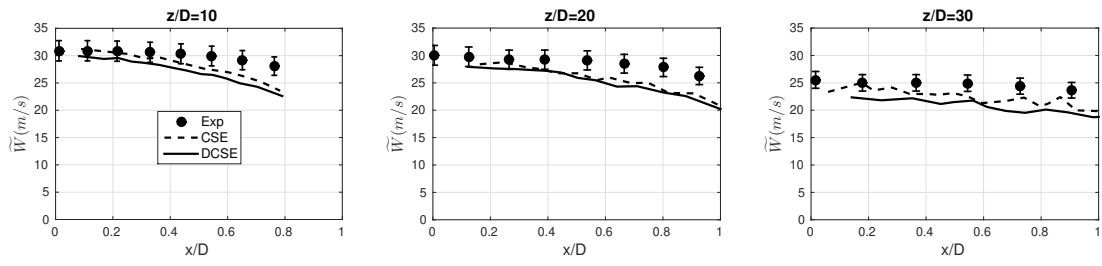
(b) EtF3
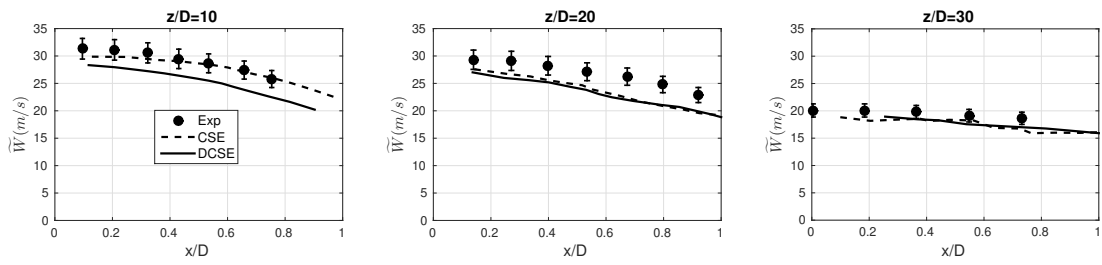
(c) EtF4

Figure 6.10: Radial mean droplet velocity profiles for $(0\mu m < d < 10\mu m)$ of flames EtF1, EtF3, and EtF4 at different axial locations compared with the experimental data with the vertical bar at each experimental point indicating the experimental uncertainty [2]. Dashed lines represent current CSE-RANS implementation and solid lines current DCSE-RANS.
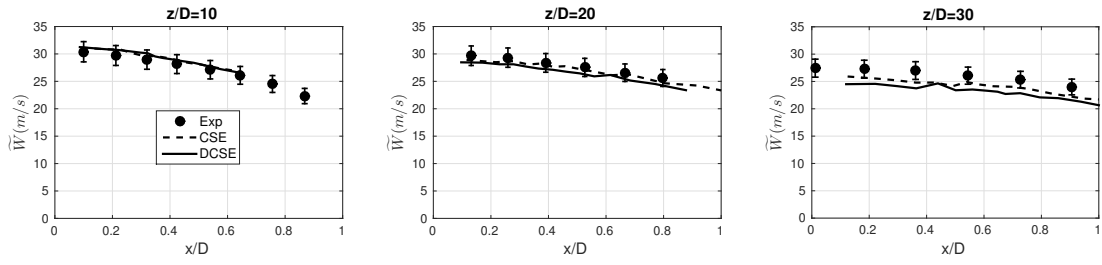
(a) EtF1
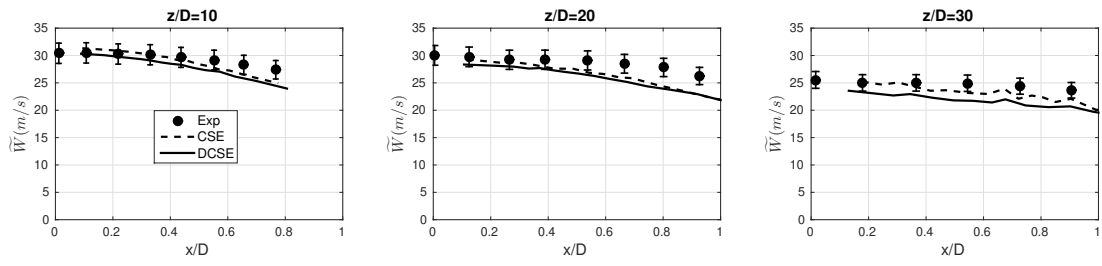
(b) EtF3
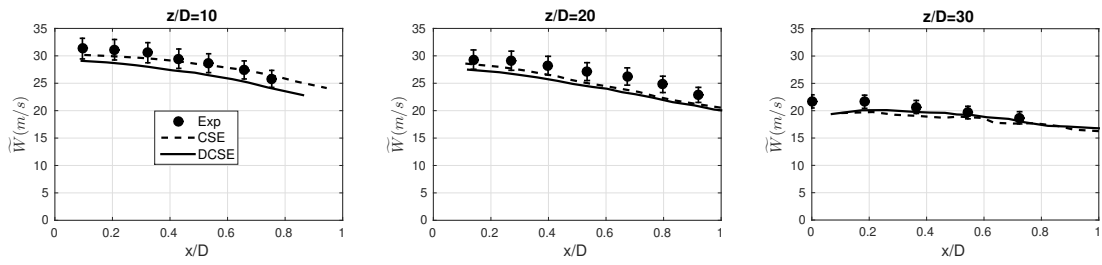
(c) EtF4

Figure 6.11: Radial mean droplet velocity profiles for ($20\mu m < d < 30\mu m$) of flames EtF1, EtF3, and EtF4 at different axial locations compared with the experimental data with the vertical bar at each experimental point indicating the experimental uncertainty [2]. Dashed lines represent current CSE-RANS implementation and solid lines current DCSE-RANS.
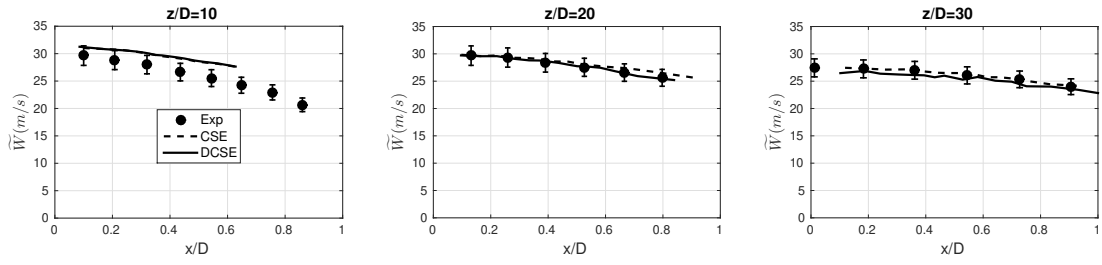
(a) EtF1

(b) EtF3

(c) EtF4

Figure 6.12: Radial mean droplet velocity profiles for $(40\mu m < d < 50\mu m)$ of flames EtF1, EtF3, and EtF4 at different axial locations compared with the experimental data with the vertical bar at each experimental point indicating the experimental uncertainty [2]. Dashed lines represent current CSE-RANS implementation and solid lines current DCSE-RANS.

predictions seen in the present work, overpredictions are shown, still persistent after testing different inflow conditions [62]. The velocity profiles obtained from LES of premixed FGM [101] show sim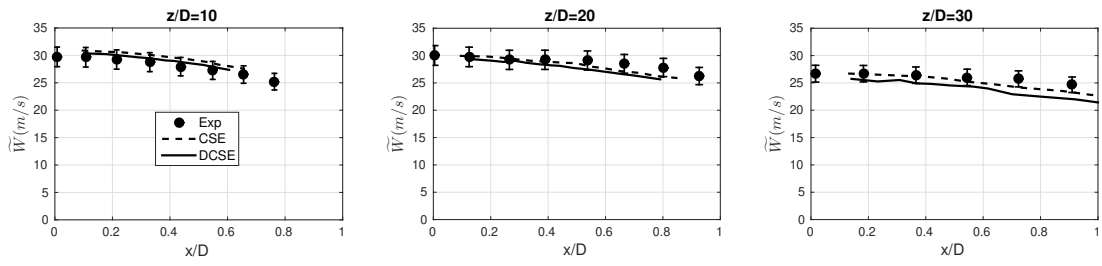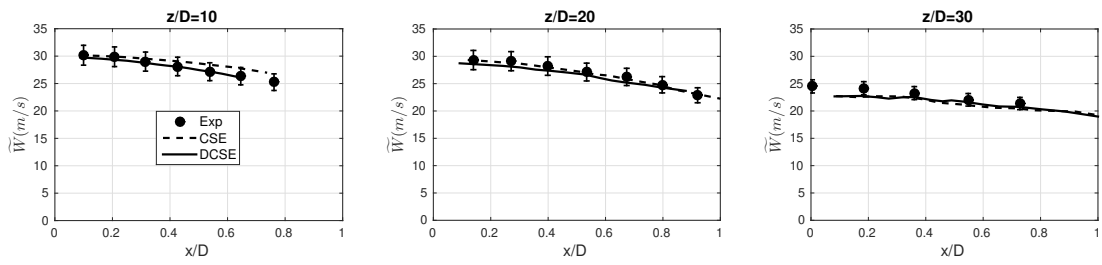ilar trends to the results obtained in the current study where underprediction is observed at z/D=20 and z/D=30 when a coarse mesh was used without sub-filter model. However, the results significantly improved with a finer mesh and inclusion of sub-filter models. This emphasizes the improvements expected from moving up to LES with careful attention to the sgs contribution modeling. The mean droplet velocities for the sizes of $(0\mu m < d < 10\mu m)$ are presented in Figure 6.10. CSE predictions are slightly higher compared to DCSE as a result of the overpredicted temperature, as can be seen in Figure 6.5. Moreover, the velocity tends to be underpredicted at most locations. This can be explained as the smaller droplets follow the gas phase velocity which is underpredicited as well due to jet spreading. Figure 6.11 presents the mean velocity of the intermediate droplet size $(20\mu m < d < 30\mu m)$. The same behavior of the small droplets can be observed. However, the level of discrepancy slightly decreases. For the larger droplets $(40\mu m < d < 50\mu m)$, the velocity is slightly overpredicted at z/D=10 and the predictions improves farther downstream as shown in Figure 6.12. The larger droplets retain their high inlet velocity near the nozzle exit since they have higher inertia and they do not follow the gas phase velocity decay unlike the smaller droplets. The predictions improve farther downstream since the large droplets have more time to closely flow the gas phase velocity. In addition, it is observed that the larger droplets tend to be concentrated near the centreline at z/D=10 and most of the droplets exist at radial location where (r/D<0.6). This occurs as the large droplets do not strictly follow the gas phase spreading due to their higher inertia. This also explains the drop in the Sauter mean diameter at farther radial distances as will be discussed in Section 6.5.5.

Liquid volume flux

The radial profiles of the liquid volume flux are shown in Figure 6.13. In general, the liquid volume flux is usually underpredicted for all the flames at the different locations and drops at increased axial distances due to further spray evaporation. It can be seen that the liquid volume flux magnitude of flame EtF1 is higher than EtF3 and EtF4 which corresponds to the liquid spray mass flow rate introduced at the nozzle exit, as shown in Table 6.1. For flame EtF1, the liquid volume flux displays good agreement with the experiment at all locations except near the centreline at z/D=10. The same trend can be seen for EtF3 and EtF4. It is also observed that the differences between CSE and DCSE are small for flames EtF1 and EtF4 at all locations and they arise mainly due to the temperature differences, as shown in Figure 6.5. However, the profiles display considerable mismatch between CSE

and DCSE for EtF3 at z/D=10. This can be explained by the overpredicted evaporation rate associated with CSE, as can be seen in Figure 6.7, where the mean evaporation rate is much higher at location closer to the nozzle exit. In addition, it is noted that the discrepancy level is inversely proportional with the fuel loading. For instance, in DCSE, the centreline volume flux is underpredicted by 20%, 35%, and 60% for EtF1, EtF3, and EtF4, respectively. This is consistent with the corresponding centreline temperature, as shown in Figure 6.5, where the higher temperature results in overpredicted evaporation rates. Similar trends were obtained in previous LES [100, 101, 62] for the different flames. A possible explanation for this underprediction is the uncertainty associated with the experiments which reaches 20% for the liquid volume flux measurements. Further, the liquid coating of the pipe wall observed in the experiment could lead to larger discrepancy near the centreline, as discussed in [62].

Sauter mean diameter

The radial profiles of the Sauter mean diameter are shown in Figure 6.14. Both CSE and DCSE provide similar results. Generally, the profiles are in good agreement with the experimental data at most locations for the three flames. However, the predicted Sauter mean diameter decreases at farther radial positions near r/D=0.5 at locations closer to the jet around z/D=10. This can be explained by the lack of large droplets at these locations. As can be seen in Figure 6.12, the large droplets do not follow the gas phase, since they have higher inertia, and they are concentrated near the jet centreline. This trend is observed for the three flames. At farther downstream locations, the predicted Sauter mean diameter mostly shows better results as the large droplets have the sufficient time to disperse and follow the gas phase distribution. It is worth noting that the profiles are slightly underpredicted in flame EtF3 at z/D=30. Previous LES [100, 101, 62] also show the same trend of underpredicted SMD at farther radial positions and at downstream locations. Overall, the spray statistics show reasonable agreement with the experiments and previously published simulations. Nevertheless, the evaporation rates are generally overpredicted and further investigation is required to provide more accurate results.
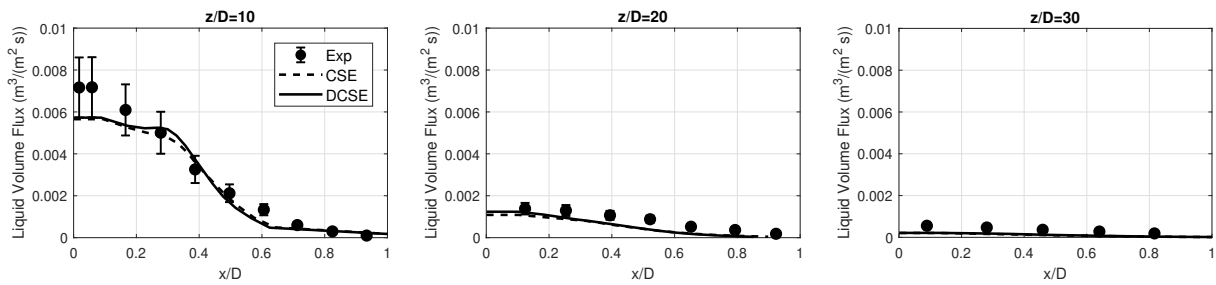
(a) EtF1
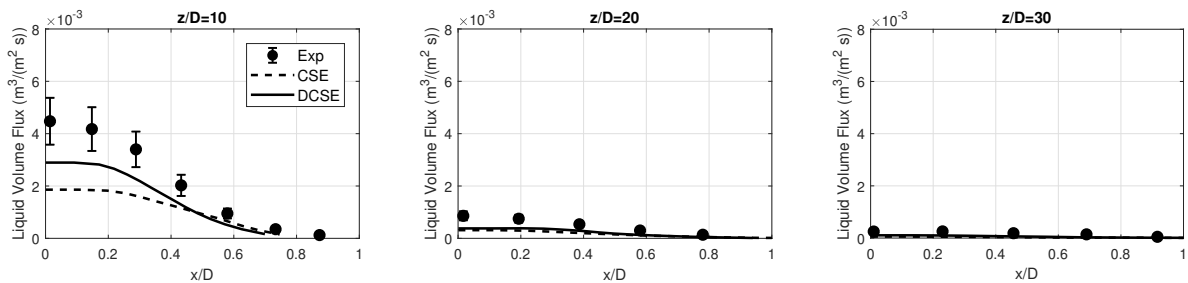
(b) EtF3
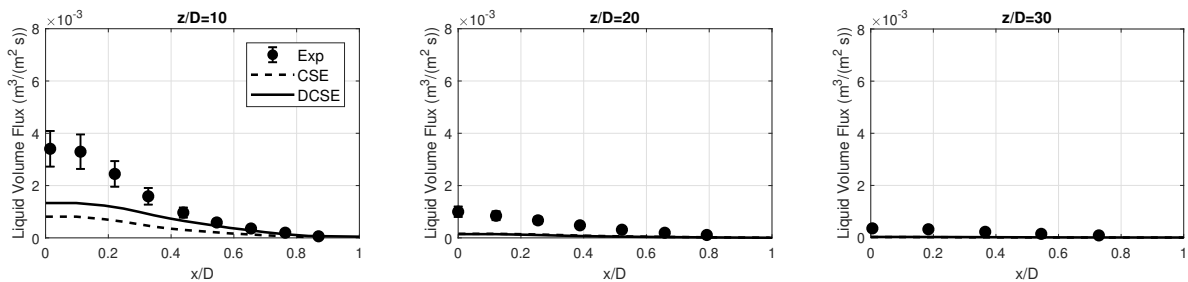
(c) EtF4

Figure 6.13: Radial mean liquid volume flux profiles in $(m^3/(m^2 s))$ of flames EtF1, EtF3, and EtF4 at different axial locations compared with the experimental data [2]. Dashed lines represent current CSE-RANS implementation and solid lines current DCSE-RANS.
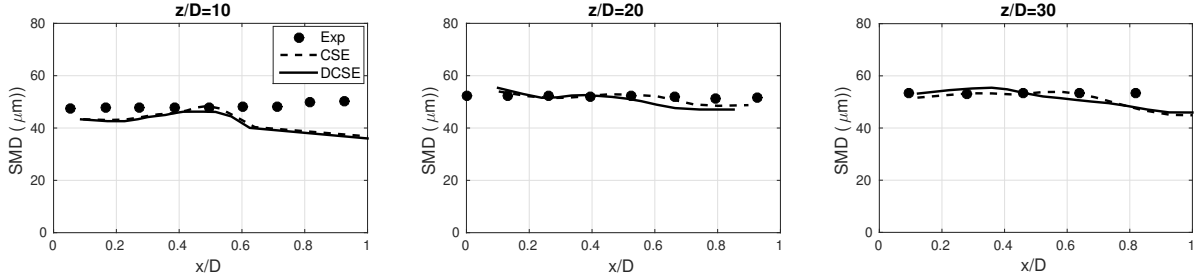
(a) EtF1
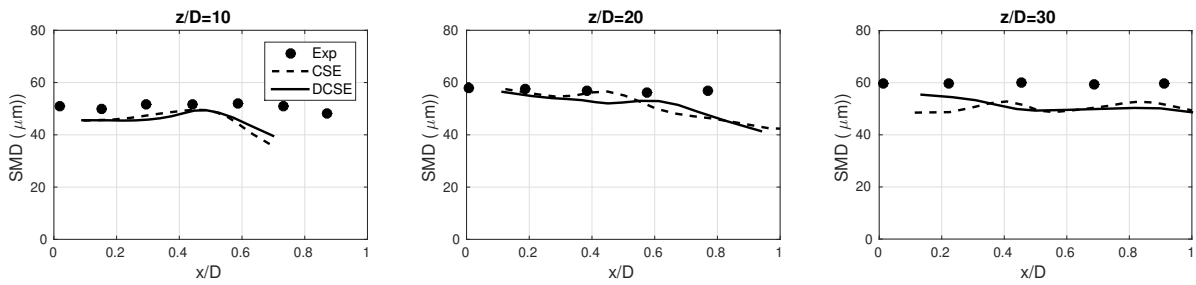
(b) EtF3
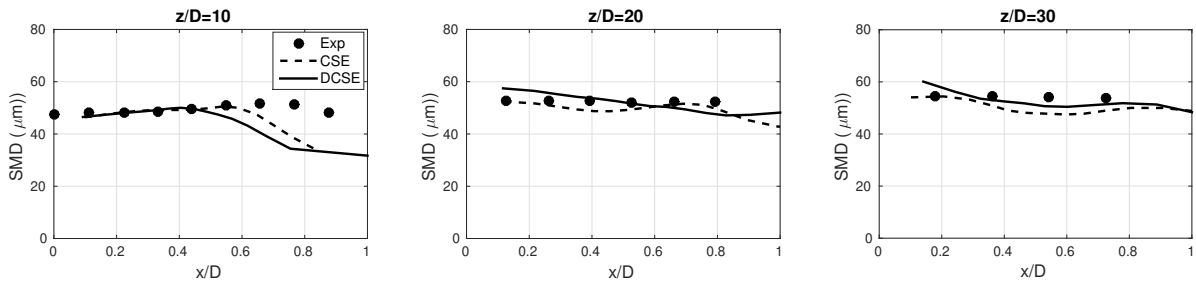
(c) EtF4

Figure 6.14: Radial profiles of mean Sauter mean diameter (SMD) in μm for flames EtF1, EtF3, and EtF4 at different axial locations compared with the experimental data [2]. Dashed lines represent current CSE-RANS and solid lines current DCSE-RANS.

6.6 Summary

This chapter compares the performance of CSE and DCSE in predicting the mean temperatures and spray velocities in three turbulent ethanol flames with varying degrees of premixing. RANS equations are solved along with the standard k-ε model with standard coefficients. The Eulerian-Lagrangian method with two-way coupling is used to account for the gas-spray interaction. In DCSE, a progress variable is defined as a second conditioning variable. The progress variable is defined as the mass fraction of CO_2. The predictions are compared with available experimental data and previously published numerical simulations of the same flames.

For the three flames, DCSE results in improved mean temperature predictions over CSE and the results are in close agreement with the experimental data, except for z/D = 10 near the centreline for flames EtF1 and EtF3 where the DCSE temperatures are clearly lower than the experimental values. These temperature underpredictions in the core jet were also observed in some previous studies using LES with different approaches and DNS, whereas temperature overpredictions were reported in other LES investigations with different sgs models. At these locations, near the jet exit, there may be a larger experimental error due to cooling effect on the thermocouples with larger amounts of droplets, probably combined with modeling errors due to the use of the standard k-ε model that may overpredict the jet spreading rate and underpredict the centreline values. Other modeling sources of error may be due to the joint PDF modeling, the neglect of evaporation effect on the conditional averages and the selected progress variable based on CO_2 only, for example. Otherwise, near the temperature peak location, CSE shows a temperature overprediction, while DCSE manages to improve the predictions significantly. For instance, in flame EtF1, the maximum temperature discrepancy drops from 25% in CSE to almost 0% in DCSE within the experimental uncertainty. However, the DCSE improvements over CSE seem to be small for EtF4 in which more partial premixing takes place. Further analysis of the mean HRR indicates that DCSE reproduced some features of the complex flame structure found in the selected flames, in particular a double peak in the mean HRR could be in EtF1 and EtF4 seen at some locations and DCSE could include the effect of larger conditional fluctuations more accurately than CSE. Flame EtF4 is shorter than the other flames and larger differences in the mean HRR and predicted temperature can be found upstream of the first measurement location. Farther downstream, CSE and DCSE produce similar temperatures due to low mean HRR and reduced level of conditional fluctuations.

Flames EtF1 and EtF3 are found to produce higher mean evaporation rates compared to flame EtF4 consistent with the introduced amount of spray into the domain. Further, the evaporation is seen to continue to farther axial distances in EtF1 and EtF3. In CSE, higher

mean evaporation rates are shown in flames EtF1 and EtF3 where the peak was closer to the nozzle exit due to higher predicted temperatures in comparison to DCSE.

The mixture fraction profiles display richer composition in flames EtF1 and EtF3, while flame 4 showes regions closer to the stoichiometric conditions. CSE results display slightly higher mixture fractions due to enhanced evaporation rates. The progress variable radial profiles show that CSE yields higher CO_2 mass fractions at most locations and are consistent with the predicted temperatures.

The predicted mean droplet velocity is in good agreement with the experimental data at z/D=10 and z/D=20. However, at z/D=30, the mean spray velocity is underpredicted for CSE and DCSE. Similar discrepancies were also reported in previous LES studies with similar formulations for the evaporation model. The small droplets follow the underpredicted gas phase in the axial and radial directions. In contrast, the large droplets exhibit velocity overpredictions at locations closer to the nozzle since they do not follow the gas velocity due to their high inertia. Further, this also produced a higher concentration of large droplets near the centreline.

The liquid volume flux is generally underpredicted, in particular near the centreline which indicates higher predicted evaporation rates. The same level of underpredictions has been encountered in previous numerical simulations [62, 100, 101]. Reasonable agreement with the experiments is obtained for the Sauter mean diameter. However, the predictions exhibit systematic underpredictions at farther radial positions as a result of the lower number of large droplets at these locations. Further investigation is needed to improve the currently available evaporation models.

In conclusion, DCSE is shown to improve CSE temperature predictions and produces good agreement with the experimental values.

Chapter 7

LES-CSE of turbulent ethanol flames coupled with non-adiabatic chemistry tabulation

In the last two chapters, three dimensional chemistry tabulations were generated using TGLDM technique [66] in adiabatic conditions. The initial RANS-CSE and RANS-DCSE temperature and droplet velocity predictions for acetone and ethanol showed good agreement with the experimental data. However, in RANS-CSE, the predicted radial temperature were often lower than the experimental values near the centreline and larger near the flame peak temperature. A shift radially outward for the predicted radial location of the peak temperature was also observed. The sources of modeling discrepancy were identified to be (i) the RANS limitations for accurate description of turbulent flow and mixing field, (ii) singly CSE formulation based on one conditioning variable, mixture fraction, that is limited for multi combustion regime and (iii) the neglect of evaporation effect on the conditional averages through the tabulated chemistry. Thus, for further investigation, Doubly Conditional-source Term Estimation (DCSE) was implemented in RANS in Chapter 6 for the series of turbulent ethanol spray flames and was shown to improve the temperature predictions compared to the singly CSE results by better capturing the partially premixed flame structure. Building upon our previous analysis, further investigation is conducted by using LES instead of RANS and incorporating the evaporation effect on the conditional averages in the tabulated chemistry.

LES presents an attractive compromise between RANS and DNS techniques. In LES, the large scales are resolved, while the small scales, beyond the filter width, are modeled. Accurate predictions may be obtained at a manageable computational cost. LES has shown

good performance in describing turbulent spray flames including different combustion models such as flamelet models [99, 100, 101, 102, 103], Conditional Moment Closure (CMC) [95, 111], and Multiple Mapping Conditioning (MMC) [62, 88].

The objectives of the current chapter are (i) to include the heat losses due to spray evaporation and gas radiation in the TGLDM tables and assess the impact of these changes on the temperature and droplet statistics, and (ii) to evaluate the performance of LES-CSE for a series of turbulent ethanol spray flames including one flame close to the blow-off limit. The three turbulent ethanol spray flames, EtF3, EtF6, and EtF8, from the Sydney database [2, 7] are selected. They have the same fuel loading with different carrier mass flow rates resulting in different Reynolds numbers and varying levels of pre-evaporation. Further, flame EtF8 has the highest velocity amongst the studied flames and is the closest to the blow-off limit.

7.1   LES equations

The Favre-filtered transport equations of mass, momentum, species mass fraction, and sensible enthalpy are given by

$$\frac{\partial \bar{\rho}}{\partial t} + \frac{\partial}{\partial x_i}(\bar{\rho}\tilde{u}_i) = \bar{\dot{\rho}}, \tag{7.1}$$

$$\frac{\partial}{\partial t}(\bar{\rho}\tilde{u}_j) + \frac{\partial}{\partial x_i}(\bar{\rho}\tilde{u}_i\tilde{u}_j) = -\frac{\partial \bar{p}}{\partial x_j} + \frac{\partial \bar{\tau}_{ij}}{\partial x_i} - \frac{\partial \tau_{ij}^{sgs}}{\partial x_i} + \bar{\dot{F}}_j, \tag{7.2}$$

$$\frac{\partial}{\partial t}(\bar{\rho}\tilde{Y}_k) + \frac{\partial}{\partial x_i}(\bar{\rho}\tilde{u}_i\tilde{Y}_k) = \bar{\bar{\omega}}_k + \frac{\partial}{\partial x_i}\left(\bar{\rho}(D + D_t)\frac{\partial \tilde{Y}_k}{\partial x_i}\right) + \bar{\dot{\rho}}_k, \tag{7.3}$$

$$\frac{\partial}{\partial t}(\bar{\rho}\tilde{h}) + \frac{\partial}{\partial x_i}(\bar{\rho}\tilde{u}_i\tilde{h}) = \frac{\partial}{\partial x_i}\left(\bar{\rho}(\alpha + \alpha_t)\frac{\partial \tilde{h}}{\partial x_i}\right) + \bar{\dot{Q}} + \bar{\dot{q}}_{react} + \overline{Q}_{rad}, \tag{7.4}$$

where ρ is the gas density, u_i the velocity in i direction, p the pressure, τ_{ij} the viscous stress tensor, Y_k the mass fraction of species k, $\bar{\bar{\omega}}_k$ the filtered chemical source term, h the sensible enthalpy, and $\dot{q}_{react}$ the enthalpy source term due to chemical reactions. $\bar{\dot{\rho}}$, $\bar{\dot{F}}_j$, and $\bar{\dot{Q}}$ are the spray source terms for mass, momentum, and energy transfer, respectively. $\overline{Q}_{rad}$ is the radiation heat loss, $\bar{\dot{\rho}}_k$ the mass transfer due to the evaporation of species k which is equal to $\bar{\dot{\rho}}$ in single fluid sprays and zero for all other species. τ_{ij}^{sgs} represents the sub-grid

scale (SGS) stress tensor described by the WALE model [119] in the current study. The SGS scalar fluxes are modeled by a standard gradient assumption. D and D_t represent the molecular and turbulent diffusivity, respectively. The turbulent diffusivity is determined from $D_t = \nu_t/Sc_t$, where Sc_t is the SGS Schmidt number. In the current study, three values of 0.4, 0.7, 0.9 have been tested for Sc_t. In the current investigation, the value of Sc_t is found to provide negligible effects on the time-averaged profiles. This may be explained by the fine mesh selected. Thus, a value of 0.7 is used for Sc_t in all the presented results the current study. α and α_t are the molecular and turbulent thermal diffusivities. A turbulent Prandtl number of 0.7 is also applied assuming a unity Lewis number. The radiation heat loss $\overline{Q}_{rad}$ is calculated from the main combustion product species carbon dioxide (CO_2), water (H_2O), and carbon monoxide (CO) based on the optically thin assumption [120], as described in Chapter 4.

The transport equations of the resolved mixture fraction, $\widetilde{Z}$ and its SGS variance, $\widetilde{Z''^2}$, are written as

$$\frac{\partial}{\partial t}(\bar{\rho}\tilde{Z}) + \frac{\partial}{\partial x_i}(\bar{\rho}\tilde{u}_i\tilde{Z}) = \frac{\partial}{\partial x_i}\left(\bar{\rho}(D + D_t)\frac{\partial \tilde{Z}}{\partial x_i}\right) + \bar{\dot{\rho}}, \tag{7.5}$$

$$\frac{\partial}{\partial t}(\bar{\rho}\widetilde{Z''^2}) + \frac{\partial}{\partial x_i}(\bar{\rho}\tilde{u}_i\widetilde{Z''^2}) = \frac{\partial}{\partial x_i}\left(\bar{\rho}(D + D_t)\frac{\partial \widetilde{Z''^2}}{\partial x_i}\right) + 2\bar{\rho}(D + D_t)\frac{\partial \tilde{Z}}{\partial x_i}\frac{\partial \tilde{Z}}{\partial x_i} - \bar{\rho}\widetilde{\chi}_z + \overline{\sigma_s}, \tag{7.6}$$

where χ_z is the SGS scalar dissipation rate (SDR) for mixture fraction, and $\overline{\sigma_s}$ the mixture fraction variance source term due to evaporation. The SGS SDR is modeled using a linear relaxation model following [100] as $\widetilde{\chi}_z = C_\chi(\widetilde{Z''^2}/\tau_t)$, where C_χ is a model constant set to 8 [100, 101], and τ_t is a turbulent SGS time scale calculated as $\tau_t \approx \Delta^2/max(D, D_t)$, where Δ represents the filter width. In LES for gaseous combustion, $C_\chi = 2$ is widely used. However, in spray combustion, droplet evaportion is expected to affect small scale mixing and further investigation is needed. De and Kim [121] examined three values of 2, 4, and 8, and a value of 8 is recommended. The unclosed evaporation source term in the SGS mixture fraction variance equation is closed following [122] as $\overline{\sigma_s} = \alpha\widetilde{Z''^2}(\bar{\rho}/\tilde{Z})$. A constant value of 0.5 is used for α in the current study as suggested by [123]. However, Pera et al. [122] suggested using a dynamic procedure to determine α.

7.2   Liquid phase formulation

The same Lagrangian model for liquid spray discussed in Chapter 3 is used for LES. The effects of the SGS velocity of the carrier phase on the drag of droplets are usually neglected

in the context of LES where the obtained resolved velocity are deemed sufficient. However, in the present study, the influence of the unresolved SGS of gas velocity fluctuations on the particle dispersion are calculated using a stochastic model. The resolved velocity is perturbed in random directions, with a Gaussian random number distribution. The distribution mean is taken to be zero and the variance is determined from the local root mean square (rms) value of the SGS velocity fluctuations. The rms velocity fluctuations are calculated from the SGS turbulent kinetic energy assuming isotropic turbulence.

7.3 CSE with non-adiabatic chemistry tables

This section provides a brief description of the current CSE implementation with non-adiabatic chemistry tables.

7.3.1 CSE description

The unconditional filtered chemical source term for species k is calculated as

$$\overline{\dot{\omega}_k}(x_j, t) = \overline{\rho} \int_0^1 \frac{\langle \dot{\omega}_k | \eta \rangle}{\langle \rho | \eta \rangle} \widetilde{P}(\eta, x_j, t) d\eta, \tag{7.7}$$

where x_j is the spatial coordinate, t the simulation time and η represents the mixture fraction sample space. The terms $\langle \dot{\omega}_k | \eta \rangle$ and $\langle \rho | \eta \rangle$ are the conditional chemical production rates and conditional density obtained from the chemistry tables. In the previous investigations of CSE in turbulent spray combustion in Chapters 5 and 6, $\langle \dot{\omega}_k | \eta \rangle$ is calculated as a function of the conditional species mass fractions of water $\langle Y_{H_2O} | \eta \rangle$ and carbon dioxide $\langle Y_{CO_2} | \eta \rangle$. In the current study, an additional parameter, namely the conditional enthalpy loss $\langle h_{loss} | \eta \rangle$, is required to account for heat losses in the four dimensional chemistry library. Thus, $\langle \dot{\omega}_k | \eta \rangle$ can be written as

$$\langle \dot{\omega}_k | \eta \rangle \approx \dot{\omega}_k \left(\langle Y_{CO_2} | \eta \rangle, \langle Y_{H_2O} | \eta \rangle, \langle h_{loss} | \eta \rangle \right) \tag{7.8}$$

The conditional parameters $\langle Y_{CO_2} | \eta \rangle$, $\langle Y_{H_2O} | \eta \rangle$, and $\langle h_{loss} | \eta \rangle$ at each ensemble are obtained by performing integral inversion, as described in Chapter 4.
In Equation 7.7, $\widetilde{P}(\eta, x_j, t)$ represents the filtered density function FDF calculated from $\widetilde{Z}$ and $\widetilde{Z''^2}$ assuming a β distribution.

7.3.2 Non-adiabatic chemistry tables

Non adiabatic TGLDM chemistry tables are generated prior to the LES-CSE calculations. Marinov detailed chemistry mechanism for ethanol [5] is selected including 56 species and 383 reactions. Fifty different values of η are included ranging from 0.001 to 0.99, with finer resolution around the stoichiometric mixture fraction ($\eta_{st} = 0.1$). The number of η bins was tested and shown to give η grid independent results in Chapter 5. Six different values of conditional heat loss are tabulated starting from adiabatic conditions and reaching a maximum total enthalpy loss of 50%. The number of tabulated enthalpy loss values were tested and six levels are shown to be sufficient. For comparison, three tabulated values are included in the work of Ma et al. [89] for the Delft Spray-in-Hot-Coflow flame. The filtered enthalpy loss is calculated during the LES-CSE calculation. For this, an additional transport equation is solved for the filtered adiabatic sensible enthalpy $\widetilde{h_{ad}}$ by removing the source terms associated with radiation and spray evaporation from Equation 7.4. Then, the filtered enthalpy loss is calculated as $\widetilde{h_{loss}} = \widetilde{h} - \widetilde{h_{ad}}$. The conditional enthalpy loss in each ensemble $\langle h_{loss}|\eta \rangle$ is calculated by inverting the following integral

$$\widetilde{h_{loss}}(x_j, t) = \int_0^1 \langle h_{loss}|\eta \rangle (t) \widetilde{P}(\eta; x_j, t) d\eta. \tag{7.9}$$

The conditional enthalpy loss $\langle h_{loss}|\eta \rangle$ is used to determine the enthalpy level in the chemistry library. A linear interpolation is performed to retrieve the corresponding conditional averages needed to determine $\langle \dot{\omega}_k|\eta \rangle$ in Equation 7.7.

7.4 Experimental configuration and numerical setup

The experimental set of ethanol spray flames from the university of Sydney [2, 7] is used in the current study. The same database was used in Chapter 6, where flames EtF1, EtF3, and EtF4 were studied. In this chapter, EtF3, EtF6, and EtF8 are selected with their experimental details summarized in Table 7.1. These three flames have the same fuel flow rate with an increasing bulk velocity of 24 m/s, 36 m/s, and 48 m/s, respectively. These flames are considered so that varying levels of turbulence and leaner conditions can be studied. Further, flame EtF8 is the closest to the blow-off limit.

The computational domain consists of a cylinder with a height of 420 mm and a diameter of 120 mm. The computational grid includes 500, 80, and 64 divisions in the axial,

Table 7.1: Experimental details for the selected flames [7]

	EtF3	EtF6	EtF8
Bulk velocity (m/s)	24	36	48
Carrier	Air	Air	Air
Carrier mass flow rate (g/min)	150	225	301
Liquid fuel injection rate (g/min)	45	45	45
Liquid fuel rate at inlet (g/min)	30.7	41.3	36.6
Vapour fuel rate at inlet (g/min)	14.3	3.7	8.4
Overall equivalence ratio	2.9	1.9	1.4
Z_{jet}	0.087	0.016	0.027
Z_{Pilot}	0.1	0.1	0.1
Jet Reynolds number	19678	26422	34848

radial, and circumferential directions, respectively, resulting in 2,560,000 cells. The computational mesh is refined in the shear layer and close to the jet exit plane where higher scalar gradients are expected. The spatial filter width reaches 0.12 mm in the refined regions. The current mesh resolves more than 90% of the turbulent kinetic energy near the shear layer. A finer mesh with 3,600,000 cells was investigated for grid independence, and no significant improvement in the time-averaged quantities was detected. The computational domain is divided into 40 CSE ensembles in the axial direction following previous simulations in Chapter 5 and Chapter 6. The ensembles are selected such that they have an approximately equal number of cells for best parallel computational efficiency.

The simulations are performed using OpenFOAM-7.0 with a finite volume low Mach number pressure-based solver. Parallel processing is performed using 40 processors (Intel Skylake 2.4 GHz). The time-averaged statistics are collected for approximately 6 flow-through times based on the carrier bulk velocity and require approximately 60 hours.

An implicit second-order backward scheme is applied for the time derivatives. A Gauss linear scheme is used for gradients and Gauss limited linear for the divergence scheme. The diffusion term is approximated by the second-order Gauss Linear limited scheme. Zero-gradient boundary conditions are applied for all scalars at the outlet and the sides. The temperature, species mass fractions, and mixture fractions are defined at the jet, pilot, and coflow to match the reported experimental values. The digital filtering technique proposed by Klein et al. [124] is selected to generate the inflow turbulence. The mean velocity profile at the jet is obtained from the experimental measurements. The Reynolds stress tensor is obtained from the reported rms at the jet exit plane [2]. At the outlet and cylinder sides, wave-transmissive outflow boundary conditions [125] are applied for both pressure and velocity to stabilize the solutions and prevent wave reflections.

7.5 Results

7.5.1 Gas phase results
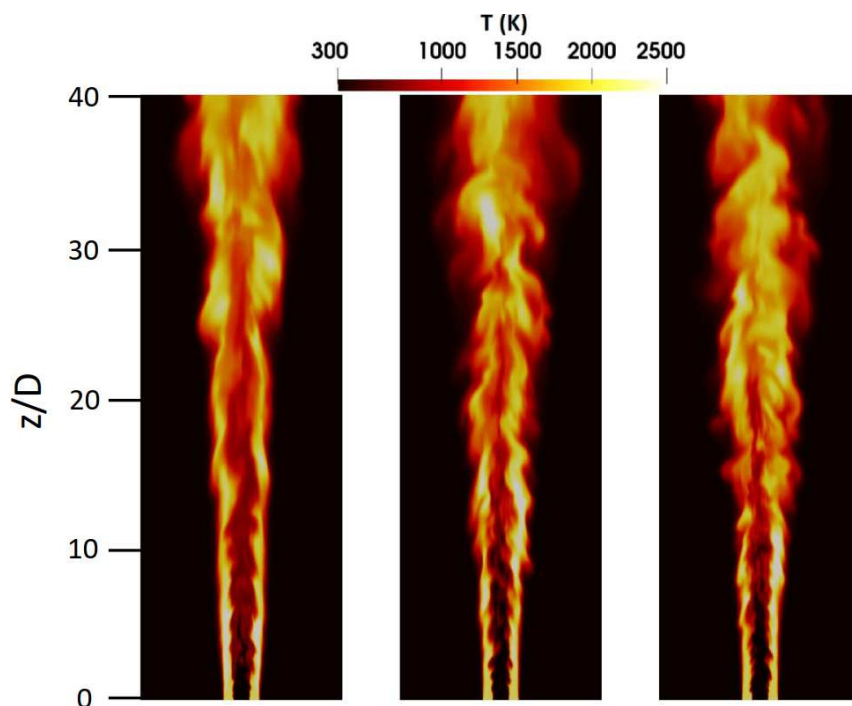
Figure 7.1: Instantaneous contour plots of the gas temperature for flames EtF3 (left), EtF6 (middle), and EtF8 (right) using the non-adiabatic TGLDM tables. z is the axial distance from the nozzle exit and D = 10.5 mm.

Before examining the time averaged statistics, several instantaneous snapshots are presented. For qualitative visualization of the flames EtF3, EtF6 and EtF8, some instantaneous temperatures obtained by LES-CSE with non-adiabatic TGLDM are shown in Figure 7.1. As can be seen, flame EtF3 exhibits smaller turbulence levels, in particular at the flame outer surface due to lower velocity compared with the other two flames. The turbulent production in the shear layer is low since the relative velocity between the jet and the pilot is small. In contrast, flames EtF6 and EtF8 reveal higher turbulence levels close to the jet exit where jet break-up is visible.

Further information may be obtained from the heat release rate (HRR). Figure 7.2 presents snapshots of the instantaneous HRR using the non-adiabatic TGLDM for EtF8 compared with instantaneous contours from the experiment at specific axial locations. The HRR
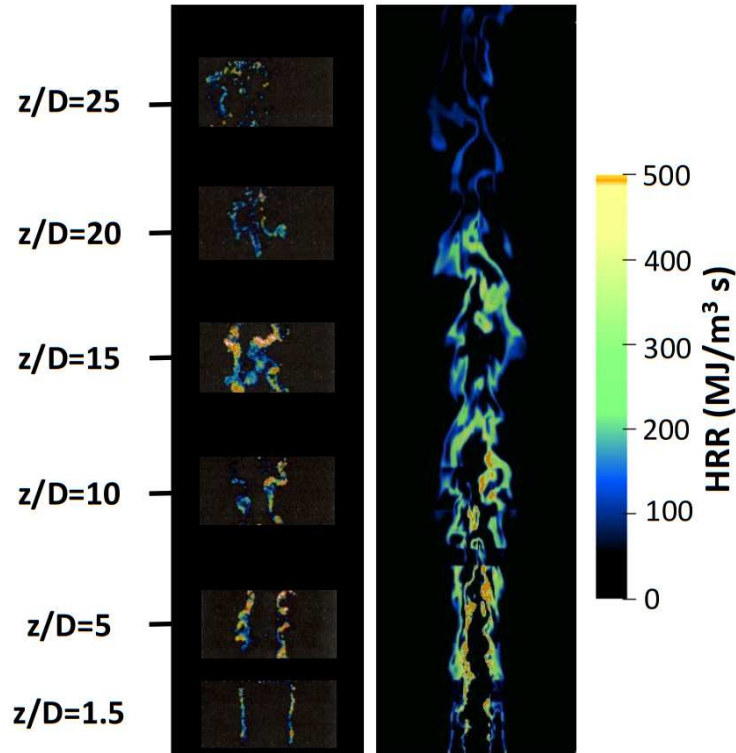
Figure 7.2: Instantaneous contour plots of the HRR for flame EtF8 extracted from the case with non-adiabatic TGLDM (right) compared with the results from the experiments at specific axial distances (left) reproduced from [2].

provides a representation of the flame structure as it shows the regions of high chemical reactions. It can be seen that the current LES captures the regions of high reaction rates. However, up to z/D=10, LES-CSE indicates higher reaction rates and slightly wider reaction zone when compared with the experiment. The HRR drop found at z/D=20 and z/D=25 can be seen in both experimental and LES contours. Further, around z/D=10, some breaks in the HRR are visible in the experiment as well as LES which represent regions of local extinction [2].

The time-averaged temperature profiles of flames EtF3, EtF6, and EtF8 are shown in Figure 7.3. Compared with the experimental data, in flame EtF3, the LES-CSE temperatures are underpredicted near the centreline at z/D=10 and z/D=20. However, the centreline predictions significantly improve at z/D=30. The LES-CSE appears to predict much lower mixing rates between the pilot gases and the inlet jet stream at the first axial locations.

Similar temperature underpredictions are seen in previously published studies for the same flame, in DNS [104] (at z/D = 10 only) and LES-FGM [99]. These discrepancies may be the results of combined experimental errors and SGS modeling errors. As can be seen in Figure 7.3, the LES temperatures predictions using adiabatic and non-adiabatic TGLDM are close to each other in flame EtF3 at all locations. The LES-CSE with adiabatic TGLDM provides slightly better agreement with the experiment near the centreline at z/D=10, and z/D=20, while the LES-CSE with non-adiabatic TGLDM yield closer temperature peak magnitudes and locations relative to the experimental profiles. The larger centreline temperature drop obtained by the non-adiabatic TGLDM is caused by the higher spray evaporation heat loss experienced near the centreline that is included in the simulation. Compared to the RANS-CSE results in Chapter 6, the current LES-CSE with non adiabatic TGLDM shows some improvements at all locations, although smaller than initially expected.

For flame EtF6, the centreline temperature is underpredicted at z/D=10 in LES, similar to what is seen in flame EtF3. However, the centreline temperature underprediction is smaller than what is found in flame EtF3. Flame EtF6 has higher jet velocity and the shear layer develops faster promoting better mixing at distances closer to the jet exit section. Further, the LES-non-adiabatic TGLDM temperature predictions are in better agreement with the experiments near the temperature peak location with noticeable underprediction near the centreline. Previously published LES-FGM [102] also shows significant centreline temperature underprediction at z/D=10 and z/D=20. In flame EtF8, the predicted temperature near the centreline is reproduced better than that of EtF3 and EtF6, maybe due to the higher jet velocity and faster development of the shear layer. The peak temperature magnitude is overpredicted at all locations using CSE with adiabatic TGLDM. In contrast, LES-CSE with the non-adiabatic TGLDM substantially improves the temperature predictions, in particular at z/D=10 and z/D=20. For flame EtF8, the peak temperature is shifted radially outward at z/D=10 and z/D=20 for LES-adiabatic TGLDM. However, with the LES-non-adiabatic TGLDM, a slight improvement is seen for the radial location of the peak temperature. This is in agreement with Figure 7.2 with LES displaying a wider flame as a result of the higher reaction rates near the stoichiometric region. Similar observations have also been noticed in the RANS-CSE simulations of ethanol flames where DCSE improved the results. Previous LES studies [101, 99] also noted some temperature discrepancies near the peak at the first two axial locations for the same flame.

The effect of heat losses is further investigated by examining the heat loss contribution due to spray evaporation and gas radiation. As shown in Figure 7.4, the heat loss due to spray evaporation has a larger contribution to the total heat loss compared to the radiation heat losses at all locations. This supports the conclusion of previous studies [90, 95, 89] that evaporation effects must be included in the chemistry tabulation. The spray heat

90

Figure 7.3: Time-averaged radial temperature profiles for flames EtF3 (top), EtF6 (middle), and EtF8 (bottom) at different axial locations compared with the experimental data with the vertical bar at each experimental point indicating the experimental uncertainty [2]. Solid lines represent LES with adiabatic TGLDM, dashed lines LES with non-adiabatic TGLDM. Dotted lines are for previous RANS solution with adiabatic TGLDM for EtF3 only. RANS-CSE predictions for flames EtF6 and EtF8 are not available.

losses are larger near the centreline where higher evaporation rates are expected at the measurement locations. In contrast, radiation heat losses are negligible near the centreline and reach their maximum value near the peak temperature locations. This is explained by the presence of higher temperature and concentration of radiative species, as prescribed from the optically thin radiative model. It is interesting to note that flame EtF6 exhibits the highest spray heat losses, while flames EtF3 and EtF8 show slightly lower magnitudes. This needs to be placed in the context that the evaporation rate depends on the spray velocity, gas temperature, and the mass flow rate of injected liquid spray. This aspect is examined for the three flames.

Figure 7.5 shows the centreline distribution of the heat loss due to evaporation only. Although EtF3 has the lowest mass flow at the jet exit, it shows the highest initial evapo-
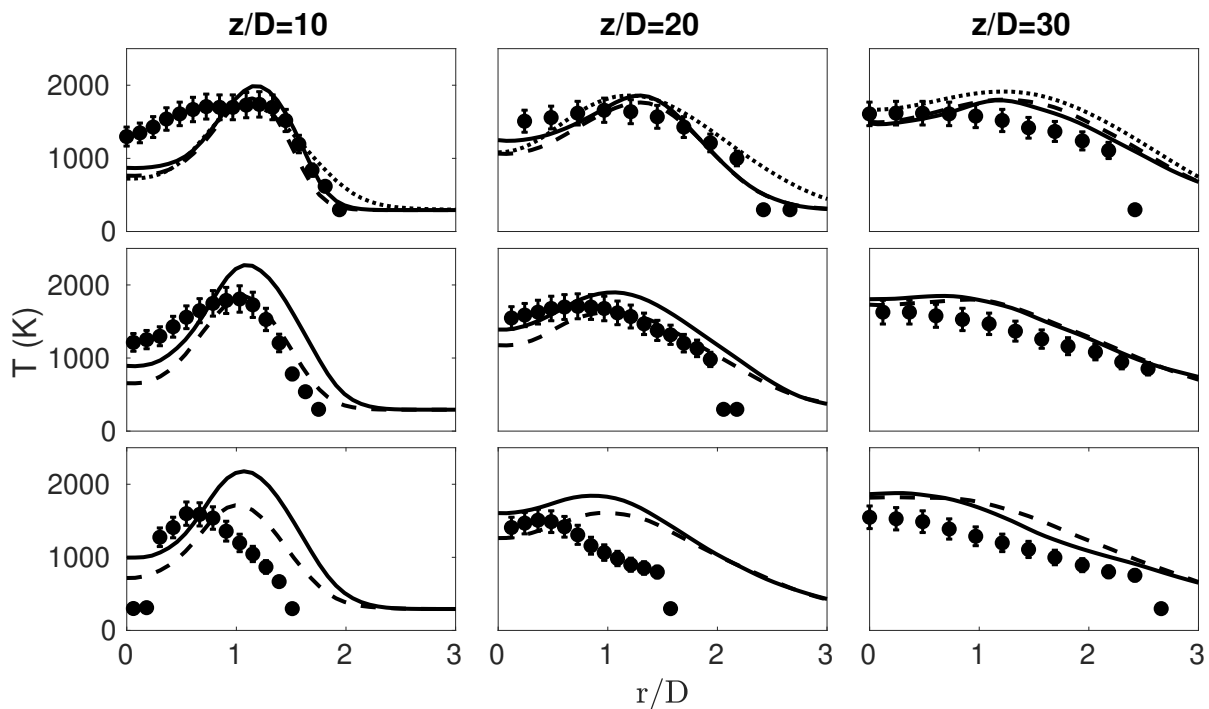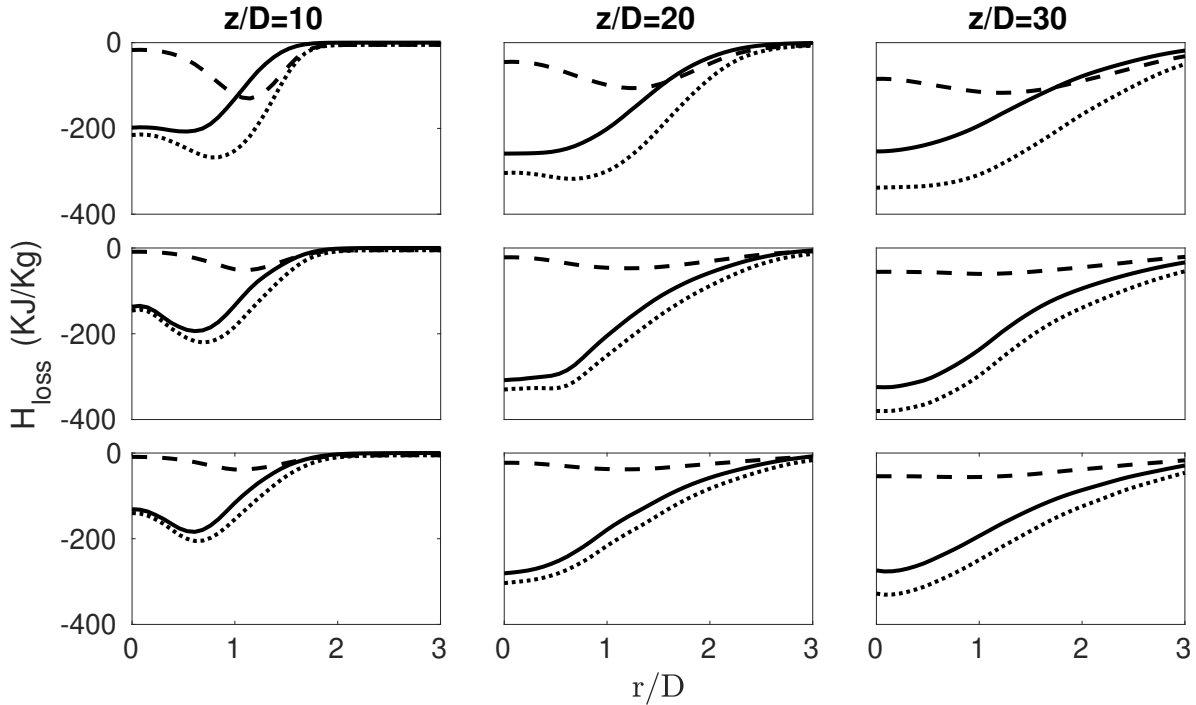
Figure 7.4: Radial time-averaged heat loss profiles of flames EtF3 (top), EtF6 (middle), and EtF8 (bottom) at different axial locations extracted from the cases with non-adiabatic TGLDM. Solid lines represent heat loss due to spray evaporation. Dashed lines represent heat loss due to gaseous radiation. Dotted lines represent the total heat loss.

ration heat loss for z/D <10. This can be explained by flame EtF3 having the lowest jet and spray velocities leading to a higher droplet residence time where the droplets are exposed to the hot reacting gases for longer times leading to higher evaporation heat losses. The evaporation heat loss for the three flames reaches a peak around z/D=25 where it begins to decrease due to the lower amount of spray present due to evaporation. Flames EtF6 and EtF8 show similar evaporation heat losses up to z/D=15. However, EtF6 starts to show larger heat losses as it has higher initial spray flow rate and higher residence time. As seen in Figure 7.5, the largest evaporation heat loss difference is found at z/D=10 and decreases at farther axial distances. As noted in Figure 7.3, the largest temperature difference is found at z/D=10 and decreases farther downstream for all flames. For example, flame EtF8 exhibits the highest temperature difference, while it has generally the lowest heat loss. The peak temperature difference at z/D=10 is 9%, 22%, and 28% for EtF3, EtF6, and EtF8, respectively. This can be explained by the effect of the enthalpy deficit

92
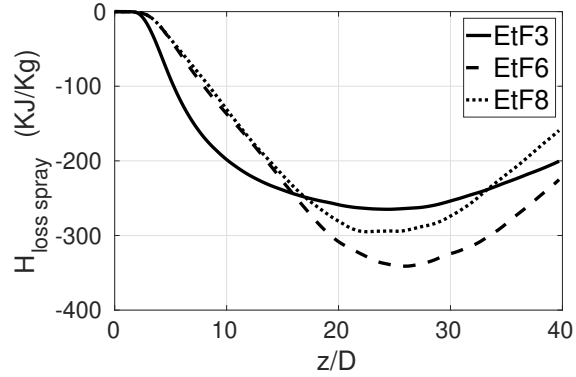
Figure 7.5: Axial time-averaged heat loss profiles of the three flames extracted from the cases with non-adiabatic TGLDM. Solid line represents EtF3, dashed line represent EtF6, and dotted line represents EtF8.

on chemical reaction rates and species concentration only visible in the flammable region where significant reaction rates exist, and considerably decreases outside the flammability limits. Therefore, the difference between the adiabatic and non-adiabatic TGLDM predictions is expected to be highest around stoichiometry and decreases away from stoichiometry. The link between mixture stoichiometry and HHR is further explored. Figures
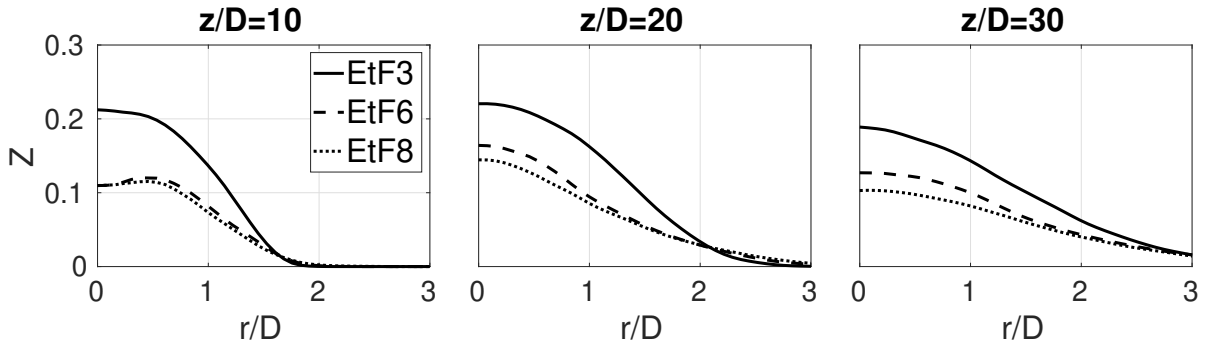
Figure 7.6: Radial time-averaged mixture fraction profiles of flames EtF3 (solid lines), EtF6 (dashed lines), and EtF8 (dotted lines) at different axial locations extracted from the cases with non-adiabatic TGLDM.

7.6 and 7.7 show the radial profiles of the time-averaged mixture fraction and heat release rate, respectively, from LES-non-adiabatic TGLDM. The heat release rate is the source term in the enthalpy equation and the main contributor to the temperature change due to chemical reactions. As can be seen in Figure 7.6, EtF3 has a richer composition at all locations with a maximum $\widetilde{Z}$ value of 0.22 which lies approximately on the upper flammability limit of ethanol combustion and far from the stoichiometric value ($\eta_{st} = 0.1$). In
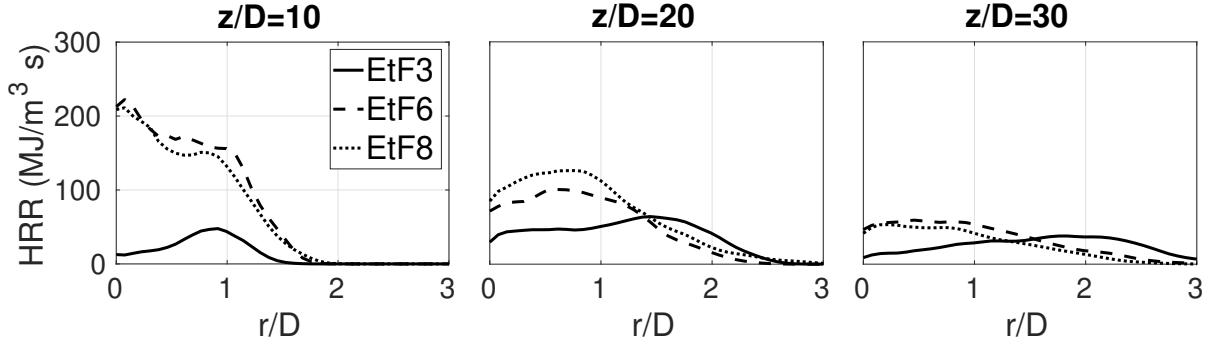
Figure 7.7: Radial time-averaged heat release rate profiles of flames EtF3 (solid lines), EtF6 (dashed lines), and EtF8 (dotted lines) at different axial locations extracted from the cases with non-adiabatic TGLDM.

contrast, flames EtF6 and EtF8 have lower $\widetilde{Z}$ values. Therefore, they burn primarily close to the stoichiometric conditions. This explains the higher HRR encountered in EtF6 and EtF8 at z/D=10 compared to the lower HRR in EtF3, as seen in Figure 7.7. The HRR is maximum at z/D=10 for EtF6 and EtF8 and decreases with the axial direction. However, EtF3 reveals maximum HRR near z/D=20, unlike EtF6 and EtF8. At z/D=30, the three flames show small HRR. The enthalpy loss effect on the temperature predictions closely follows the HRR profiles. For example, the temperature difference is larger between those obtained by LES-adiabatic TGLDM and those with LES-non-adiabatic TGLDM in flames EtF6 and EtF8 near z/D=10 (Figure 7.3). This corresponds to the largest HRR values as shown in Figure 7.7. Likewise, the enthalpy loss effects are negligible at z/D=30 where the HRR is minimum. Further, flame EtF8 includes lower HRR values and temperatures compared to EtF6 at z/D=10 due to local extinction that decreases the time-averaged HRR and temperature.

Figure 7.8 shows the conditional mass fractions of CO_2 and H_2O at z/D=10 and z/D=30 for flame EtF8 using the non-adiabatic chemistry tables. The conditional mass fractions of CO_2 and H_2O are shown as they are obtained directly from the integral inversion and they determine the conditional chemical reaction rates. The profiles show identical predictions

in the rich regions up to the stoichiometric mixture fraction where the profiles start to exhibit different behavior. The conditional mass fractions begin to decrease for z/D=10 and increase for z/D=30. It is worth noting that the maximum mean mixture fraction is approximately 0.12 and 0.1 for z/D=10, and z/D=30, respectively, as shown in Figure 7.6. Thus, the conditional means at mixture fractions higher than these values do not provide an accurate statistical description. In addition, these values have negligible effects after averaging with the FDF to obtain the filtered mean quantities.
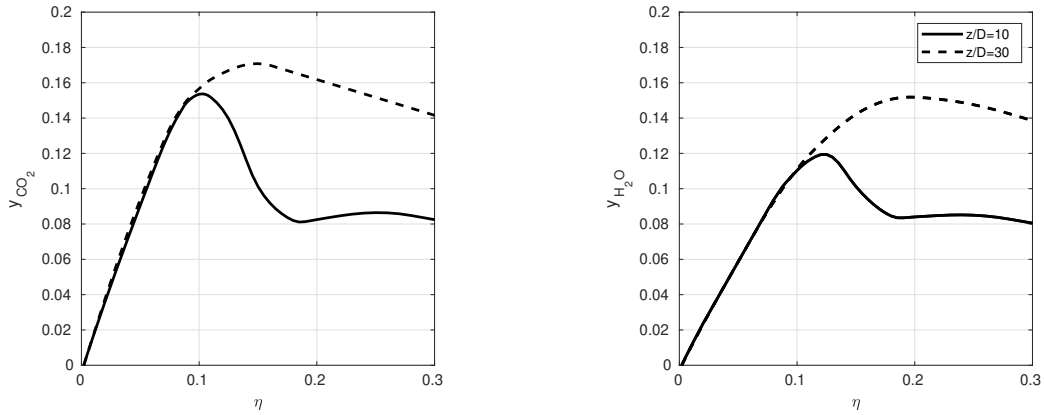
Figure 7.8: Conditional mass fractions of CO_2 and H_2O at z/D=10 and z/D=30 for flame EtF8 using the non-adiabatic chemistry tables.

7.5.2 Droplets statistics

The droplet axial mean velocity and RMS are presented in Figure 7.9. In general, good agreement between the predicted results and the experimental profiles is observed at the different locations. The mean axial velocity is well captured for EtF3 and EtF6, while underpredicted for flame EtF8, in particular, for z/D>20. This can be explained by the underpredicted gas temperature at these locations. The same behaviour for EtF8 has been observed in other LES studies [101, 99].
The velocity rms is slightly underpredicted at z/D=30 in EtF3. The discrepancy in the velocity rms can be attributed to using a relatively simple stochastic dispersion model assuming isotropic turbulence. In comparison with other LES studies [62, 100], the present rms predictions are in excellent agreement with the experimental values. When comparing the predictions using the LES-CSE with adiabatic and non-adiabatic TGLDM, a slight

95

discrepancy in the mean velocity and RMS is noticed. The adiabatic TGLDM shows regularly higher velocities consistent with the higher mean temperatures at the same locations as a result of the higher thermal expansion. Therefore, the mean velocity using adiabatic TGLDM show predictions closer to the experiment for EtF8 since the mean velocity is generally underpreddicted for both cases. Regarding the velocity rms, the non-adiabatic cases bring small improvement in the predictions.

Figure 7.10 shows the radial profiles of the Sauter mean diameter at different locations. For the three flames, the SMD profiles show good agreement with the experiments for z/D>10. At z/D=10, a close match between LES and experiments is found close to the centreline. However, the SMD significantly drops for r/D>0.6. A possible explanation is the lack of turbulent dispersion required to push the large droplets radially outward. Therefore, the large droplets are concentrated near the centreline while the small droplets closely follow the gas phase dispersion due to their lower momentum. Similar underpredictions near z/D=10 at farther radial locations are also observed in other LES studies [100, 101] and previous RANS-CSE in Chapter 5 show the same behaviour at z/D=10.
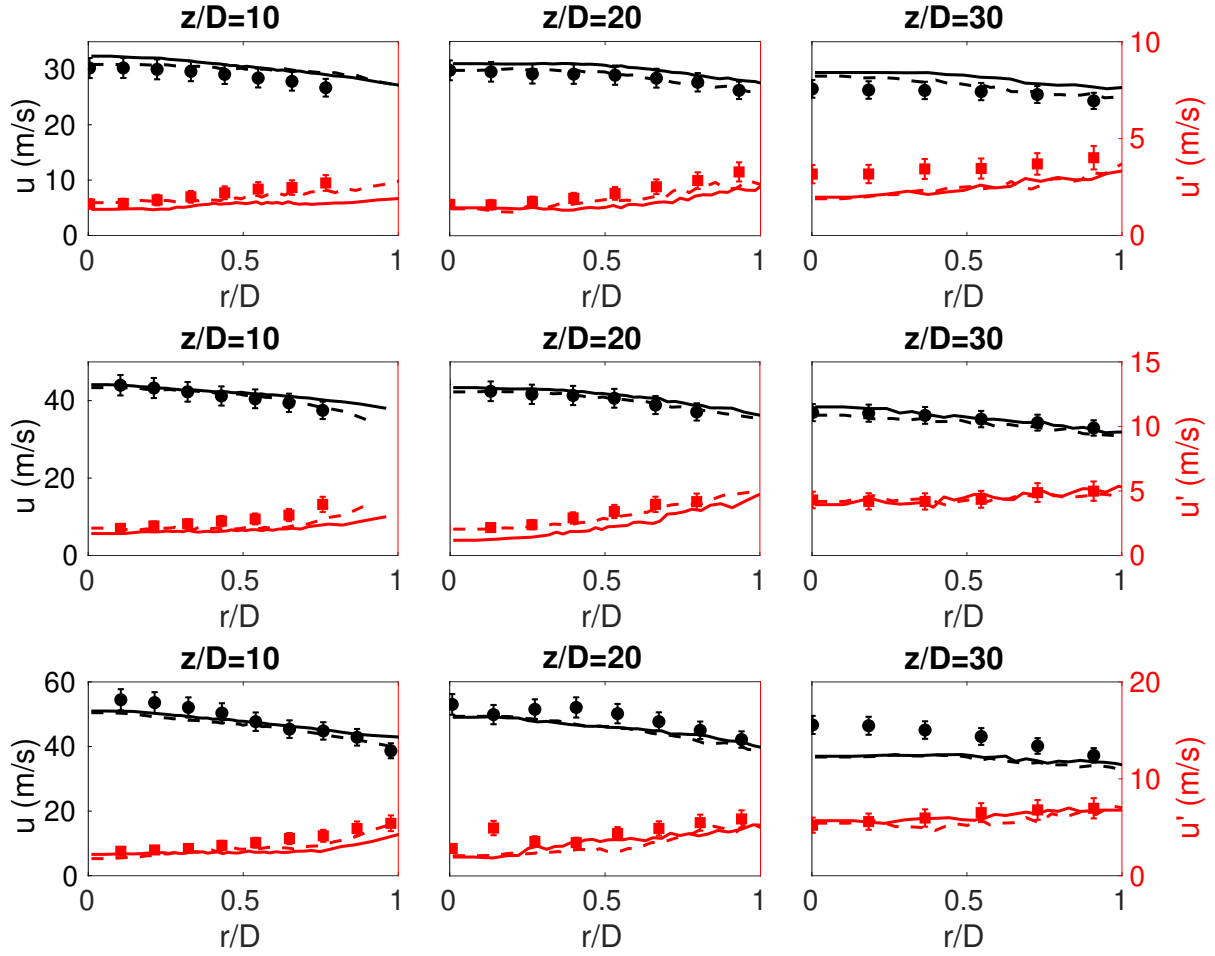
Figure 7.9: Radial profiles of droplet mean axial velocity and RMS axial velocity for all sizes at different axial locations for EtF3 (top), EtF6 (middle), and EtF8 bottom. Black lines represent mean axial velocity (u, left axis) and red lines represent RMS of axial velocity (u', right axis). Solid lines represent solutions with adiabatic TGLDM. Dashed lines represent solutions with non-adiabatic TGLDM.
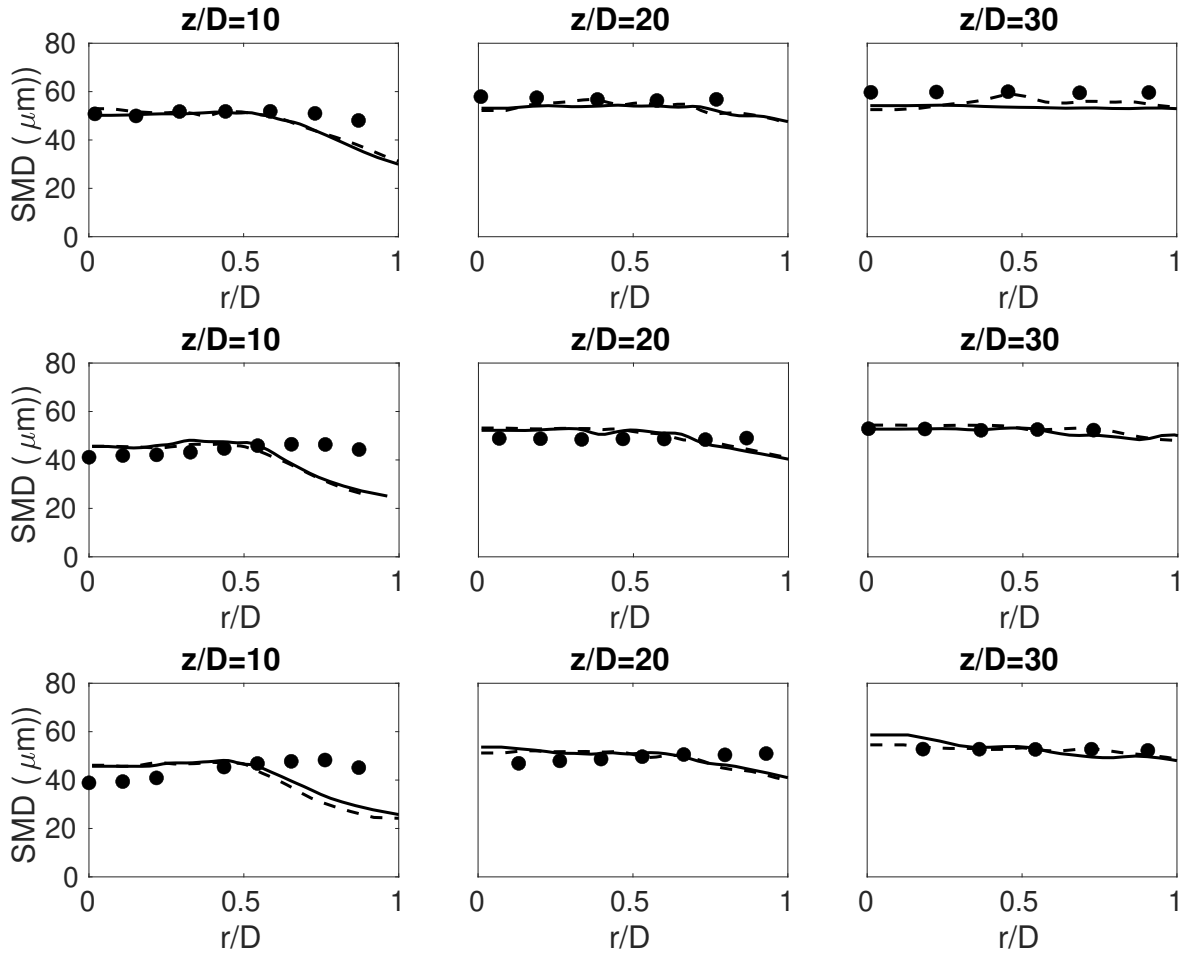
Figure 7.10: Radial profiles of Sauter mean diameter (SMD) in μm for flames EtF3 (top), EtF6 (middle), and EtF8 (bottom) at different axial locations. Solid lines represent solutions with adiabatic TGLDM. Dashed lines represent solutions with non-adiabatic TGLDM.

7.6   Summary

LES-CSE is implemented to investigate three turbulent ethanol spray flames featuring different jet velocities and constant fuel loading. The effects of heat loss due to spray evaporation and gas radiation are incorporated in the chemistry tables. The instantaneous snapshots of the gas temperature and heat release rate show that the turbulent flame structure is well captured. For flame EtF3, LES brings some improvements in the mean temperature profiles compared to previous RANS simulations, but centreline temperature remain underpredicted. The addition of enthalpy loss to the chemistry tables improves the gas temperature predictions near the peak locations, but results in further underprediction near the jet core. In the selected flames, the evaporation heat loss is found to be much larger than the radiative heat loss at all locations. The profiles of spray mean velocity, rms, and Sauter mean diameter are well captured in the simulations. The rms profiles are underpredicted at some locations. This may be due to the simple stochastic dispersion model used.

Chapter 8

Conclusions

8.1   Summary of main findings

In Chapter 5, RANS equations were solved coupled with CSE model for non-premixed combustion to simulate four acetone flames with diffusion characteristics. A modified k-ε turbulence model was used to correct the overpredicted jet spreading of axisymmetric jets. The Eulerian-Lagrangian method was applied where the Lagrangian approach is employed to determine the dispersed phase characteristics. The coupling between the two phases was achieved by introducing source terms to the governing equations to account for mass, momentum, and heat transfer. The selected flames included dilute sprays only. Detailed chemistry effects were included by generating the TGLDM tables prior to the simulations. The mean temperature and droplet velocities were compared with the experimental results for reacting acetone spray flames. The trends of the mean gas temperature profiles were well captured. However, overprediction near the peak was observed for all flames, in particular at farther downstream locations. Further, the peak temperature was also shifted radially outwards at downstream locations. The temperature was slightly underpredicted for flames AcF1 and AcF2 and significantly underpredicted for flame AcF5 near the jet-core. Previously published numerical studies [3, 4, 86, 87, 95, 96, 85, 88] also noted larger discrepancies at the third axial location. Possible sources of discrepancy are inaccurate turbulent mixing field due to RANS limitations, increased levels of premixing that cannot be captured in the present non-premixed CSE version, the neglect of spray effect on the conditional averages in the chemistry tabulation and a larger experimental uncertainty in the temperature measurements in high temperature regions. The mean droplets velocity profiles showed good agreement with the experiments for the four flames. However, the ve-

locity was underpredicted, especially near the centerline, for flames AcF1 and AcF2. This can be justified by the lower centerline temperature which causes lower thermal expansion. The velocity profiles of flames AcF3 and AcF5 were in good agreement with the experimental results since the temperature is higher at the centerline. The number of droplets in flames AcF3 and AcF5 is small at z/D=30 since the higher temperature at the centerline enhances the evaporation rates and most of the droplets evaporate before reaching this location. The present results may be improved by performing LES for better description of the turbulence and mixing fields, and including the evaporation effects in the chemistry tabulation.

In Chapter 6, the performance of CSE and DCSE in predicting the mean temperatures and spray velocities in three turbulent ethanol flames EtF1, EtF3, and EtF4 with varying degrees of premixing was compared. RANS equations were solved along with the standard k-ε model with standard coefficients. To implement DCSE, a progress variable is defined as a second conditioning variable. The progress variable is defined as the mass fraction of CO_2. For the three flames, DCSE resulted in improved mean temperature predictions over CSE and the results were in close agreement with the experimental data, except for z/D = 10 near the centreline for flames EtF1 and EtF3 where the DCSE temperatures were clearly lower than the experimental values. At these locations, near the jet exit, there may be a larger experimental error due to cooling effect on the thermocouples with larger amounts of droplets, probably combined with modelling errors due to the use of the standard k-ε model that may overpredict the jet spreading rate and underpredict the centreline values. Other modelling sources of error may be due to the joint PDF modelling, the neglect of evaporation effect on the conditional averages and the selected progress variable based on CO_2 only, for example. Otherwise, near the temperature peak location, CSE showed a temperature overprediction, while DCSE managed to improve the predictions significantly. Further analysis of the mean HRR indicates that DCSE reproduced some features of the complex flame structure found in the selected flames, in particular a double peak in the mean HRR could be seen in EtF1 and EtF4 at some locations and DCSE could include the effect of larger conditional fluctuations more accurately than CSE. Flames EtF1 and EtF3 were found to produce higher mean evaporation rates compared to flame EtF4 consistent with the introduced amount of spray into the domain. Further, the evaporation was seen to continue to farther axial distances in EtF1 and EtF3. In CSE, higher mean evaporation rates were shown in flames EtF1 and EtF3 where the peak was closer to the nozzle exit due to higher predicted temperatures in comparison to DCSE.
The predicted mean droplet velocity was in good agreement with the experimental data at z/D=10 and z/D=20. However, at z/D=30, the mean spray velocity was underpredicted for CSE and DCSE. The small droplets followed the underpredicted gas phase in the axial

and radial directions. In contrast, the large droplets exhibited velocity overpredictions at locations closer to the nozzle since they do not follow the gas velocity due to their high inertia. Further, this also produced a higher concentration of large droplets near the centreline.

The liquid volume flux was generally underpredicted, in particular near the centreline which indicates higher predicted evaporation rates. Reasonable agreement with the experiments was obtained for the Sauter mean diameter. However, the predictions exhibited systematic underpredictions at farther radial positions as a result of the lower number of large droplets at these locations.

In Chapter 7, LES-CSE was implemented to investigate three turbulent ethanol spray flames featuring different jet velocities and constant fuel loading. The effects of heat loss due to spray evaporation and gas radiation were incorporated in the chemistry tables. The instantaneous snapshots of the gas temperature and heat release rate showed that the turbulent flame structure was well captured. For flame EtF3, LES introduced some improvements in the mean temperature profiles compared to previous RANS simulations, but the centreline temperature remained underpredicted. The addition of the enthalpy loss to the chemistry tables improved the gas temperature predictions near the peak locations, but resulted in further underprediction near the jet core. In the selected flames, the evaporation heat loss was found to be much larger than the radiative heat loss at all locations. The trends of spray mean velocity, rms, and Sauter mean diameter were well captured in the simulations. The rms profiles were underpredicted at some locations. This may be due to the simple stochastic dispersion model used.

8.2   Summary of accomplishments

The main outcomes of the current dissertation can be summarized as

- Non-premixed CSE formulation for gas combustion was extended to simulate turbulent spray flames. An Eulerian-Lagrangian approach was used to describe the multiphase gas-spray interactions. RANS simulations of non-reacting acetone spray showed that the current implementation is capable of accurately predicting spray characteristics.

- Chemistry tables for acetone and ethanol combustion were generated using TGLDM for the first time.

- Numerical simulations using non-premixed CSE in RANS were conducted to study a series of mostly non-premixed acetone spray flames. The results showed generally good agreement with some discrepancies at some locations.

- DCSE was implemented for spray combustion to provide better description of flames with higher premixing levels. In contrast to previous DCSE implementations, a non-normalized form of the progress variable is used to eliminate several modeling difficulties.

- A RANS comparison between CSE and DCSE for a series of ethanol flames was carried out. DCSE introduced better predictions at most locations showing the effect of double conditioning.

- The effect of enthalpy loss due to spray evaporation and gas radiation on the conditional averages has been accounted for. This was achieved by adding an additional dimension for enthalpy loss to the chemistry tables.

- LES using CSE of ethanol flames with higher jet velocities were performed. Using LES combined with the heat loss effects resulted in better predictions at most locations.

8.3   Future work

In the current study, acetone and ethanol combustion is considered. However, actual engineering applications commonly use more complicated fuels such as kerosene and jet A. Thus, other tabulation techniques may be implemented along with CSE to simulate more complex fuels.

Numerical simulations of conventional spray are performed in the current work. The next step is to consider swirl spray combustion which requires more complex boundary conditions where higher turbulence levels are expected to enhance the mixing process.

All the simulations in the current investigation are conducted at atmospheric pressure. However, typical engines usually operate at much higher pressures. This would require different tabulation techniques. In addition, significant amounts of soot are expected at such high pressures where soot modeling should be introduced.

The current investigation considers only dilute spray. However, regions of dense spray usually exists in actual applications, especially near the injection nozzle. Thus, more

accurate models for liquid spray break-up, atomization, droplet collision and coagulation must be considered.

Regarding spray modeling, more sophisticated models may be investigated to provide further insight on the physics related to droplet evaporation, heat, and mass transfer.

In the current study, the Lagrangian approach is adopted for liquid phase description. A more thorough comparison should be conducted between the Lagrangian and Eulerian approach to determine their advantages and disadvantage. The Eulerian approach introduces some advantages such as easier coupling between the two phases and better description of the spray dispersion.

References

[1] B. P. Center, Annual energy outlook 2021, Energy Information Administration, Washington, DC (2021).

[2] J. D. Gounder, An experimental investigation of non-reacting and reacting spray jets, Ph.D. thesis, University of Sydney (2009).

[3] S. Ukai, A. Kronenburg, O. T. Stein, Simulation of dilute acetone spray flames with LES-CMC using two conditional moments, Flow Turbul. Combust. 93 (2014) 405–423.

[4] Y. Hu, R. Kurose, Nonpremixed and premixed flamelets LES of partially premixed spray flames using a two-phase transport equation of progress variable, Combust. Flame 188 (2018) 227–242.

[5] N. M. Marinov, A detailed chemical kinetic model for high temperature ethanol oxidation, Int. J. Chem. Kin. 31 (1999) 183–220.

[6] P. Dirrenberger, P.-A. Glaude, R. Bounaceur, H. Le Gall, A. P. Da Cruz, A. Konnov, F. Battin-Leclerc, Laminar burning velocity of gasolines with addition of ethanol, Fuel 115 (2014) 162–169.

[7] J. D. Gounder, A. Kourmatzis, A. R. Masri, Turbulent piloted dilute spray flames: Flow fields and droplet dynamics, Combust. Flame 159 (2012) 3372–3397.

[8] P. Domingo, L. Vervisch, J. Reveillon, DNS analysis of partially premixed combustion in spray and gaseous turbulent flame-bases stabilized in hot air, Combust. Flame 140 (2005) 172–195.

[9] D. Wacks, N. Chakraborty, Flame structure and propagation in turbulent flame-droplet interaction: a direct numerical simulation analysis, Flow Turbul. Combust 96 (2016) 1053–1081.

[10] A. Masri, Turbulent combustion of sprays: From dilute to dense, Combust. Sci. Technol. 188 (2016) 1619–1639.

[11] J. W. Labahn, C. B. Devaud, Investigation of conditional source-term estimation applied to a non-premixed turbulent flame, Combust. Theor. Model. 17 (2013) 960–982.

[12] S. Lee, C. Devaud, Application of conditional source-term estimation to two turbulent non-premixed methanol flames, Combust. Theor. Model. 20 (2016) 765–797.

[13] A. Masri, J. Gounder, Turbulent spray flames of acetone and ethanol approaching extinction, Combust. Sci. Tech. 182 (2010) 702–715.

[14] A. Hussien, C. B. Devaud, Simulations of turbulent acetone spray flames using the conditional source term estimation (CSE) approach, Combust. Theor. Model. 25 (2) (2021) 269–292.

[15] A. Hussien, C. Devaud, Simulations of partially premixed turbulent ethanol spray flames using doubly conditional source term estimation (DCSE), Combust. Flame (2021) 111651.

[16] S. B. Pope, Turbulent flows, IOP Publishing, 2001.

[17] D. C. Wilcox, Turbulence modeling for CFD, Vol. 2, DCW industries La Canada, CA, 1998.

[18] R. Cant, E. Mastorakos, An introduction to turbulent reacting flows, Imperial College Press, 2008.

[19] B. E. Launder, B. Sharma, Application of the energy-dissipation model of turbulence to the calculation of flow near a spinning disc, Letters in heat and mass transfer 1 (1974) 131–137.

[20] S. Pope, An explanation of the turbulent round-jet/plane-jet anomaly, AIAA journal 16 (1978) 279–281.

[21] R. Bilger, Turbulent flows with nonpremixed reactants, in: Turbulent reacting flows, Springer, 1980, pp. 65–113.

[22] N. Peters, Turbulent combustion. Cambridge University Press, 2000.

[23] C. Hollmann, E. Gutheil, Modeling of turbulent spray diffusion flames including detailed chemistry, Symposium (international) on combustion 26 (1996) 1731–1738.

[24] J. Smagorinsky, General circulation experiments with the primitive equations: I. the basic experiment, Monthly weather review 91 (1963) 99–164.

[25] M. Germano, U. Piomelli, P. Moin, W. H. Cabot, A dynamic subgrid-scale eddy viscosity model, Phys. Fluids A: Fluid Dynamics 3 (1991) 1760–1765.

[26] G. M. Faeth, Mixing, transport and combustion in sprays, Prog. Energy Combust. Sci. 13 (1987) 293–345.

[27] G. Stiesch, Modeling engine spray and combustion processes, Springer Science & Business Media, 2003.

[28] A. Mostafa, H. Mongia, On the modeling of turbulent evaporating sprays: Eulerian versus Lagrangian approach, Int. J. Heat Mass Trans. (1987) 2583–2593.

[29] G. Wu, W. A. Sirignano, Transient convective burning of a periodic fuel-droplet array, Proc. Combust. Inst. 33 (2011) 2109–2116.

[30] G. Wu, W. A. Sirignano, Transient convective burning of interactive fuel droplets in single-layer arrays, Combust. Theor. Model. 15 (2011) 227–243.

[31] G. Wu, W. A. Sirignano, Transient convective burning of interactive fuel droplets in double-layer arrays, Combust. Flame 158 (2011) 2395–2407.

[32] B. Wang, A. Kronenburg, D. Dietzel, O. Stein, Assessment of scaling laws for mixing fields in inter-droplet space, Proc. Combust. Inst. 36 (2017) 2451–2458.

[33] B. Wang, A. Kronenburg, G. L. Tufano, O. T. Stein, Fully resolved DNS of droplet array combustion in turbulent convective flows and modelling for mixing fields in inter-droplet space, Combust. Flame 189 (2018) 347–366.

[34] J. Lumley, Two-phase and non-newtonian flows, in: Turbulence, Springer, 1975, pp. 289–324.

[35] G. Batchelor, Transport properties of two-phase materials with random structure, Annu. Rev. Fluid Mech. 6 (1974) 227–255.

[36] R. O. Fox, F. Laurent, M. Massot, Numerical simulation of spray coalescence in an eulerian framework: direct quadrature method of moments and multi-fluid method, J. Comput. Phys. 227 (2008) 3058–3088.

[37] S. Subramaniam, Lagrangian–Eulerian methods for multiphase flows, Prog. Energy Combust. Sci. 39 (2013) 215–245.

[38] M. R. Maxey, J. J. Riley, Equation of motion for a small rigid sphere in a nonuniform flow, Phys. Fluids 26 (1983) 883–889.

[39] F. P. Kärrholm, Numerical modelling of diesel spray injection, turbulence interaction and combustion, Chalmers University of Technology Gothenburg, Sweden, 2008.

[40] J. D. Schwarzkopf, M. Sommerfeld, C. T. Crowe, Y. Tsuji, Multiphase flows with droplets and particles, CRC press, 2011.

[41] C. K. Law, Recent advances in droplet vaporization and combustion, Prog. Energy Combust. Sci. 8 (1982) 171–201.

[42] W. Sirignano, The formulation of spray combustion models: resolution compared to droplet spacing, J. Heat Trans. 108 (1986) 633–639.

[43] D. B. Spalding, The combustion of liquid fuels, in: Symposium (international) on combustion, Vol. 4, Citeseer, 1953, pp. 847–864.

[44] W. Ranz, W. R. Marshall, Evaporation from drops, Chem. eng. prog 48 (1952) 141–146.

[45] G. B. Macpherson, N. Nordin, H. G. Weller, Particle tracking in unstructured, arbitrary polyhedral meshes for use in cfd and molecular dynamics, Communications in Numerical Methods in Engineering 25 (2009) 263–273.

[46] D. Rochaya, Numerical simulation of spray combustion using bio-mass derived liquid fuels, Ph.D. thesis, Cranfield University (2007).

[47] B. Merci, D. Roekaerts, A. Sadiki, Experiments and numerical simulations of diluted spray turbulent combustion, Springer, 2011.

[48] J. K. Dukowicz, A particle-fluid numerical model for liquid sprays, J. Comput. Phys. 35 (1980) 229–253.

[49] P. A. Vesilind, The rosin-rammler particle size distribution, Resource Recovery and Conservation 5 (1980) 275–277.

[50] S. K. Liew, K. Bray, J. Moss, A flamelet model of turbulent non-premixed combustion, Combust. Sci. Tech. 27 (1981) 69–73.

[51] A. Y. Klimenko, R. W. Bilger, Conditional moment closure for turbulent combustion, Prog. Energy Combust. Sci. 25 (1999) 595–687.

[52] H. Steiner, W. Bushe, Large eddy simulation of a turbulent reacting jet with conditional source-term estimation, Phys. Fluids 13 (2001) 754–769.

[53] A. Y. Klimenko, S. Pope, The modeling of turbulent reactive flows based on multiple mapping conditioning, Phys. Fluids 15 (2003) 1907–1925.

[54] B. F. Magnussen, B. H. Hjertager, On mathematical modeling of turbulent combustion with special emphasis on soot formation and combustion, in: Symposium (international) on Combustion, Vol. 16, Elsevier, 1977, pp. 719–729.

[55] A. De, E. Oldenhof, P. Sathiah, D. Roekaerts, Numerical simulation of delft-jet-in-hot-coflow (djhc) flames using the eddy dissipation concept model for turbulence–chemistry interaction, Flow, Turbulence and Combustion 87 (4) (2011) 537–567.

[56] R. Bilger, Conditional moment closure for turbulent reacting flow, Phys. Fluids A: Fluid Dynamics 5 (1993) 436–444.

[57] A. Y. Klimenko, Multicomponent diffusion of various admixtures in turbulent flow, Fluid dynamics 25 (1990) 327–334.

[58] T. Lundgren, Model equation for nonhomogeneous turbulence, Phys. Fluids 12 (3) (1969) 485–497.

[59] S. B. Pope, Lagrangian pdf methods for turbulent flows, Annual review of fluid mechanics 26 (1) (1994) 23–63.

[60] S. B. Pope, PDF methods for turbulent reactive flows, Prog. Energy Combust. Sci. 11 (1985) 119–192.

[61] D. C. Haworth, Progress in probability density function methods for turbulent reacting flows, Progress in Energy and combustion Science 36 (2) (2010) 168–259.

[62] J. Kirchmann, A. Kronenburg, O. Stein, M. Cleary, Two-phase sparse-lagrangian MMC-LES of dilute ethanol spray flames, Proc. Combust. Inst. 38 (2020) 1–9.

[63] W. K. Bushe, H. Steiner, Conditional moment closure for large eddy simulation of nonpremixed turbulent reacting flows, Phys. Fluids 11 (1999) 1896–1906.

[64] R. Grout, W. K. Bushe, C. Blair, Predicting the ignition delay of turbulent methane jets using conditional source-term estimation, Combust. Theor. Model. 11 (2007) 1009–1028.

[65] M. Wang, J. Huang, W. Bushe, Simulation of a turbulent non-premixed flame using conditional source-term estimation with trajectory generated low-dimensional manifold, Proc. Combust. Inst. 31 (2007) 1701–1709.

[66] J. Huang, W. Bushe, Simulation of transient turbulent methane jet ignition and combustion under engine-relevant conditions using conditional source-term estimation with detailed chemistry, Combust. Theor. Model. 11 (2007) 977–1008.

[67] J. W. Labahn, C. Devaud, Species and temperature predictions in a semi-industrial mild furnace using a non-adiabatic conditional source-term estimation formulation, Combust. Theor. Model. 21 (2017) 466–486.

[68] J. W. Labahn, I. Stanković, C. B. Devaud, B. Merci, Comparative study between conditional moment closure (CMC) and conditional source-term estimation (CSE) applied to piloted jet flames, Combust. Flame 181 (2017) 172–187.

[69] M. Salehi, W. Bushe, Presumed PDF modeling for RANS simulation of turbulent premixed flames, Combust. Theor. Model. 14 (2010) 381–403.

[70] D. Dovizio, M. M. Salehi, C. B. Devaud, RANS simulation of a turbulent premixed bluff body flame using conditional source-term estimation, Combust. Theor. Model. 17 (2013) 935–959.

[71] N. Shahbazian, M. M. Salehi, C. P. Groth, Ö. L. Gülder, W. K. Bushe, Performance of conditional source-term estimation model for LES of turbulent premixed flames in thin reaction zones regime, Proc. Combust. Inst. 35 (2015) 1367–1375.

[72] D. Dovizio, A. Debbagh, C. Devaud, RANS simulations of a series of turbulent v-shaped flames using conditional source-term estimation, Flow Turbul. Combust. 96 (2016) 891–919.

[73] J. Labahn, D. Dovizio, C. Devaud, Numerical simulation of the Delft-jet-in-hot-coflow (DJHC) flame using conditional source-term estimation, Proc. Combust. Inst. 35 (2015) 3547–3555.

[74] J. Labahn, C. Devaud, Large eddy simulations (LES) including conditional source-term estimation (CSE) applied to two Delft-jet-in-hot-coflow (DJHC) flames, Combust. Flame 164 (2016) 68–84.

[75] D. Dovizio, J. W. Labahn, C. B. Devaud, Doubly conditional source-term estimation (DCSE) applied to a series of lifted turbulent jet flames in cold air, Combust. Flame 162 (2015) 1976–1986.

[76] D. Dovizio, C. Devaud, Doubly conditional source-term estimation (DCSE) for the modelling of turbulent stratified v-shaped flame, Combust. Flame 172 (2016) 79–93.

[77] M. Mortada, C. Devaud, Large eddy simulation of lifted turbulent flame in cold air using doubly conditional source-term estimation, Combust. Flame 208 (2019) 420–435.

[78] S. Girimaji, Assumed β-pdf model for turbulent mixing: Validation and extension to multiple scalar mixing, Combust. Sci. Tech. 78 (1991) 177–196.

[79] A. Tikhonov, V. Arsenin, Solution of incorrectly formulated problems and the regularization method, Soviet Mathematics Doklady 4 (1963) 1035–1038.

[80] J. W. Labahn, C. B. Devaud, T. A. Sipkens, K. J. Daun, Inverse analysis and regularisation in conditional source-term estimation modelling, Combust. Theor. Model. 18 (3) (2014) 474–499.

[81] S. B. Pope, Small scales, many species and the manifold challenges of turbulent combustion, Proc. Combust. Inst. 34 (1) (2013) 1–31.

[82] S. Pope, U. Maas, Simplifying chemical kinetics: Trajectory-generated low-dimensional manifolds, Mechanical and Aerospace Engineering Report, Ithaca, NY, Report No. FDA (1993) 93–11.

[83] P. C. Hansen, Numerical tools for analysis and solution of fredholm integral equations of the first kind, Inverse problems 8 (1992) 849.

[84] R. J. Renka, Algorithm 751: Tripack: a constrained two-dimensional delaunay triangulation package, ACM Transactions on Mathematical Software (TOMS) 22 (1996) 1–8.

[85] Y. Hu, R. Kurose, Partially premixed flamelet in LES of acetone spray flames, Proc. Combust. Inst. 37 (2019) 3327–3334.

[86] M. Chrigui, J. Gounder, A. Sadiki, A. R. Masri, J. Janicka, Partially premixed reacting acetone spray using LES and FGM tabulated chemistry, Combust.Flame. 159 (2012) 2718–2741.

111

[87] M. Chrigui, J. Gounder, A. Sadiki, J. Janicka, A. Masri, Acetone droplet behavior in reacting and non reacting turbulent flow, Flow Turbul. Combust. 90 (2013) 419–447.

[88] N. Khan, M. J. Cleary, O. T. Stein, A. Kronenburg, A two-phase MMC-LES model for turbulent spray flames, Combust. Flame 193 (2018) 424–439.

[89] L. Ma, D. Roekaerts, Modeling of spray jet flame under mild condition with non-adiabatic FGM and a new conditional droplet injection model, Combust. Flame 165 (2016) 402–423.

[90] Y. Zhang, H. Wang, A. Both, L. Ma, M. Yao, Effects of turbulence-chemistry interactions on auto-ignition and flame structure for n-dodecane spray combustion, Combust. Theor. Model. 23 (2019) 907–934.

[91] C. T. Chong, S. Hochgreb, Measurements of laminar flame speeds of acetone/methane/air mixtures, Combust. Flame 158 (2011) 490–500.

[92] R. Barlow, A. Karpetis, J. Frank, J.-Y. Chen, Scalar profiles and no formation in laminar opposed-flow partially premixed methane/air flames, Combust. Flame 127 (2001) 2102–2118.

[93] TNF Workshop. http://www.sandia.gov/tnf/abstract.html.

[94] X. Fang, R. Ismail, K. Bushe, M. Davy, Simulation of ECN diesel spray A using conditional source-term estimation, Combust. Theor. Model. 24 (2020) 1–36.

[95] S. Ukai, A. Kronenburg, O. Stein, LES-CMC of a dilute acetone spray flame, Proc. Combust. Inst. 34 (2013) 1643–1650.

[96] S. Ukai, A. Kronenburg, O. Stein, Large eddy simulation of dilute acetone spray flames using CMC coupled with tabulated chemistry, Proc. Combust. Inst. 35 (2015) 1667–1674.

[97] W. Bushe, C. Devaud, J. Bellan, A priori evaluation of the Double-conditioned Conditional Source-term Estimation model for high-pressure heptane turbulent combustion using DNS data obtained with one-step chemistry, Combust. Flame 217 (2020) 131–151.

[98] C. Devaud, W. Bushe, J. Bellan, The modeling of the turbulent reaction rate under high-pressure conditions: a-priori evaluation of the conditional source term estimation concept, Combust. Flame 207 (2019) 205–221.

112

[99] M. Chrigui, A. Masri, A. Sadiki, J. Janicka, Large eddy simulation of a polydisperse ethanol spray flame, Flow Turbul. Combust. 90 (2013) 813–832.

[100] S. De, S. H. Kim, Large eddy simulation of dilute reacting sprays: Droplet evaporation and scalar mixing, Combust. Flame 160 (2013) 2048–2066.

[101] A. Rittler, F. Proch, A. M. Kempf, LES of the Sydney piloted spray flame series with the PFGM/ATF approach and different sub-filter models, Combust. Flame 162 (2015) 1575–1598.

[102] H. A. El-Asrag, M. Braun, A. R. Masri, Large eddy simulations of partially premixed ethanol dilute spray flames using the flamelet generated manifold model, Combust. Theor. Model. 20 (2016) 567–591.

[103] Y. Hu, R. Kai, R. Kurose, E. Gutheil, H. Olguin, Large eddy simulation of a partially pre-vaporized ethanol reacting spray using the multiphase DTF/flamelet model, Int. J. Multiph. Flow 125 (2020) 103216.

[104] A. L. Pillai, R. Kurose, Combustion noise analysis of a turbulent spray flame using a hybrid DNS/APE-RF approach, Combust. Flame 200 (2019) 168–191.

[105] A. Kronenburg, Double conditioning of reactive scalar transport equations in turbulent nonpremixed flames, Phys. Fluids 16 (2004) 2640–2648.

[106] W. Bushe, Spatial gradients of conditional averages in turbulent flames, Combust. Flame 192 (2018) 314–339.

[107] L. Vervisch, R. Hauguel, P. Domingo, M. Rullaud, Three facets of turbulent combustion modelling: DNS of premixed v-flame, LES of lifted nonpremixed flame and RANS of jet-flame, Journal of turbulence 5 (2004) 1–8.

[108] P. Auzillon, O. Gicquel, N. Darabiha, D. Veynante, B. Fiorina, A filtered tabulated chemistry model for LES of stratified flames, Combust. Flame 159 (2012) 2704–2717.

[109] M. Ghadimi, H. Atayizadeh, M. M. Salehi, Presumed joint-PDF modelling for turbulent stratified flames, Flow Turbul. Combust. (2021) 1–35.

[110] M. P. Sitte, E. Mastorakos, Modelling of spray flames with doubly conditional moment closure, Flow Turbul. Combust. 99 (2017) 933–954.

[111] M. P. Sitte, E. Mastorakos, Large eddy simulation of a spray jet flame using doubly conditional moment closure, Combust. Flame 199 (2019) 309–323.

113

[112] S. Sreedhara, K. Y. Huh, Conditional statistics of nonreacting and reacting sprays in turbulent flows by direct numerical simulation, Proc. Combust. Inst. 31 (2) (2007) 2335–2342.

[113] H. Wang, K. Luo, J. Fan, Direct numerical simulation and cmc (conditional moment closure) sub-model validation of spray combustion, Energy 46 (1) (2012) 606–617.

[114] C. T. d'Auzay, U. Ahmed, A. L. Pillai, N. Chakraborty, R. Kurose, Statistics of progress variable and mixture fraction gradients in an open turbulent jet spray flame, Fuel 247 (2019) 198–208.

[115] C. Heye, V. Raman, A. R. Masri, Les/probability density function approach for the simulation of an ethanol spray flame, Proc. Combust. Inst. 34 (2013) 1633–1641.

[116] H. Kolla, J. Rogerson, N. Chakraborty, N. Swaminathan, Scalar dissipation rate modeling and its validation, Combust. Sci. Technol. 181 (2009) 518–535.

[117] D. G. Goodwin, H. K. Moffat, R. L. Speth, Cantera: An object-oriented software toolkit for chemical kinetics, thermodynamics, and transport processes, Caltech, Pasadena, CA 124 (2009).

[118] S. Ukai, Conditional moment closure modelling of turbulent spray flames, Ph.D. thesis, University of Stuttgart (2014).

[119] F. Nicoud, F. Ducros, Subgrid-scale stress modelling based on the square of the velocity gradient tensor, Flow Turbul. Combust. 62 (1999) 183–200.

[120] W. L. Grosshandler, Radcal: a narrow-band model for radiation, Calculations in a Combustion Environment, NIST Technical Note 1402 (1993).

[121] S. De Chaisemartin, L. Fréret, D. Kah, F. Laurent, R. Fox, J. Reveillon, M. Massot, Eulerian models for turbulent spray combustion with polydispersity and droplet crossing, Comptes Rendus Mécanique 337 (2009) 438–448.

[122] C. Pera, J. Réveillon, L. Vervisch, P. Domingo, Modeling subgrid scale mixture fraction variance in les of evaporating spray, Combust. Flame 146 (4) (2006) 635–648.

[123] J. Tillou, J.-B. Michel, C. Angelberger, C. Bekdemir, D. Veynante, Large-eddy simulation of diesel spray combustion with exhaust gas recirculation, Oil & Gas Science and Technology–Revue d'IFP Energies nouvelles 69 (1) (2014) 155–165.

[124] M. Klein, A. Sadiki, J. Janicka, A digital filater based generation of inflow data for spatially developing direct numerical or large eddy simulations, J. Comput. Phys. 186 (2003) 652–665.

[125] T. J. Poinsot, S. Lelef, Boundary conditions for direct simulations of compressible viscous flows, J. Comput. Phys. 101 (1992) 104–129.